Jamila Djafari

Mestre em Engenharia Quimica e Quimica Molecular

Synthesis, Characterization and Applications of Gold and Silver Nanoparticles: From Antibacterial to Optoelectronic Nanomaterials

Dissertação para obtenção do Grau de Doutor em Quimica

Orientador: Prof. Dr. José Luis Capelo Martinez,
Associated Professor with habilitation
LAQV-Requimte, Faculdade de Ciências e Tecnologia, Universidade Nova de Lisboa

Co-orientador: Prof. Dr. Carlos Lodeiro Espiño,
Associated Professor with habilitation
LAQV-Requimte, Faculdade de Ciências e Tecnologia, Universidade Nova de Lisboa

Dr. Javier Fernandez-Lodeiro,
Researcher
LAQV-Requimte, Faculdade de Ciências e Tecnologia, Universidade Nova de Lisboa

Júri:

Presidente: Prof. Doutor Manuel Luís de Magalhães Nunes da Ponte
Vogais: Prof. Doutor Carlos Lodeiro Espiño
Prof. Doutora Julia Lorenzo Rivera
Doutor Fernando Novio Vazquez
Doutor Hugo Miguel Baptista Carreira Dos Santos

FACULDADE DE CIÊNCIAS E TECNOLOGIA
UNIVERSIDADE NOVA DE LISBOA

Junho de 2019

Jamila Djafari

Mestre em Engenharia Quimica e Quimica Molecular

Synthesis, Characterization and Applications of Gold and Silver Nanoparticles: From Antibacterial to Optoelectronic Nanomaterials

Dissertação para obtenção do Grau de Doutor em Quimica

Orientador: Prof. Dr. José Luis Capelo Martinez,
Associated Professor,
LAQV-Requimte, Faculdade de Ciências e Tecnologia, Universidade Nova de Lisboa

Co-orientador: Prof. Dr. Carlos Lodeiro Espiño,
Associated Professor with habilitation
LAQV-Requimte, Faculdade de Ciências e Tecnologia, Universidade Nova de Lisboa

Dr. Javier Fernandez-Lodeiro,
Researcher
LAQV-Requimte, Faculdade de Ciências e Tecnologia, Universidade Nova de Lisboa

Júri:

Presidente: Prof. Doutor Manuel Luís de Magalhães Nunes da Ponte
Vogais: Prof. Doutor Carlos Lodeiro Espiño
Prof. Doutora Julia Lorenzo Rivera
Doutor Fernando Novio Vazquez
Doutor Hugo Miguel Baptista Carreira Dos Santos

FACULDADE DE CIÊNCIAS E TECNOLOGIA
UNIVERSIDADE NOVA DE LISBOA

Junho de 2019

Synthesis, Characterization and Applications of Gold and Silver Nanoparticles: From Antibacterial to Optoelectronic Nanomaterials

“Nothing happens without effort. You have to have faith. And for that, you have to break down the barriers of prejudice, which requires courage. To have courage, you must conquer your fears.”

Paulo Coelho

To my dear parents and my brother,

Acknowledgments

I want to thank my supervisor Prof. Dr José Luis Capelo Martinez and my co-supervisor Prof. Dr Carlos Lodeiro Espiño for giving me the opportunity to do my PhD thesis under their supervision in the BIOSCOPE Group. I also thank them for welcoming me to their laboratory and for helping me in all stages of this thesis. I thank them for their extreme kindness, their understanding, and for the beautiful people they are. I shared great moments at your side, thank you for everything because without them I could not have achieved this thesis.

I would like to thank the PROTEOMASS Scientific Association for the support for PhD inscription fees, all reagents and general funding during my thesis. Moreover, I would like to thank the FCT-MEC for my Research Contract associate with the R&D project PTDC/QEQ-MED/2118/2014 allowing me to acquire complementary skills during my thesis. To the research units, UCIBIO-REQUIMTE (2015-2107) and to the LAQV-REQUIMTE (2018-2019) for their support and help during these periods.

I sincerely thank my thesis co-supervisor Dr Javier Fernández-Lodeiro for teaching me the labor part of this thesis. I thank him for these long scientific explanations, for these late hours in the laboratory, for these moments of stress but which allowed us to live these moments of joy with each concretion of work. I thank him also for transmitting me his vision of science that is in line with its excellent values and scientific objectives. His autodidactic allowed me to realize that the most important is not only the result, but all the road travelled to reach these objectives even if it is strewn with pitfalls. Each error is learning and is necessary for scientific growth. A big thank for his patience, his foresight and for taking me under his wing to achieve all these projects. Even without having a background in nanomaterials, I was able to acquire reliable knowledge in nanoparticle synthesis that allowed me to understand theoretically but especially to precisely observe each synthesis of nanoparticles as different from each other — an enormous thanks for this.

I would like to thank all my co-workers and colleagues from the BIOSCOPE Group at the laboratory, more specially to Adrián Fernández-Lodeiro for his valuable help in the laboratory, and Susana Jorge, Eduardo Aráujo, Silvia Nuti, Gonçalo Marcelo, Dr. Elisabete Oliveira, Dr. Hugo Santos, Luis Carvalho, Gonçalo Martins, Joao Prates, and Dr. Cristian Cuerva for these shared moments, especially during the organization of the events, and during the birthdays celebrations, thank you for your good mood and your kindness. Thanks also to the colleagues working in PROTEOMASS, Ana Laço and Marta Silva.

I want to thank all the collaborators which have contributed in my work with the antibacterial, protein and SERS studies. Mainly, I would like to mention Prof. Gilberto Igrejas and Prof. Dr Patricia Poeta, and Ms. Vanessa Silva from the University of Trás-os-Montes e Alto Douro (Portugal) and Prof. Dr. Carmen Torres from the University of La Rioja (Spain) for the antibacterial studies; Prof. Dr. Emilia Bértolo Pardo, Prof. Simon C Harvey and Dr. Marie T McConnell from the Christ Church University of Canterbury (UK) for the protein and biological test on the functionalized gold@lectine nanoparticles; Dr. Benito Rodríguez-González from the University of Vigo, CACTI (Spain) for some of the HRTEM and TEM characterization, and Prof. Dr. Isabel Pastoriza, Prof. Dr. Jorge Perez-Juste and Mr. Daniel Garcia-Lojo from the University of Vigo (Spain) for the SERS studies. And for Mr. Carlos Fernández-Lodeiro for his collaboration in the synthesis of silver nanoplates.

Thanks to the Analytical Laboratory at the REQUIMTE-Chemistry Department for their support, and specially the help to Dr. Luz Fernandes, Carla Rodrigues, Nuno Costa and Ana Teresa Lopes. Thanks also to Laboratory technicians at the 4th floor of the Chemistry Department, Mrs. Idalina Martins e Mrs. Conceição Luis for their help and extreme kindness.

And finally, I would like to thank to Prof. Marco Diogo Richter Da Silva for his help as the Chemistry Doctoral Program coordinator.

D'un point de vue personnel, je souhaite remercier ma famille du plus profond de mon cœur. Tout d'abord, à mes deux modèles, aux personnes les plus importantes à mes yeux, mes parents Ivanira et Tawfik. Je vous remercie de m'avoir soutenu à chaque étape de cette expérience et d'avoir toujours été là pour moi dans les bons comme dans les mauvais moments. Je vous remercie sincèrement d'avoir toujours cru en moi et de m'avoir inculqué toutes ces belles valeurs qui font partie de votre être. Merci pour votre bienveillance, vos enseignements, et merci simplement d'être vous-même cela a permis d'être la personne que je suis aujourd'hui. Je ne vous remercierai jamais assez pour tout ce que vous avez fait pour moi car sans vous je ne serai rien. Je vous aime du fond du cœur. Un grand merci à mon petit frère adoré Yanis, mon sang, mon humain préféré, mon meilleur ami et mon confident. Merci pour ton optimisme et ta bonne humeur qui m'ont remonté le moral maintes fois. Merci pour ces good vibes, ces soirées télé, ces discussions, ces restaus et tous ces bons moments qu'on a passé ensemble. Sache que je serai toujours là pour toi et que je t'aime fort. Bien sûr, un grand merci à ma petite chienne Rubis que j'aime du fond du cœur et qui me manque terriblement.

Merci à ma tante Amel, Didier et mon petit Medhi pour tous ces moments passés ensemble lorsque je rentrais à la maison. A chaque fois, c'est un plaisir de vous voir et de pouvoir me changer les idées, merci de votre soutien.

Merci à ma famille répartie dans le monde, qui malgré la distance est toujours là pour moi notamment à mes oncles, tantes et cousines au Canada et en Algérie, merci pour leur soutien.

Obrigado tambem a minha familia brasileira com quem estou sempre em contacto, e com quem eu morro de dar risada com todas nossas discussões no cellular. Obrigado por suas belezas, vôcés são pessoas increiveis e lindas. Obrigado tambem a minha linda avo Dona Nena por ser o que ela e, uma pessoa maravilhosa, tenho muita saudades e espero verte pronto.

Une grande pensée à mes étoiles qui me manquent et qui veillent sur moi: Tata, Habibi et vovo Mario, shukraan et obrigado.

Merci à mes amies de toujours, Pauline et Camille. Merci pour ces moments partagés, et pour cette jolie amitié qui dure depuis plus de 20 ans déjà. Merci pour ces fous rires, ces discussions sans fin, pour votre bienveillance et surtout merci d'être là pour moi. Merci également à Sabrina, Yahia, Carole et Anne-Sophie.

Bien sûr, merci à Marie-Paule et Patrice pour leur aide et leur soutien, ainsi qu'à leurs familles respectives pour ces dinés passés ensemble et tous ces bons moments qui sont gravés dans ma mémoire. Un grand merci à Souheila que je considère comme ma petite sœur, et qui pour qui j'ai beaucoup d'affection. Merci d'avoir été là pour moi et merci à toute ta famille pour ces moments de joie partagés ensemble au rythme latino.

Agradezco, por supuesto, a la segunda familia que gané en los últimos años y que me recibió con los brazos abiertos en su casa. Gracias a Pilucha, por haberme considerado como su hija y por haberme dado el amor como una madre, nunca te agradeceré lo suficiente por tu sonrisa, tu bondad y por la fabulosa persona que eres. Gracias a Josecho por su sabiduría, su sentido del humor, me río mucho contigo, y gracias por aprovechar la vida como lo haces, es contagioso. Gracias a Esther, paz para su alma en el cielo, y a Avelino por su amabilidad siempre conmigo. Gracias a "Los Valentinos", mi pequeña Valentina, Paula y Abel, y por todos estos divertidos momentos pasados juntos, siempre es un placer estar con vosotros. Gracias a Adrián, mi compañero de tesis, gracias por tu apoyo, tu ayuda y por todos tus chistes. Alguien me dijo que eras una de las personas más amables que conocía y tiene toda la verdad. ¡Gracias a mi pequeño

Carlitos, que vino al laboratorio, y pudo experimentar la síntesis de los nanoprismas de plata conmigo, menuda aventura la nuestra! Pude comprobar que eres una persona de oro en la macroescala, correcta y brillante, especialmente mantente como eres, porque eres una persona excepcional. Gracias a Paula igualmente.

Gracias a todos mis nuevos amigos en España con quien he pasado muy buenos momentos y fiestas.

Gracias a los lindos animales españoles que compartieron buenos momentos conmigo: Luna, Athina, Piranha, Daphne, y Lila. Y a los que están en el cielo: Poncho, Hugo y Nacho.

Y, por supuesto, gracias a mi novio, que, sin él, podría haber renunciado a este reto. Gracias por apoyarme todos los días, por ser paciente conmigo y por estar siempre a mi lado. Gracias por todos estos momentos juntos que me permitieron escapar durante todos los períodos de estrés. Gracias por ser la persona más bella que conozco.

NAMASTE

Resumo

A investigação e o desenvolvimento de novas nanopartículas metálicas (NPs) têm crescido nas últimas décadas como resultado das propriedades ventajosas que estes nano-materiais apresentam. A sua natureza metálica associada ao seu tamanho diminuto resulta em propriedades físico-químicas que constituem uma ve ntagem real para a construção de uma nova gama de materiais nano-métricos com potenciais aplicações em campos como a biomédicina, eletrônicos, óticos ou catalíticos, entre muitos outros.

Atualmente, muitas áreas científicas e tecnológicas estão obtendo muitos benefícios pelo uso e desenvolvimento dos nano-materiais de ouro e prata. Nó entanto neste momento, é necessário desenvolver novas metodologias reproduzíveis que permitam uma maior compreensão dos materiais em escala nanométrica, favorecendo a construção das NPs de ouro e prata mais precisas e complexas, controlando seu tamanho, forma e composição, permitindo novas aplicações.

Com o objetivo de introduzir novos avanços sintéticos na área de nanotecnologia, na presente tese de doutorado temos estudado: i) A síntese e caracterização de NPs de ouro biofuncionalizadas com proteínas; ii) O desenvolvimento de uma nova ruta sintética para produzir NPs de ouro e prata usando Tetraciclina como agente sintético; iii) A síntese e funcionalização de nanoplacas triangulares de prata e seu subsequente revestimento controlado orgânico ou inorgânico (camada de sílica), e iv) Uma síntese inovadora de NPs de ouro pseudo-esféricas, multi-ponta ou tipo framboesa, utilizando Ferro(II) como agente redutor sustentável.

Além disso, as propriedades antimicrobianas e optoelectrónicas e as aplicações das NPs produzidas foram exploradas e estudadas.

Palavra Chaves: Nanoparticulas, Ouro, Prata, Sintese, Sensor, Antibacteriano.

Abstract

The Research and development of new metallic nanoparticles (NPs) have been booming in recent decades as a result of the advantageous properties presented by these nanomaterials. Their metallic nature associated with their tiny size induce physicochemical properties that constitute a real advantage for the construction of a new range of nano-metric materials with potential applications in biomedical, electronic, optical or catalytic fields, among many others. Until now, many scientific and technological fields are obtaining great benefits by the utilization and development of gold and silver nanomaterials. However currently, it is necessary to develop new reproducible methodologies allowing a greater understanding of the nano-scale materials thus promoting the construction of most precise and more complex gold and silver NPs through the control of their size, shape and composition, allowing new reviewed applications.

With the aim to introduce new synthetic advances in the nanotechnology area, in the present doctoral thesis we have studied: i) The synthesis and characterization of bio-functionalized gold NPs with proteins; ii) The development of a nobel synthetic approach to produce gold and silver NPs using Tetracycline as synthetic agent; iii) The synthesis and functionalization of silver triangular nanoplates and their subsequent controlled organic and inorganic (silica layer) coating; and iv) the creation of a novelty synthesis of pseudo-spherical, multi-tip or raspberry like AuNPs using Iron (II) as Green reducing agent.

Furthermore, the antimicrobial and optoelectronic properties of the produced NPs and their applications have been explored and studied.

Keywords: Nanoparticles, Gold, Silver, Sensing, Antibacterial

Table of Contents

List of Figures

List of Tables

Abbreviations

4-NTP	4-nitrothiophenol
AEFs	Analytical enhancement factors
Ag	Silver
AgNPs	Silver Nanoparticles
AgNPs@TC	Silver Nanoparticles functionalized with Tetracycline
AgNTs	Silver nanoprisms
AgNTs@MHA	Silver nanoprisms functionalized with 16-mercaptohexadecanoic acid
AgNTs@Si-COOH	Silver nanoprisms functionalized with carboxylate terminated silica
AgNTs@Si-NH_2	Silver nanoprisms functionalized with amine terminated silica
AgNTs@Si-OH	Silver nanoprisms functionalized with alcohol terminated silica
APTMS	(3-Aminopropyl)triethoxysilane
a-THF	Anhydrous Tetrahydrofuran
Au	Gold
AuNPs	Gold nanoparticles
AuNPs@Citrate	Gold nanoparticles functionalized with Citrate
AuNPs@EHL	Gold nanoparticles conjugated with EHL
AuNPs@TC	Gold nanoparticles functionalized with Tetracycline
BSPP	bis (p-sulfonatophenyl) phenylphosphine
CFU	Colony-forming unit
CTAB	Cetyltrimethylammonium bromide
DLS	Dynamic Light Scattering
DMA	Dimethylamine
DMF	Dimethylformamide
DNA	Deoxyribose Nucleic Acid
EHL	*Eranthis hyemalis*
FT-IR	Fourier Transform InfraRed
HAADF	High-Angle Annular Dark-Field Imaging
HRTEM	High Resolution Transmission Electronic Microscopy
ICP	Inductively Coupled Plasma-Atomic Emission Spectrometer
LB	Luria-Bertani
LOD	Limit of Detection
LSPR	Localized Surface Plasmon Resonance
MBC	Minimum bactericidal concentration

MHA	16-Mercaptohexadecanoic acid
MIC	Minimum inhibitory concentration
MQ	Milli-Q
NGM	Nematode Growth Media
PBS	Phosphate Buffered Saline
PDI	Polydispersity Index
PVP	Polyvinylpyrrolidone
PSS	Poly(sodium 4-styrenesulfonate)
RIP	Ribosome Inactivating Protein
RT	Room Temperature
SAED	Selected Area Electron Diffraction
SERS	Surface Enhanced Raman Spectroscopy
SPR	Surface Plasmon Resonance
STEM	Scanning Transmission Electron Microscope
TC	Tetracycline
TEM	Transmission Electronic Microscopy
TEOS	Tetraethyl orthosilicate
UV-Vis	UltraViolet-Visible

Symbols

d	Particle diameter
Cext	Cross-section extinction
ε_m	Dielectric constant of the medium
R	Radius of the sphere
ε_r	Real component of the dielectric function of nanoparticles
ε_i	Imaginary component of the dielectric function of nanoparticles
λ	Wavelength of the incident radiation
ΔG	Total Gibbs free energy variation
r	Radius of the spherical nuclei
ΔGv	Free energy of the crystal
γ	Surface tension energy
ΔGc	Critical global free energy
rc	Critical radius
kb	Boltzmann constant
T	Temperature
υ	Molar volume
S	Supersaturation
C	Concentration
Cs	Concentration at solubility
I_{SERS}	SERS intensity for a selected mode of a given analyte
I_{RS}	Non-enhanced Raman intensity
c_{SERS}	Analyte concentration in the SERS
c_{RS}	Analyte concentrations in the Raman experiments

CHAPTER

1

GENERAL INTRODUCTION

1.1. METALLIC NANOPARTICLES BACKGROUND: RAW MATERIALS TO METAL COLLOIDS

Metals such as gold, silver or copper have been widely used by humankind for millennia as a result of their availability in the native state. Already in the time of ancient civilizations, especially in Egypt and Mesopotamia, metallurgy and mining techniques were developed and exploited for the production of metal objects, pieces of jewelry or ornaments.[1–3] Among the three metals mentioned, gold was one of the most worked metal due to its bright color, beauty, malleability and resistance to corrosion. Long considered as a symbol of the sun and a "gift from the Gods" by several civilizations, gold was widely used to represent loyalty, lust and royalty. For instance, the older collections of pure gold objects dating from 4600-4200 BCE were found in Bulgaria in 1972 and represent around 6 kg of gold jewelry, vessels and decorative objects. This overwhelming collection of more than 300 objects of solid gold was found in the richest tombs of an ancient cemetery (near the Black Sea) highlighting the mystical and religious character of gold, as well as the hierarchical culture during this period.[2]

Regarding silver, this metal was not used as much as gold to symbolize royalty but in contrast it was widely used as a payment method (as well as electrum coins, made of a natural

alloy of silver and gold) but also to produce recipient to keep fresher food and liquids.[4] On the contrary, copper acquired a more important role in the manufacture of tools, weapons and dishes among others.

Over the years, the development of alchemy allowed to perform different techniques such as heating, distillation, reflux or sublimation, to produce metals-based objects. Alchemists' motivation at that time was based on the discovery of the "philosopher's stone". It was believed that the aforementioned stone, reddish in appearance, give eternal life and allowed the transmutation of base metals into gold or silver.[5] Efforts to find this "chemical treasure" improved alchemists' technics arising many alloys with different colors and compositions.[5,6] Besides, with the evolution of glass manufacturing, it was possible to create different colored glasses through the addition of specific amounts of transition metals such as copper, gold and silver.[7]

Possibly, the most famous object in history composed of a special class of colored glass dating from the 4th century BC is known as the Lycurgus Cup which is exhibited at the British Museum in London. This drinking *cage cup* is a typical Roman cup composed of a carved decorative frieze representing the scene of the triumph of Dionysus (god of the wine) on Lycurgus (king of Edoni).[8] The richness of this piece is not only due to the skills developed to make this carved piece, but to the unusual optical properties compared to other pieces found at this time. Indeed, the cup exhibits strong dichroism, when the cup is illuminated from the inside, a red ruby color is transmitted while it appears green opaque when it's illuminated from the outside. (**Figure 1.1**)

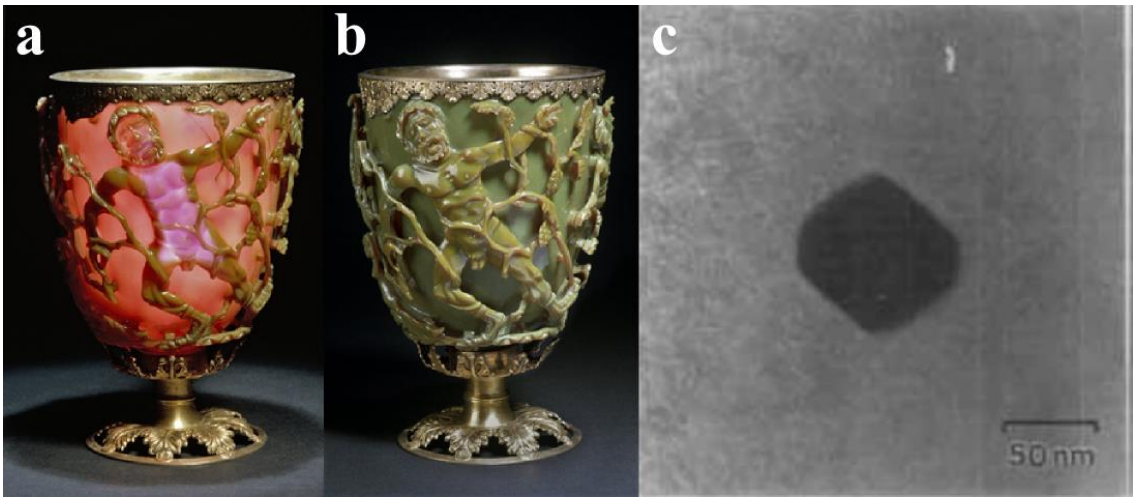

Figure 1.1. Photos of the Lycurgus Cup in (a) transmitted and (b) refracted light, photos from the British museum free service. (c) Image TEM of metallic nanoparticles composing the Lycurgus Cup, image reprinted from the reference [10].

Several studies have been conducted to determine the composition of the cup's colored glass. In 1965, R. Brill was able to demonstrate the origin of the unexpected dichroism. In his work, the author demonstrated the presence of gold and silver minute units in the glass by

composition analysis.[9] Later, in 1990, studies of the Lycurgus Cup under Transmission Electronic Microscope (TEM) and X-ray analysis were carried out by D. J. Barber and I. C. Freestone, revealing that the Roman cup is composed of polygonal (squares) metallic particles.[10] The particles observed, in average sizes between 50-100 nm, are formed of gold, silver and copper alloy in proportion 31.2/66.2/2.5. These observations using modern techniques confirmed the results of R. Brill. (**Figure 1.1**). The studies also reveal the presence of non-metallic polygonal (squares and hexagonal) particles ranging from 15 to 100 nm corresponding to crystallized sodium chloride.[10] Therefore, the Lycurgus cup represents the oldest colored object found composed of metallic nanoparticles (NPs) although its color is probably induced by accident/hazard.

With this important historical example, it is clear that metals at the nanoscale level have a totally different appearance and color when compared to their massive counterpart. However, to form these types of colored glasses, the simple addition of metals to the glass is not enough to generate this unusual optical effect, because the metals must be reduced in specific conditions. Note that during Roman times, the reduction of metals was not known yet. In fact, R. Brill studies about Lycurgus cup supposes that this unusual optical effect would be coincidentally obtained by the presence of redox species in the glass such as iron, antimony and manganese which can participate in the gold and silver reduction under these conditions.[9] Therefore, the Lycurgus Cup can be considered as a "nano-accidental" object produced during this period.

However, it was not until the 8th century that alchemy brought an invaluable advance related to the metals' manipulation in solution. The improvement of distillation followed by the discovery of mineral acids by the well-known alchemist J. I. Hayyan (Latinization Geber) allowed the solubilization of nobel metals.[11] Through the manipulation of hydrochloric acid and nitric acid derivatives J. I. Hayyan obtained for the first time the aqua-regia known at that time as the "royal solvent" which dissolve gold and silver, but also hardly soluble non-metals such as sulfur.[2,5] This discovery influenced significantly the progress in the handling of metals for the colored glasses' preparation.

Gold was widely applied as red pigment like copper, but the latter is difficult to handle oxidizing easily and losing part of the color. One of the most famous gold-based pigments developed was known as Purple of Cassius, composed of gold nanoparticles (AuNPs) with an average size of 10-15 nm.[2] It was used to dye porcelain, ceramics or glass even before the NPs discovery. J. R. Glauber was the first researcher that informed about the preparation of Purple of Cassius using gold and tin derivatives in 1659. Twenty years later, Purple of Cassius pigment was widely used to produce red ruby glasses on a large-scale in a Postdam factory. However, in 1985 A. Cassius Junior wrote the book "*De Auro*" where is presented the preparation of purple colored glass developed by his father A. Cassius and the pigment take his name until now.[2,12] The solubilization of metals with aqua regia lead also to the development of stained glass used to build

medieval cathedrals windows, some of them were analyzed and revealed to be composed of metal particles, as well as the Lycurgus cup.[2,3]

The first famous experiments and observations in the synthesis of ruby red AuNPs were published by Michael Faraday in 1857. M. Faraday published "The Bakerian Lecture: Experimental Relations of Gold (and Other Metals) to Light" where he describes all the observations related with his important metal NPs experiments.[13] Aerosols, thin films, hydrosols composed by metals such as gold, silver, and copper but also platinum, palladium were studied in the mentioned work. For instance, M. Faraday observed the formation of ruby red AuNPs obtained by reducing tetrachloroaurate with phosphorus in a two-phase aqueous solution and their interaction with light. The conclusion about the red solutions obtained cited verbatim "*The latter, when in their finest state, often remain unchanged for many months, and have all the appearance of solutions. But they never are such, containing in fact no dissolved, but only diffused gold. The particles are easily rendered evident, by gathering the rays of the sun (or a lamp) into a cone by a lens…*" reveals the high understanding of the colloidal metal state.[13,14] Note that M. Faraday studied colloids even before the term colloid was first introduced by T. Graham a few years later in 1861 even if he did not considered M. Faraday solutions as colloids.[15] An appropriate definition of colloid, as a substance dispersed in a different phase medium was later revealed, proving the colloid state of M. Faraday gold solutions.[16]

Thanks to M. Faraday and Berzelius works among others, the colloidal nature of Purple of Cassius has been recognized by Adolf Zsigmondy who awarded the Nobel Prize in Chemistry in 1925 "for its demonstration of the heterogeneous nature of colloidal solutions and for the methods it has used". This become fundamental in the chemistry of modern colloids.[17] A. Zsigmondy developed with H. Siedentopf, the ultra microscope which allows to observe gold-based colored solutions and raises doubt about the questions of the time about colloids saying in his Nobel lecture that "*A colloidal mixture may sometimes behave like a chemical compound and has frequently simulated one*". This discovery has confirmed the colloidal nature of these solutions and can be used to determine an approximation of the particle structure including size and shape. In addition, the invention permits to observe the dynamics of colloidal solutions after disruption of the system by salts or dilution proving the formation of particles aggregates responsible for gold solutions color change from red to blue.[17]

All these discoveries open the door to the study of metallic colloids which possesses interesting chemical and physical behavior.

1.2. PHYSICO-CHEMICAL PROPERTIES OF METALLIC NANOPARTICLES

1.2.1. Optical properties: origin and understanding of nanoparticles color

The color of the gold and silver colloids covers all wavelengths of the visible spectrum. These optical properties are completely different from the bright metallic color of the raw materials. Already in the studies of M. Faraday, the diffusion of sunlight in ruby red gold colloidal solutions were reported.[13] A few years later, J. Tyndall described in detail this phenomenon, which since has been called the Tyndall or Faraday-Tyndall effect.[18] This optical phenomenon is observed when the light is dispersed through a colloid or a suspension of fine particles in all directions. The Tyndall effect is a phenomenon easily observable in nature; for example, the whitish cloudy effect produced by the scattering of visible light through fog or smoke. It is also observed when a colloidal solution is illuminated with a laser.

The light is composed of an electric and magnetic field perpendicular to each other oscillating at the same frequency. When light interacts with matter, the negative charges located in atoms/molecules began to oscillate and create an electrical dipole emitting electromagnetic radiation. Therefore, the interaction of light with matter provides relevant dynamic and structural information of the matter. Several phenomena occur when light interact with matter, namely: absorption, refraction (change of direction after contact with matter), diffraction (change of density of the incident wave), reflection (after contact within the material, the wave changes of direction) or scattering (incident wave leaves in all directions) producing different optical effects (**Figure 1.2**). In the case of small particles, depending on their size, the interaction modes can be notably divergent. Indeed, when the particles are smaller than the wavelength, a clear colored solution is observed while the solution is opaque when the particle size is greater than the wavelength.

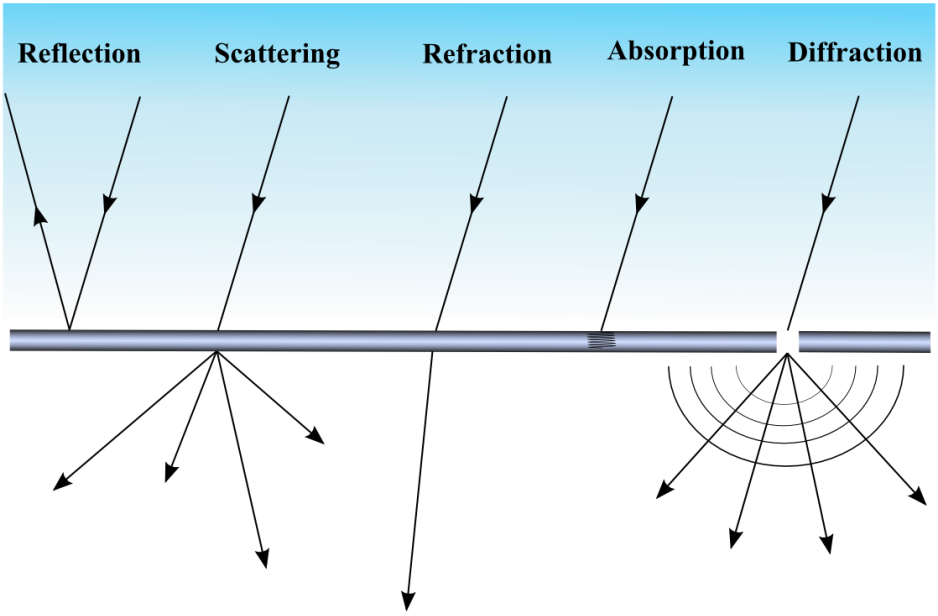

Figure 1.2. The different pathways resulting from the interaction of light with matter.

To explain in more detail where the color of NPs is originated, it is necessary to focus on the phenomenon of electromagnetic wave propagation in matter, which is described by fundamental physical laws: Maxwell's equations.[19,20] The application of Maxwell's equations in the context of light interaction with small spheres has been theoretically developed by several scientists such as J. J. Thomson, L. Lorentz, F. Hasenörl and F. Ehrenhalf.[21] However, the origin of the color was understood thanks to the Maxwell equations resolution by Gustav Mie in 1908 based on the L. Rayleigh, F. Hasenörl and L. Lorenz works.[21,22] The results of G. Mie provided theoretical solutions to the experimental observations related to colloid science, and even contributed solutions to natural macroscopic phenomena. Thought application of Maxwell's equations with spherical coordinates, G. Mie exposes a theory about the scattering of light by spherical particles. Indeed, this theory makes it possible to explain in which directions the diffusion of light is the most intense and determine a pattern of emission independently of the intensity of the wave and the nature of the particle. This light pattern intensity depends on the size of the particle studied. More specifically, when the wavelength (λ) is much smaller than the size diameter (d) of the particle ($\lambda << d$), the scattering pattern is asymmetric predominating forward explaining the clouds white color and shape for example. In the case of metallic nanoparticles, ($\lambda >> d$), the interaction light/particles induce an electric dipole generated as a consequence of the conduction electrons displacement in opposite direction to the incident wave electric field. Then, a restorative force is generated in the particle promoting the return to equilibrium, which was altered by the charge distortion. In the situation for which the induced dipole and the restorative force are coupled, a plasmon resonance occurs.[23] In other words, Localized Surface Plasmon

Resonance (LSPR) is the collective oscillation of the metallic NPs conduction electrons when they are illuminated with the appropriate wavelength (**Figure 1.3**).[24,25]

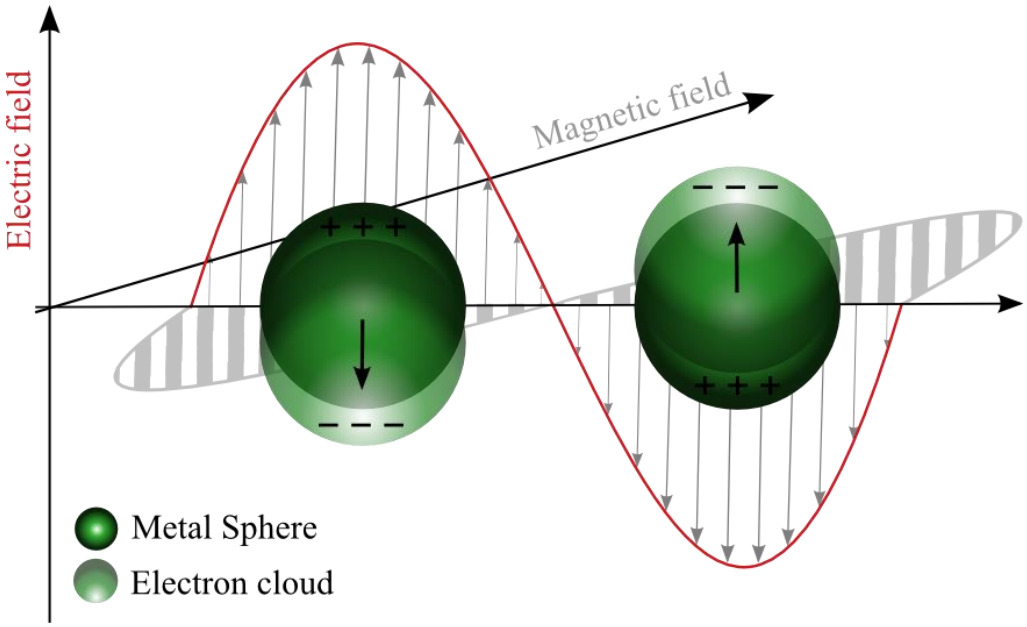

Figure 1.3. Localized Surface Plasmon Resonance of metallic nanoparticles under light illumination.

In the case of gold and silver NPs, the resonance is maximum, and its frequency occurs in the visible field of the electromagnetic spectrum producing a LSPR. The NPs' LSPR has the ability to absorb certain frequencies of the incident light and transmit the unabsorbed frequencies associated with a certain color. Note that the observed color of colloidal suspensions is associated with the part of light transmitted by the particle.[26] For instance, if we consider AuNPs of size d <30 nm, the LSPR absorbs light from the visible area of the blue-green electromagnetic spectrum and produces red reflected light, then the colloidal solution takes an intense red color. The resonance frequency, absorption bandwidth and the LSPR's energy depend on composition, size, shape, aspect ratio as well as the surrounding medium of metallic NPs.

Based on Mie's theory, for the case of a spherical metal particle, **Equation 1.1** can be applied to determinate the cross-section extinction Cext which is the sum of absorption and scattering[24,27]:

$$Cext = \frac{24\pi^2 R^2 {\varepsilon_m}^{2/3}}{\lambda} \frac{\varepsilon_2}{(\varepsilon_1 + 2\varepsilon_m)^2 + \varepsilon_2^2} \quad \textbf{(Equation 1.1)}$$

Where Cext is the cross-section extinction (sum of absorption and scattering), ε_m is the dielectric constant of the medium, *R* the radius of the sphere, ε_1 and ε_2 are the real and imaginary components of the NPs dielectric function and, λ is the wavelength of the incident radiation. The

cross-section extinction is strongly dependent on several factors such as the dielectric constant of the solvent, the temperature, the composition, the surface charge (stabilizing agents, ligands and indirectly the dielectric charge of the NPs environment), the size and shape of the NPs.

The analysis of Ultraviolet-Visible (UV-Vis) spectroscopy profile permit to obtain precise information about the nanoparticle size and shape. The isotropic NPs, which have the same properties in all directions are defined by a well-defined UV-Vis band in the corresponding LSPR. In the case of gold and silver small size nanospheres, the resonance condition depends mainly on the metal dielectric functions and the medium. In the case of larger nanospheres a red-shift is observe according to NPs size. For instance, 20 nm diameter aqueous AgNPs have a LSPR at a wavelength of 405 nm, and when the size increases to 120 nm, the LSPR red shifts to 500 nm (**Figure 1.4**).[28,29] As the scattering cross section increase (increasing size), radiative damping and different higher multipoles occur in the resonance producing significantly broadened of LSPR band.

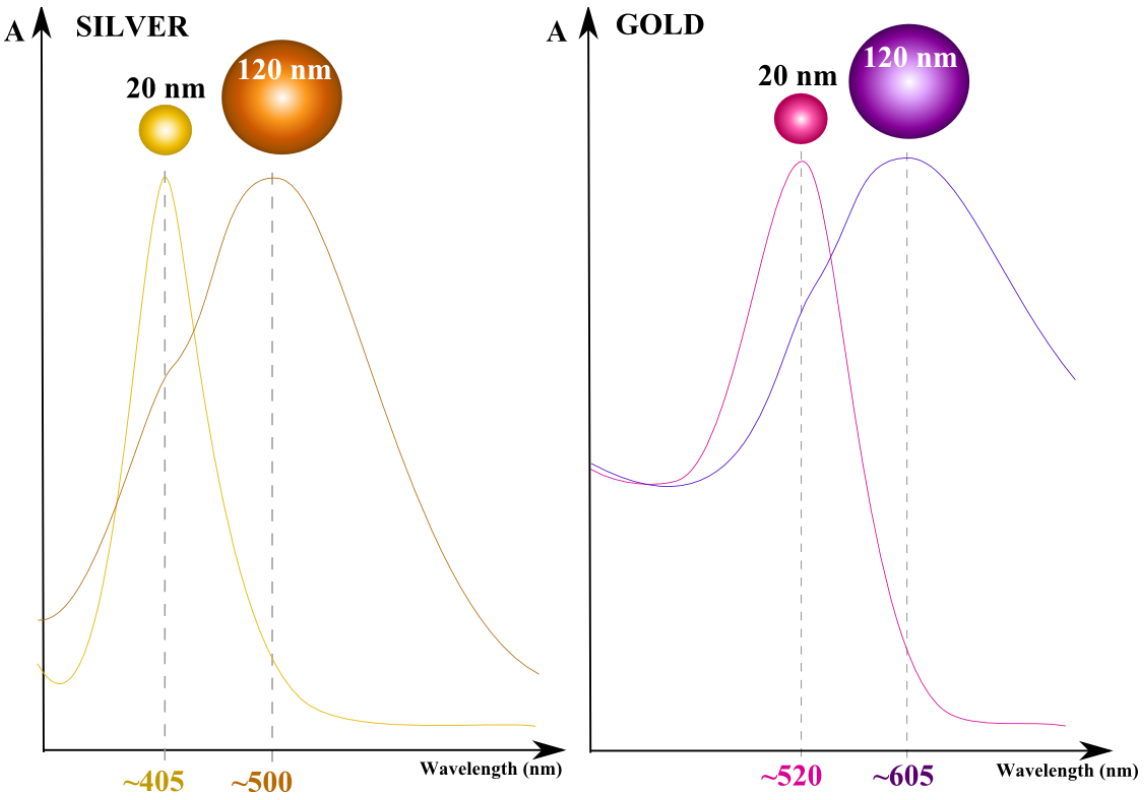

Figure 1.4. UV-Vis spectra profile of metallic NPs in function of their size and composition. (Left) Silver NPs and (Right) gold NPs based on reference [28, 29].

Contrary, anisotropic NPs with well-defined shape are characterized by several LSPR bands corresponding to different excitation modes linked with their shape. These excitation modes correspond to the electromagnetic dipoles present in the NPs according to their shape (**Figure 1.5**).

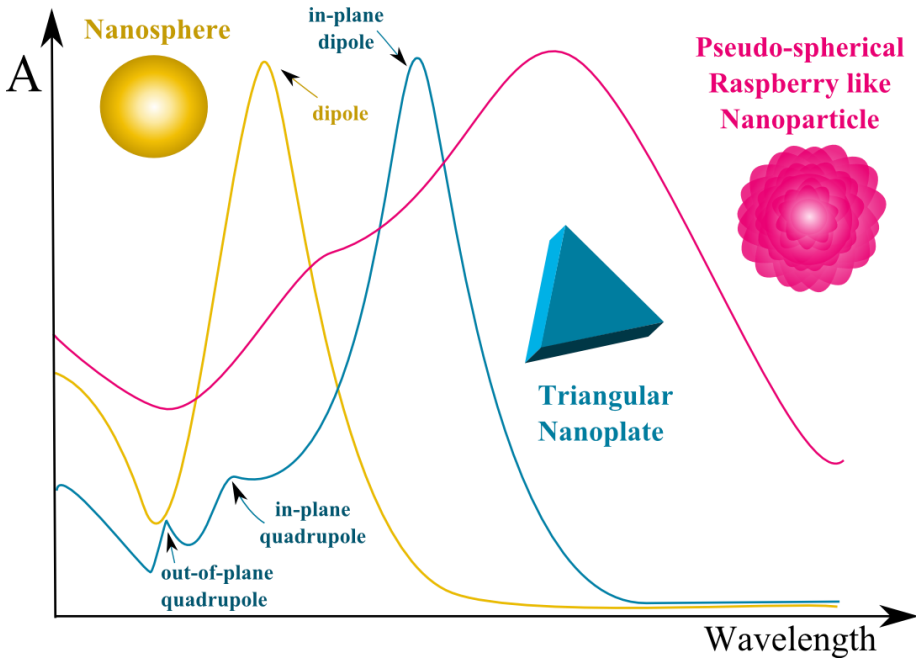

Figure 1.5. Different plasmon band evolution in function of the shape of nanoparticles.

For instance, silver and gold nanotriangles present both dipole and quadrupole plasmon resonances depending on their characteristics (size, shape, medium etc…).[30] Furthermore, nanotriangles also present out of plane extinction mode related with their pointed corners that create high electromagnetic energy hot spots which are detectable in UV-Vis spectroscopy.[30]

Another interesting geometry for gold and silver NPs is nano-stars or multi-tips NPs also known as raspberry like, urchin like NPs. These fascinating geometries bring a high number of hot spots per particle, which arouses a growing interest in the development of new synthetic methodologies allowing the production of theses advantageous geometries. Also, nano-star or multi-tip NPs plasmon resonances result from the hybridization of individual tips and NPs core plasmons.[31] Furthermore, multi-tip NPs are in particular interest once the sharp tips produce an enhancement of the local electromagnetic field making them excellent candidates for the detection of molecules in optical applications such as SERS.[32,33]

1.2.2. Chemical properties of gold and silver nanoparticles

It has been known for millennia that the silver metal is unstable at room temperature and generates an oxide layer at its surface. Indeed, silver is the metal that has the highest electrical and thermal conductivity being easily sensitive to oxidation in open atmosphere. The environment humidity forms a thin aqueous layer on the metal surface favoring the adsorption of atmospheric gases such as nitrates, oxides, carbonates, sulphites among others.[34] These ions and molecules can participate in the metal corrosion by promoting the dissolution of the metal and forming an metal oxide film on its surface.

Generally, the metal NPs chemical properties are directly linked to the metal redox standard potential. For example, the difference between the standard reduction potential of silver ($E°_{Ag+/Ag}$ = + 0.80 V) and oxygen in normal conditions ($E°_{O2/H2O}$ = + 1.23 V) shows the thermodynamically favorable character of metallic silver oxidation in an open atmosphere. This electrochemical property is present in the raw metal but also at nanometric state, which makes silver nanoparticles (AgNPs) sensitive to their environment and easily oxidizable. This feature makes them toxic to many microorganisms and may be an advantage in antibacterial and antifungal applications among others.[35] Unlike silver, gold presents a higher standard reduction potential ($E°_{Au3+/Au}$ = + 1.50 V) which makes this metal more resistant to corrosion and stable at ambient air.

Compared with the AgNPs' corrosion, AuNPs being more resistant to oxidation and biocompatible, are extensively used in biological applications. For instance, spherical AuNPs are primarily used as an X-ray contrast agent for the detection of cancer.[36] Due to their photo-resistance, AuNPs can also be used in long-term analyzes with great efficiency. Moreover, the cross-section of diffusion of the AuNPs is 10^6 times higher than that of the fluorescent molecules' emission.

In addition to the specific oxidation tendency, the reactivity of metal NPs are strongly linked with the metal surface affinity. According to Pearson acid/base theory, gold and silver NPs present affinity towards soft and borderline donating atoms (oxygen, nitrogen and specially sulfur).[37] As consequence, thiols, amines and carboxylates containing molecules can be employed to functionalize metallic NPs leading to new hybrid funcionalities.[38] Thiolate functions are the most reactive group to gold and silver surfaces, then amines and finally carboxylates. The NPs chemical affinities towards the functional groups allow the production of organic modifications on the NPs surface through different metal-ligand affinity which makes them excellent carriers of organic molecules, amino acids, biomolecules and polymers.[39,40]

1.3. SYNTHESIS OF METALLIC NANOPARTICLES

In general, there are two main paths to synthetize metallic NPs. In one hand, the top-down strategy starts with raw material which can be mechanically shocked, compressed or rubbed, causing condensation and spraying of powder leading to the production of nanomaterials.[3] In the other hand, the bottom-up method, diametrically opposite technique, can also generate NPs from precursor metal atoms used as building blocks in the solid and liquid state. Based on the fact that the metallic NPs developed in this doctoral thesis were obtained through bottom-up strategies in the liquid state, henceforth we will continue the discussion based on these techniques. Many liquid phase methods exist to synthetize NPs such as alkaline precipitation, co-precipitation, sol-gel method, or chemical reduction among others.

Bottom-up strategies generally include the reduction of metallic precursors in solution by a reducing agent (molecules, temperature… etc). In addition to reducing agents, it is mandatory to apply additional agents in order to stabilize the metallic NPs in solution, otherwise the particles, due to their high surface to volume ratio, tend to aggregate in the raw material. The different methods to stabilize metallic NPs can be classified into two large families: electrostatic and steric stabilization.[41] The electrostatic stabilization comes from the electrostatic repulsion between NPs charge when they present a double layer of electric charge. This double layer charge, which presents a total net charge, is produced by charged species interacting with the NPs surface. This total net charge provides electrostatic repulsion between the metallic NPs in dissolution.

In contrast, steric stabilization is provided by a physical barrier created through the adsorption of high molecular weight molecules for example as polymers or hydrophobic molecules. In this way, stability is given to the colloid without attending to charge terms. It should be mentioned that both stabilization methods could exist in the same colloidal system.

Furthermore, the mechanism of NPs formation is very studied but not fully understood yet by the scientific community due to its complexity and lack of observation tools.[42] Several theories have been developed to extrapolate the different phenomena involved during the formation of NPs but there are still some questions about the first stage of NPs formation which remain under discussion by the nano-technological community. The birth phase of NPs formation is composed of two main stages: nucleation and growth processes. The classical nucleation and growth theory, based on a phenomenological approach, describes the NPs formation with macroscopic parameters, and makes it possible to present a good approximation of the system.[41] Considering the case of nucleation of a solid phase in a liquid medium, the reduction of the metal precursor produces metallic clusters which form nuclei with specific size and shape composed of a few atoms.[42] These nuclei then act as a specific reduction site for the NPs growth. Additionally, nucleation can be classified into two different processes: homogeneous nucleation where nuclei

have the same probability of formation in volume; and the heterogeneous nucleation where is formed from sites such as impurities, dislocations, surface defects, bubbles, grain boundaries. The nucleation can be considered as the first stage of crystallization, in others word, the creation of a new physical phase. The classical nucleation's theory remains one of the most reproducible and representative theories of this phenomenon. This theory highlighted during the 20th century by M. Volmer, A. Weber, R. Becker, W. Döring, J. Frenkel or J. B. Zeldovich among others is mainly based on a phenomenological and kinetic approach using macroscopic parameters such as surface tension or density to describe the system. In this theory, it is exposed that homogeneous nucleation is allowed thanks to the variation of two energies: thermodynamic energy, which is associated with a change of the free energy of crystal formation, and a kinetic energy that depends on the diffusion of atoms to nuclei. The total Gibbs free energy variation ΔG is composed of the sum of the volume energy and the surface energy and can be obtained by the following **Equation 1.2:**

$$\Delta G = \frac{4}{3}\pi r^3 \Delta G_v + 4\pi r^2 \gamma \qquad \textbf{Equation 1.2}$$

Where r is the radius of the spherical nuclei, ΔG_v the free energy of the crystal (which depends on the energetic volume term) and γ the surface tension energy (which depends on the energetic surface term).[41,43] In the crystal creation stage where the nucleation is favored, the energetic term of the volume is negative due to the decrease of the free energy of the crystal ΔG_v, while the surface energy term is positive due to the increase of the surface energy created by the presence of the solid phase (**Figure 1.6**). Nucleation is favorable when the total free energy of Gibbs reaches a maximum associated with the radius nuclei sufficiently stable in solution. Typically, when nucleis reach the critical radius r^c, they can survive in solution, otherwise they are immediately redissolved. This critical radius is reached when the total free energy is at its maximum ($\frac{d\Delta G}{dr} = 0$).[43] The critical global free energy ΔG^c obtained can be defined by **Equations 1.3**:

$$\frac{d\Delta G}{dr} = 0 \quad \leftrightarrow \quad r^c = \frac{-2\gamma}{\Delta G_v} \quad \leftrightarrow \quad \Delta G^c = \frac{4}{3}\pi\gamma(r^c)^2 = \frac{16\pi\gamma^3}{3(\Delta G_v)^2} \qquad \textbf{Equations 1.3}$$

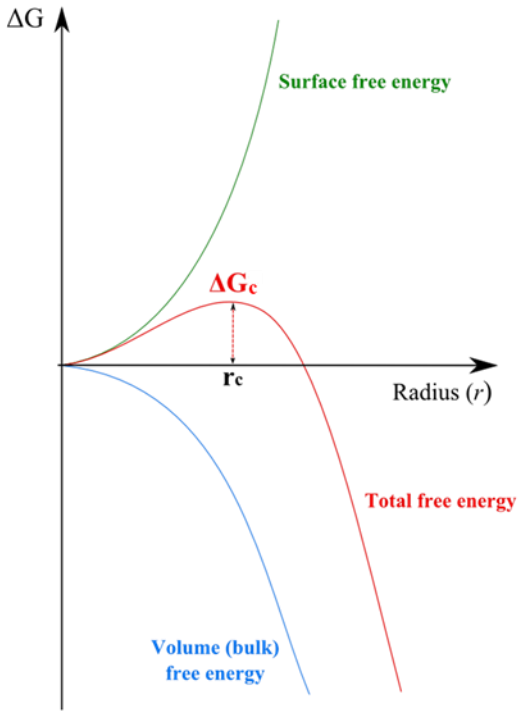

Figure 1.6. Variation of the Gibbs free energy in function of the radius of the spherical nuclei.

The nucleation driving force is induced by the free crystal energy ΔG_v, which depends on several parameters such as Boltzmann constant k_B, temperature T, molar volume υ, supersaturation S, and where C and Cs are the precursor concentration and solubility concentration respectively (**Equation 1.4**).

$$\Delta G_{\upsilon} = \frac{-k_B T ln(S)}{\upsilon} = \frac{-k_B T}{\upsilon} \ln(\frac{C}{Cs}) \qquad \textbf{Equation 1.4}$$

Therefore, nucleation and growth can be understood according to the atomic concentration with time. A first mechanism was exposed in the 1950's by V. LaMer and R. Dinegar through analysis of sulfur soils precipitation and can be presented in the so-called LaMer curve (**Figure 1.7**).[44] In this theory, nucleation and growth are divided into three different stages: atom production, nucleation from atoms aggregation, and nanocrystal growth. In the first stage, the metallic atoms are reduced. When the supersaturation point is exceeded (C>Cs), in the second stage the atoms begin to aggregate forming stable nuclei via auto or homogeneous nucleation. Finally, the supersaturation falls, and no further nucleation events occur.[43,44] Then, nuclei grow via continuous atoms addition.

During the last century, several theories have appeared explaining the nucleation and growth process beyond the different stages of the LaMer curve. All these proposals can be classified as atom mediated nucleation and growth models. Diffusion-limited growth,[45] Finke-Watzky mechanism,[46] reaction-limited growth,[47] Ostwald ripening,[48] digestive ripening[49] among others have been developed to explain the different growth processes.[44] With the nucleation and growth theories discussed above, it is possible to obtain solid explanations about the formation mechanism of the different morphologies (isotropic or anisotropic) of metallic NPs. In addition, thanks to the development of these theories, the introduction of experimental variations during the synthetic processes was achieved by kinetic or thermodynamic crystal growth changes. Serious and precise improvements were reached to control NPs size and shape.

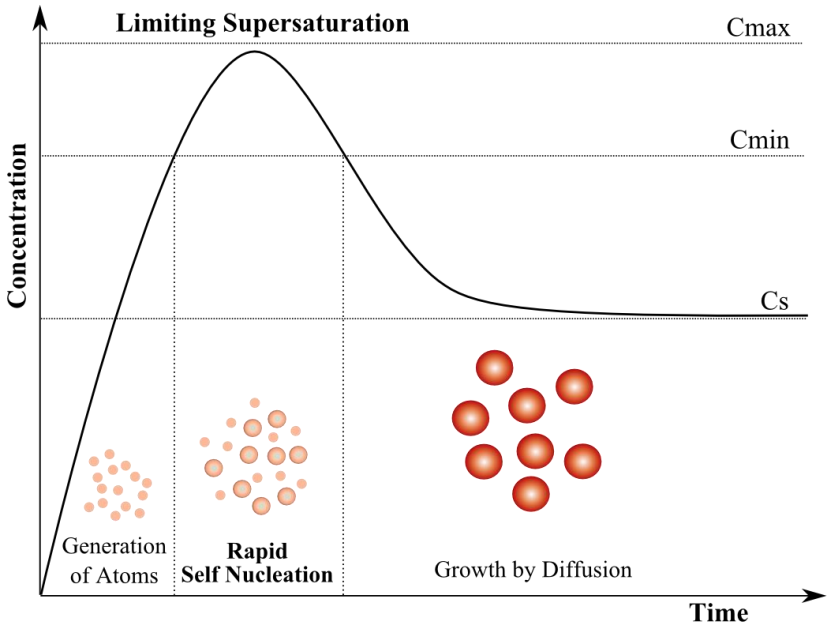

Figure 1.7. Schematic LaMer plot, atom concentration in function of time, representing the different stage of nucleation and growth processes.

However, besides to nucleation and growth processes via atoms addition, an increasing number of metal NPs synthetic processes have appeared in the last decades, which cannot be explained through atom mediated growth theories. With the improvement of electronic microscopy technics, it has been possible a more detailed visualization of crystalline structures obtained by growth processes. These growth processes are influenced by the NPs addition rather than atoms or monomers as explained by the theories mentioned above. The final products obtained by these mechanisms usually have a mesocrystalline or polycrystalline structure. In these non-classical nucleation and growth models, the nuclei reach a stable size which is used as a building block for the final nanomaterial structure. Generically, the NPs addition forming meso or polycrystal structures can occur via an oriented attachment,[50] coalescence[51] or both mechanisms (**Figure 1.8**).

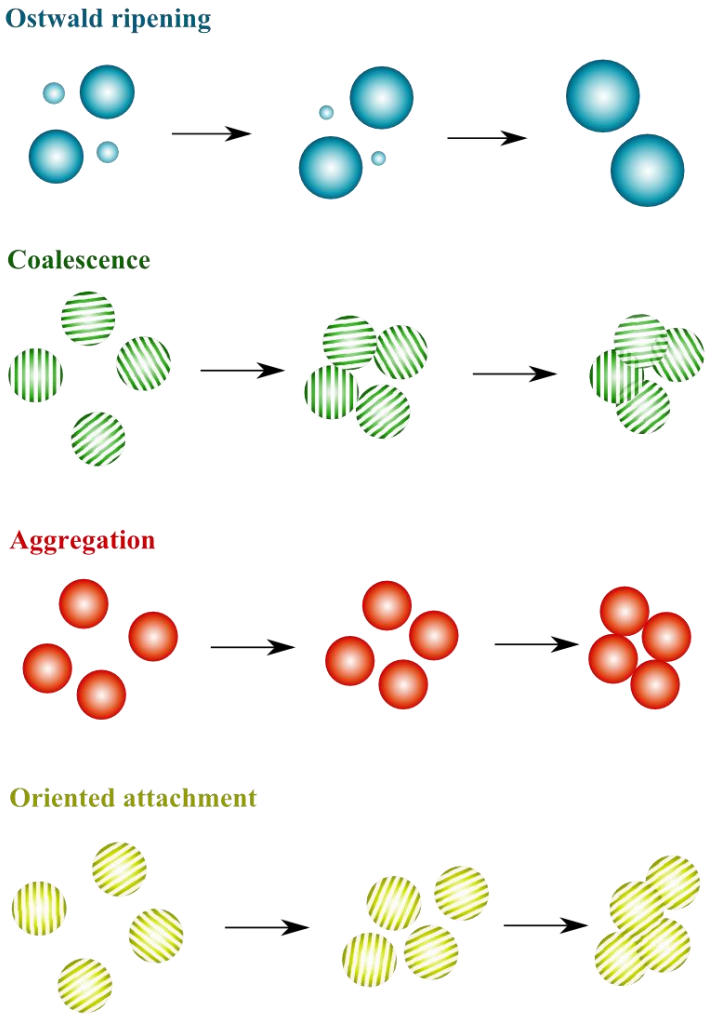

Figure 1.8. Representation of the different NPs growth evolution: Ostwald Ripening, Coalescence, Aggregation and Orientated Attachment. Crystalline planes are represented in NPs stripes.

In an experimental point of view, there are two large aqueous synthetic methods to form silver and gold NPs found in literature: seed-mediated growth and one-pot methodologies. Seed-mediated growth process involves the production of seeds (larger nuclei) and their subsequent growth to metallic NPs in two differentiated synthetic steps.[52] The separation between the nucleation and growth process allows greater control over the final product obtained, producing higher quality metallic NPs. However, on many situations, successive synthetic steps are required with tedious experimental protocols to produce the desired geometry and size. Conversely, one-pot synthesis involves the production of metallic NPs in a single step, which requires the control of nucleation and growth at the same time. Generally, the atomic control in the metallic NPs production of desired size and shape is more complicated in this way. Currently a tremendous scientific effort is being developed to allow the control in NPs synthesis by simpler methods such as one-pot, once the production time is reduced, as well as waste production.

1.4. STATE OF THE ART: APPLICATIONS OF SILVER AND GOLD NANOPARTICLES

Both, gold and silver have a long history of medical uses. As an example, drinking gold solutions was very popular during the Middle Ages with the physicist Paracelsus which developed a gold solution called *Aurum Potabile* as a long-life elixir proposes.[5,11]

In the case of silver, one of the first medical uses with silver nitrate appeared for the treatment of ulcers and wounds cauterization agent.[4] It can be noted, that since the ancient times, gold and silver chemical properties have been recognized and used. In a medical and toxicological approach, the initial properties observed in formulations based on gold and silver are strongly linked to their chemical properties. As reported in Section 1.2, their different behavior to oxidation, and surface affinity have allowed the implementation of gold and silver NPs in modern formulations, but with different properties or applications.

In the case of AuNPs, their large ratio surface to volume, their excellent bio compatibility, low toxicity, and the easy and well established controlled synthetic methods, make this material an invaluable tool for future biomedical applications.[53] As an example, AuNPs have been successfully implemented in controlled release systems of commercial anticancer drugs[54] as doxorubicin[55] or paclitaxel[56] for example. Based on the successful application of AuNPs in drug release, efforts are currently being investigated in the bioconjugation of AuNPs with biomolecules as therapeutic agents for future alternatives to the treatment of diseases.

With the tremendous advances in biochemistry science, a growing number of biomolecules with interesting antibacterial and anti-cancer properties are being used. For example, the Lectin (EHL) is a protein found in a flower called Winter Aconite that blooms late in the winter. It is a dimer protein rich in asparagine/aspartic acid, glutamine and leucine. This toxic biomolecule is a type II Ribosome Inactivating Protein (RIP) which induces the glycoside bond break in the ribosome resulting from inactivation of lipid synthesis and cell death. EHL also has a strong affinity with certain carbohydrates including N-acetyl-glucosamine characteristic of O-glycans cancers and therefore EHL can be exploited as a potential anticancer compound. EHL protein has also been functionalized with sterically stabilized AuNPs in an aqueous medium by thiolated and acetylated PEG polymers coated with lactose.[57] However, it is interesting to synthesize bioconjugate directly in order to eliminate the presence of external molecules that could interfere with the toxicological results. Lectin gold based nanoconjugate can be synthetize by ligand exchange reaction from AuNPs stabilized with citrate molecule.

The best-known and most studied AuNPs synthesis is the famous "Turkevich method" developed by J.Turkevich in 1951.[58] This one-pot synthesis offers a series of advantages over other synthetic processes. First, as the process is performed in aqueous phase, the NPs obtained can be implemented in applications with biochemical focus without the need of additional purification processes. Second, the resulting AuNPs are stabilized by surface adsorption of citrate molecules through Van der Walls forces. This weak interaction allows to functionalize easily the AuNPs with ligands having more affinity towards gold than citrate molecules. This strategy, so-called ligand exchange is applied to anneal biomolecules on AuNPs surface. Biomolecules such as proteins, immunoglobulins, or DNA have thiolated, or aminated functions with increased affinity to the metal surface when compared with citrate.[59] The proteins having amino acids with sulfur (cysteine) and amino (histidine, lysine etc.) functions can interact covalently with the metal surface.

The adsorption of proteins on the surface of the NPs modifies the zeta potential and stabilizes the NPs by steric stabilization due to the large size of the proteins. Due to the sensitivity of proteins and biomolecules to their environment, they can quickly lose their function. It is important to develop new synthetic techniques which not deactivate biomolecules while stabilizing NPs and achieving the functionalization in a compatible medium with proteins.

In the case of Lectin protein discussed above, the protein has essential amino acids with amine functions which can be easily functionalized by ligand exchange at the surface of citrate-stabilized AuNPs being a potential anticancer system. In **Chapter 2** the first description of the synthesis and toxicological properties of AuNPs bioconjugates with Lectin will be presented.

Unlike the applications concerning AuNPs, silver in the colloidal state is remarked as an agent with relatively high toxicity for most organisms.[60,61] Even though this inherent toxicity is highly dependent on NPs concentration and organisms studied, the applications of silver colloids in nanomedicine are more limited. Since antiquity, the properties of silver (for example silver nitrate) were exploited as antibacterial and healing agent.[4] At present, the toxic mechanisms that involve the silver ion towards different organisms are known with more details but still under discussions.[60] Although the exact mechanism is not yet understood, studies have been conducted against strains of *E. coli* and *S. aureus* bacteria and have revealed some mechanistic indications through the TEM microscope.[62,63] It has been observed that the interaction of silver ions with bacteria caused structural damages in the bacteria's membrane through the interaction of silver ions and thiols present in bacterial proteins membrane. Stronger activity has been observed against Gram-negative bacteria compared to *S. aureus*, which is related to the presence of large layer of peptidoglycans on their surface.[63] It has also been observed that the DNA material condenses after interaction with silver ions and it has been concluded that silver ions block the mechanisms by which bacteria pass to divide.[62] The development of new silver-based

antibacterial/antifungal is constantly increasing due to the need to fight bacteria that become resistant to antibiotics. The scientific community have observed that the AgNPs can provide advantages over the application of Ag^+ derivatives ($AgNO_3$). For instance, AgNPs can be used as silver ion reservoir controlling the ions release by partial oxidation.[64,65] A great deal of work on the subject has been published using spherical NPs as an antibacterial agent against different microorganisms: bacteria, fungi and algae, eukaryotic cells, and multicellular organisms.[66] In addition, studies have been conducted and revealed that the use of AgNPs increase the antibacterial effect of several antibiotics such as amoxicillin,[67] vancomycin and others,[68] proving the synergistic effect of AgNPs with antibiotics against bacteria. AgNPs through their chemical reactivity allow their functionalization with antibiotics, which could increase their therapeutic potential. The **Chapter 3** presents the advances in this area with the development of a new process for the production of silver and gold NPs, using only tetracycline antibiotic as a reducing agent in the presence of sodium hydroxide.

As previously stated, silver nitrate and AgNPs have high antibacterial potency which may have advantages against several pathogenic microorganisms. An attractive route to increase the antibacterial properties of AgNPs, in addition to the organic functionalization, lies in the geometrical modification of the NPs.[69] As consequence of NPs shape or size changes, different crystallographic plans are exposed in the NPs surface. Furthermore, electrochemical studies have revealed that oxidative species adsorb on specific surface facets of NPs, such as (111) and (100).[70] Subsequent studies have been done by TEM and HAADF-STEM on bacteria and have proven that NPs of 1 to 10 nm having (111) facets inhibit bacterial wall growth.[71] Pal et al. have also observed that the bactericidal activity is related to the shape of the NPs, and is incremented with higher (111) facets.[60] Small NPs with (111) planes such as nanoplates, nano-hexagonal, nano-octaedral, had a greater bactericidal action against Gram-negative strains.[71]

Among all the geometries reported in the literature, triangular nanoplates are one of the shapes that present a higher surface area formed by crystalline planes (111). As a result, triangular nanoplates are extremely sensitive to oxidation even by molecular oxygen which limits its applications. Mirkin et al. group have developed a process for coating silver nanoprisms with a thin layer of finely controlled silica, allowing the application of these nanomaterials.[72] However silver triangular nanostructures covered with silica with antimicrobial proposals have never been tested before and could be a potential tool to control the oxidation of triangular nanoplates. It should be noted that the direct application of silver nanoplates or nanotriangles without silica coating has been reported, highlighting their increased antibacterial properties when compared to spheres and rods.[60] But its inherent re-dissolution processes hinder its later rational application in more sophisticate formulations (e. g. functionalization with antibiotics). In **Chapter 4** are

presented the advances obtained in this area with a silver nanoprisms synthetic procedure for antibacterial applications.

In addition to the biomedical applications developed using gold and silver NPs, these colloid solutions can be used as well as sensors of molecules, ions, or biomolecules based on their excellent optical properties. We have seen that the LSPR frequency of gold and silver NPs is strongly dependent on the size, the surrounding environment and spatial disposition frequency of surface plasmon resonance among others factor. As a consequence, gold and silver colloids have different extinction coefficients and color in the visible region of the spectrum. These optoelectronic changes are highly related to the spacial arrangement of NPs in solution. Therefore, aggregation of NPs leads to a change of color (yellow to brown for AgNPs and red to blue for AuNPs from well-dispersed to aggregated ones, respectively). In this way, the rational design of analytes interaction with the NPs surrounding can produce a profound naked eye spectral change. Furthermore, this simple and low-cost strategy promote considerable attention about sensing approaches based on NPs aggregation (colorimetric assays).[73]

Therefore, it is possible to synthetize NPs presenting controlled aggregation in response to a target analyte. In this regard, AgNPs, exhibit the best light-matter interaction compared to other metals and sweep a wider area of the visible spectrum.[74,75] Our group, published in 2013 an excellent example of a colorimetric nano-strategy with the synthesis of AuNPs functionalized with a thiol terminated fluorescein derivative. This hybrid gold colloid showed high affinity towards Hg(II). After the selective interaction with this heavy metal, the aggregation of NPs occurs through formation of NPs chain-like structures. The ion detection by naked eye color

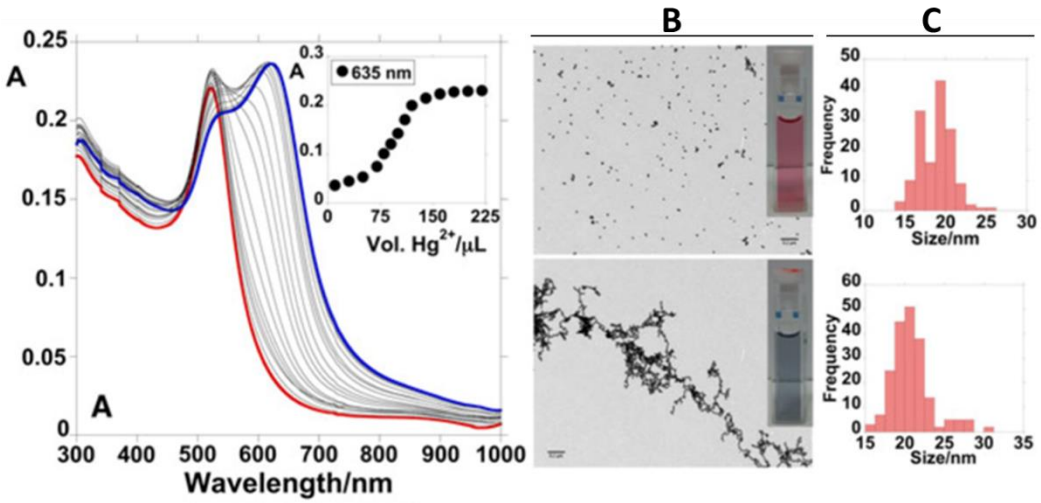

Figure 1.9. Aggregation response of AuNPs functionalized with thiol terminated fluorescein derivative in presence of mercury ions in solution. (A) AuNPs UV-Vis spectra profile with the addition of Hg^{2+} in solution. (B) Images TEM of AuNPs (up) before and (down) after mercury detection showing aggregation of nanoparticles by chain like formation. (C) Corresponding size histograms of AuNPs (up) before and (down) after mercury detection. Figure adapted from the reference [76].

changes (red to blue) was possible in a ppm range (**Figure 1.9**).[76] As part of this doctoral thesis, **Chapter 3** deals with the detection of aluminum ions by AuNPs and AgNPs aggregation.

NPs can be functionalized by many molecules (biomolecules, organic molecules, sugars) to allow the detection of ions, heavy metals, pH, or dielectric environment among others.[77] But Ag and AuNPs can not only be functionalized with synthetic organic molecules with aggregation sensor approach. In other examples, bioconjugates sensors composed of AuNPs functionalized with oligonucleotides were developed by J. J. Storhoff,[78] C. A. Mirkin,[79] R. L. Letsinger[80] and P. G. Schutz.[81] This bioconjugate makes it possible to identify precise DNA sequences complementary to the oligonucleotides present on the surface of the NPs by macromolecular assembly causing NPs aggregation.

More innovative applications, flowing from the electronic properties of the gold and silver NPs, introduce improvements in the science of chemical detection. As a result of the interaction of light and matter, 1 out of 10^7 photons is inelastically scattered. This feature is called the Raman effect.[82] This effect was predicted in 1923 by A. Smekal and then independently discovered in 1928 by physicists Chandrashekhara Venkata Râman, India and Leonid Mandelstam, Russia.[83,84] In 1930, C. V. Râman won the Nobel Prize in Physics for his work on the diffusion of light and the discovery of the Raman effect.

Raman spectroscopy is a technique based on the inelastic scattering of light and widely used in the characterization of molecules and detection of analytes by identifying the vibration bands corresponding to Raman active modes.[85] The most complex in the art is related to the lower intensity in Raman scattering compared to the light scattering produced by Rayleigh effect. But in 1973 P.J. Hendra and A.J. McQuillan, exploring the Raman spectra of pyridine adsorbed on electrochemically roughened silver, gave rise to the foundations of the modern Surface Enhancement Raman Spectroscopy (SERS) technique used to increase the Raman signal of molecules adsorbed on rough metal surfaces or nanostructures.[86] The exact mechanism of the enhancement effect of SERS is still a matter of debate, but either way, both gold and silver surfaces have showed high activity as SERS support.[87]

Although the AgNPs usually exhibits the highest SERS activity, the sensitivity to oxidation discussed above may limit the actual SERS application of silver nanostructures. Therefore, nanomaterials derived from gold have been explored more extensively for SERS purposes. Since the first reports about the enhancement of Raman signal by AuNPs, remarkable advances have been informed. For instance, X. Li and coworkers noted that an enhancement factor maximum was reached for AuNPs around 50 nm of average size.[88] Furthermore, it have been pointed that AuNPs geometrical modifications induce strong SERS enhancement factors when compared with the spherical ones.[89] The reason lies in the presence of corners or points present in the NPs, which generates hot-spots where the LSRP energy is concentrated producing improvements in SERS

response (**Figure 1.10**). Among all the geometries known for gold with improvements SERS response, star or multi-tip AuNPs has gained attention in the last decade, as a consequence of the presence of multiple tips per NPs.[90]

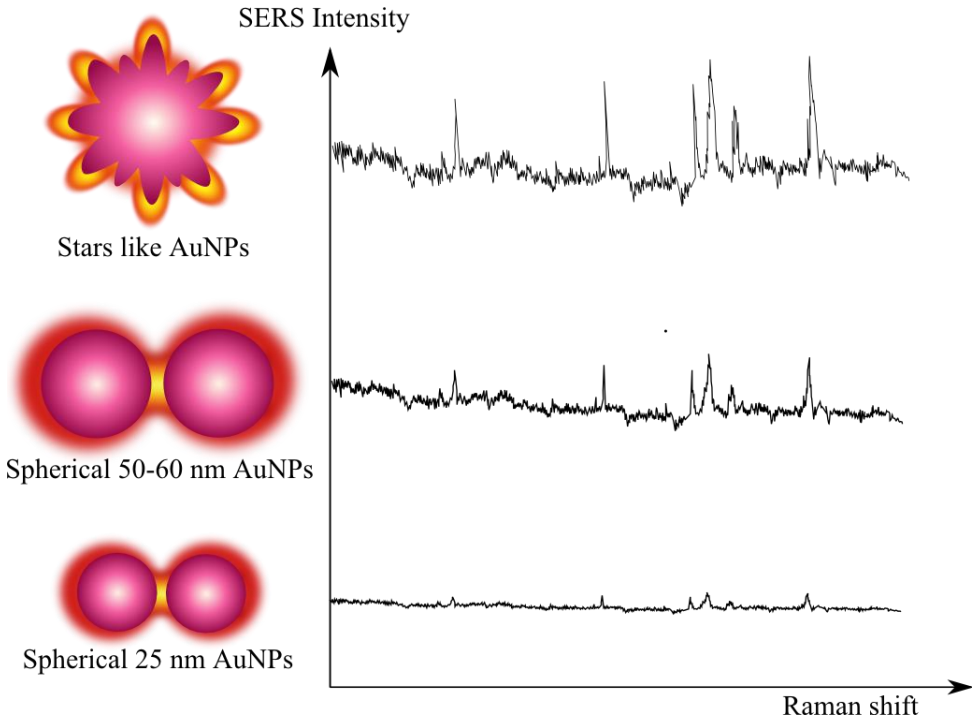

Figure 1.10. SERS response profile in function of the size and shape of AuNPs. The yellow color corresponds to the presence of hot spot in NPs.

Multi-tip or star AuNPs have been successfully applied as high-performance SERS support for the detection of organic molecules, biomolecules and even for biomedical applications.[91] Despite its wonderful properties with numerous applications, the synthesis of this type gold's geometry at the nanoscale level, usually requires laborious synthetic processes with subsequent growth steps, application of toxic stabilizing and reducing species, or require considerable energetic contribution (US irradiation, high temperature).[92–95]

Eco-friendlier multi-tip AuNPs synthesis was recently developed. For example, J. Fang et al. reported the synthesis of multi-tip "sea-urchin" like gold meso-particles obtained using iron powder as Au(III) reducer via a secondary nucleation and growth process (**Figure 1.11**).[96]

Despite the fact that metallic iron has shown interesting properties to apply in Au(III) reduction to obtain NPs, in base to our best knowledge, iron salts were never applied in synthesis of AuNPs. The use of ionic iron species instead of the metallic iron presents an enormous advantage due to the attractive possibility of altering the formal Redox potential through the complex formation with specific molecules. Specifically, Fe^{3+}/Fe^{2+} couple shifts markedly in the

negative direction through complex formation with oxalate, EDTA and citrate.[97] This chemical behavior should be able to be exploited to modulate AuNPs synthesis using Fe(II) as reducer.

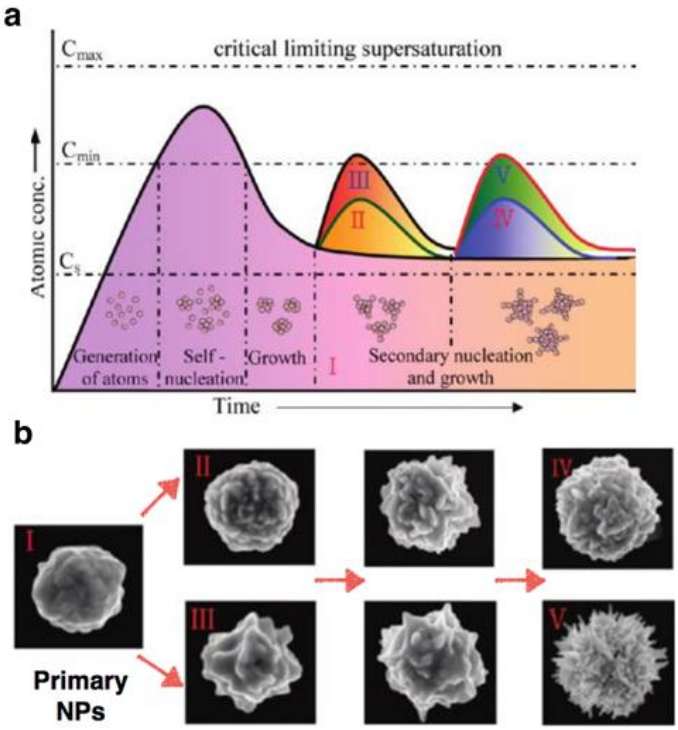

Figure 1.11. (a) Schematic plot of a gold atom concentration versus time illustrating the growth of mesoparticles. (b) SEM images of different surface topographies, types I-V, synthesized changing the experimental conditions. Figure reprinted from the reference [96]

In **Chapter 5**, we developed a new method of AuNPs synthesis with different surface morphology and size applying ratio of Fe(II) salts as the main reduction agent. In addition, the SERS properties of the NPs obtained were carefully analyzed.

CHAPTER

2

SYNTHESIS OF GOLD FUNCTIONALIZED NANOPARTICLES WITH THE *ERANTHIS HYEMALIS* LECTIN AND PRELIMINARY TOXICOLOGICAL STUDIES ON *CAENORHABDITIS ELEGANS*

Contribution: In this chapter, the candidate has realized the synthesis, functionalization and the characterization of gold nanoparticles and gold nanoparticles functionalized with the Lectin protein.

Published in: Djafari, J.; McConnell, M.T.; Santos, H.M.; Capelo, J.L.; Bertolo, E.; Harvey, S.C.; Lodeiro, C.; Fernández-Lodeiro, J. Synthesis of Gold Functionalised Nanoparticles with *Eranthis Hyemalis* Lectin (EHL) and toxicological studies on *Caenorhabditis Elegans*, *Materials* (2018), **11**(8), 1363. **DOI: 10.3390/ma11081363**

Presented in: Marie T. McConnell, Jamila Djafari, Javier Fernández Lodeiro, Jose Luis Capelo, Carlos Lodeiro, Emilia Bertolo, Simon C. Harvey. P10. Toxicity effects of *Eranthis Hyemalis* Lectin (EHL) functionalised Gold Nanoparticles in *C. elegans*. 2nd International Caparica Christmas Conferences on Translational Chemistry, 2nd IC3TC in Aldeia dos Capuchos, Caparica, Portugal, 4th-7th December 2017.

2.1. INTRODUCTION

Lectins are a class of proteins ubiquitously expressed in plants, animals, bacteria, and viruses. They are well known for their ability to agglutinate erythrocytes, and their ability to bind carbohydrates selectively based on the individual sugar specificity of the lectin.[98,99] Plant lectins play a key role in plants' defences;[100,101] insecticidal, antifungal, and antiviral qualities have also been widely described.[102–105] *Eranthis hyemalis* (Winter Aconite) is a late winter/early spring flowering perennial plant of the family *Ranunculaceae*. *E. hyemalis* possesses a proteinaceous toxin (named *Eranthis hyemalis* lectin, EHL), found to cause agglutination of erythrocytes as well as impacting on the fitness of some agricultural pests and plant viruses.[102–106] To date, *E. hyemalis* is the sole representative of the *Ranunculaceae* to be reported to express lectin activity. Due to the structural and toxicity studies conducted,[102,106–108] EHL should be classed as a Type II Ribosome Inactivating Protein (RIP). RIPs are a class of enzymes (EC 3.2.2.22) with a mode of action which results in the breakage of a glycosidic bond in the 28s rRNA in the 60S subunit of the ribosome, resulting in the disruption of protein synthesis and subsequent cell death. EHL shows specificity for N-acetyl-galactosamine,[102,106] an overexpressed and incompletely glycosylated sugar in the Tn antigen which characterizes cancer linked O-glycans.[109] Other N-acetyl-galactosamine specific RIPs such as the Mistletoe lectin and Riproximin have demonstrated promising therapeutic relevance as anticancer agents.[110–112] EHL could therefore have a promising future as an anticancer agent, if its toxicity can be harnessed and tuned to appropriate levels.

Previous work by some of the authors has shown biocidal effects of EHL against the free-living nematode *Caenorhabditis elegans*.[113] *C. elegans* is a well-established model organism for initial toxicological studies due to the conserved nature of its biological and biochemical processes, including the stress response and disease pathways.[114] A wide range of available mutants, a short life cycle, a well-documented life history, and a largely transparent body (which makes it possible to observe unusual effects easily), are some of the advantages of *C. elegans*.[115] Developing *C. elegans* individuals pass through a well-defined set of life stages, with individuals hatching as first larval stage (L1) worms. These L1 worms subsequently molt through three further larval stages—the L2, L3, and L4 stages—before maturing as adults. Development is temperature dependent and takes approximately 3 days at 20 °C. Newly hatched L1 worms measure around 0.25 mm in length, and in their adult stage they reach up to 1 mm. An interesting characteristic of *C. elegans* is its ability to enter an alternate L3 life cycle stage known as the *Dauer* larvae. Naturally induced *dauer* larval arrest occurs when L1 and L2 larva are exposed to environments not suited for growth and reproduction.[116] These environments are characterized by a depleted food source and population overcrowding, with the chemosensory cues and signals for these detected by the L1 larvae. As part of development into *dauer* larvae, worms develop a

specialized outer cuticle, and seal their mouths, preventing feeding. In combination with changes in their metabolism, these adaptations mean that *dauer larvae* have an increased lifespan, an enhanced resistance to environmental stress and are resistant to many chemical treatments that would kill other lifecycle stages. This resulting *dauer larvae* is in an arrested developmental state (a temporary halt in its development), and can survive for months until conditions improve, at which point development resumes with *dauer larvae* moulting in to L4s.[116]

Colloidal gold nanoparticles (AuNPs) have long been exploited in science for their optical properties. The applications of AuNPs have increased enormously in recent years and are used routinely in both material science and within biomedical sciences as bioimaging agents, therapeutic agents, and drug delivery vehicles.[117–120] AuNPs can be functionalized with both therapeutic and imaging agents simultaneously, thus are a powerful tool in cellular studies.[121] AuNPs can be functionalized with ligands with high affinity and specificity for target cells such as the Tn antigen, which is where conjugating AuNPs with a RIP such as EHL presents an opportunity to fine tune EHL's biological effects.

Herein we present the synthesis and characterization of AuNPs conjugated with EHL (AuNPs@EHL), and the preliminary study of the effects of AuNPs@EHL on *C. elegans*. The aim was to establish the viability of the conjugate and to perform a set of initial assays to establish if the biological effect of EHL is altered by the conjugation. The conjugates were analyzed by UV-Vis spectroscopy, Dynamic Light Scattering (DLS), Zeta Potential analysis, and Transmission Electron Microscopy (TEM). Biological assays on the effect of AuNPs@EHL on *C. elegans* were performed using first life stage (L1) and pre-adult stage (L4) nematodes, and the results compared to previously published data on the effect of EHL on L1 nematodes.[113] Additionally, the effects of naked AuNPs on L1 and L4 nematodes, and the effect of EHL on L4s were also studied.

2.2. MATERIALS AND METHODS

2.2.1. Materials

Tetrachloroauric(III) acid ($HAuCl_4 \cdot 3H_2O$), Sodium hydroxide (NaOH), Hydrochloric acid (HCl), Sodium chloride (NaCl), and Sodium citrate tribasic ($C_6H_5Na_3O_7 \cdot 2H_2O$) were purchased from Sigma Aldrich (Germany), Strem Chemicals, Fluka or Panreac, and used without further purifications. Acetonitrile (ACN, 99.9% purity) and acetic acid glacial (99.7% purity) were purchased from Sigma-Aldrich (Germany). Ethanol (EtOH, 96% purity) was purchased in Panreac (Spain). Water was always Milli-Q grade by Millipore.

Protein quantification was accomplished by measuring the absorbance at 595 nm with the use of a Bradford Protein Assay using a CLARIOStar® High performance monochromator

multimode BMG Labtech, Germany from the PROTEOMASS-BIOSCOPE Facility lab. The transmission electron microscopy images were obtained using a JEOL JEM 1010F transmission electron microscope from the CACTI, University of Vigo, (Spain), operating at 100 kV. Samples were prepared dropping 5 µL of the colloidal suspension on a copper grid coated with a continuous carbon film, and the solvent was allowed to evaporate. TEM Images were characterized using ImageJ software (Image 1.51h, Wayne Rasband, National Institutes of Health, USA),[122] with a minimum of three hundred NPs measured. The size measurements were performed with the NPs diluted in 1 mL of water in a Zetasizer Nano ZS instrument (Malvern Instruments, Malvern, Panalytical, UK) in the PROTEOMASS facilities. Zeta potential quantification was carried out in the same Zetasizer Nano ZS instrument.

2.2.2. Synthesis of EHL Conjugated Gold Nanoparticles

Gold nanoparticles functionalized with citrate (AuNPs@Citrate) were prepared by modification of a previously published protocol.[123] An aqueous solution (125 mL) containing 49 mg of tetrachloroauric (III) acid ($HAuCl_4 \cdot 3H_2O$) was heated until boiling point without reflux to ensure a low temperature gradient in the walls of the flask; the solution was kept boiling for 10 min. Then, a pre-boiled aqueous solution (12.5 mL) containing 147 mg of sodium citrate tribasic ($C_6H_5Na_3O_7 \cdot 2H_2O$) was added rapidly. The reaction mixture was heated to boiling for an additional 15 min, and then allowed to cool to ~25°C and left with magnetic stirring overnight. The reaction was then diluted to a final volume of 140 mL with milliQ water and was transferred into a glass bottle for storage. The final obtained AuNPs@Citrate presented a concentration of 0.8 mM in terms of Au(0) and were used without purification.

To achieve the bioconjugation of the AuNPs@Citrate with EHL, the protein was suspended in Phosphate Buffer Saline (PBS) solution. Quantification via Bradford technique indicated an EHL concentration of 1090 ± 40 µg/mL. Six experiments were performed in order to characterize the optimal quantity of EHL to achieve the stabilization of the NPs: 25 µL, 50 µL, 100 µL, 200 µL, 300 µL, and 500 µL of EHL solution were used. On each case, the EHL solution was added onto 5 mL of AuNPs@Citrate ([Au(0)] = 0.8 mM) and left under vigorous stirring at room temperature for 2 h, to ensure effective functionalization. The NPs obtained—AuNPs@EHL-1 (25 µL), AuNPs@EHL-2 (50 µL), AuNPs@EHL-3 (100 µL), AuNPs@EHL-4 (200 µL), AuNPs@EHL-5 (300 µL), AuNPs@EHL-6 (500 µL) —were isolated by centrifugation at 14,000 rpm during 25 min, and then suspended in PBS solution. A second centrifugation cycle and resuspension in 5 mL of MilliQ water were performed. The first supernatant was filtered in a cellulose filter of 0.22 µm, and quantified by the Bradford technique, in order to determine EHL concentration at the NPs surface. AuNPs@EHL-3 (100 µL) was selected to perform the biological studies.

2.2.3. Nematode Assay

Worms were obtained from the *Caenorhabditis* Genetics Center and maintained using standard methods[124] on nematode growth media plates (NGM) using an *Escherichia coli* OP50 strain food source. *C. elegans* strain N2 was used for the assays. In all experiments, treatments and genotypes were blind coded, the position of plates within experimental blocks was randomized, and any contaminated plates displaying evidence of fungal growth were excluded from all analysis. Assays were initiated using arrested and synchronized *C. elegans* first stage larvae (L1s) obtained by allowing eggs, isolated from gravid hermaphrodites by hypochlorite treatment,[124] to hatch on NGM plates in the absence of food for 24 h at 20°C.

For the experiments on L1 stage worms, synchronized L1s were incubated in 15 mL eppendorf tubes at 20 °C in a solution of one of four treatments (see below) for 6 h. Three replicates of each treatment were made. After incubation, all treatments were subjected to a cycle of three washes with M9 buffer[124] with a 2 min centrifugal spin at 2000 g. Worms were then added to seeded (*Escherichia coli* OP50) NGM plates and incubated at 20 °C. Plates were then scored on day 3 for survival, arrested development, and for *dauer larvae* formation.

For the experiments on L4 stage worms, synchronized L1s were placed on seeded NGM plates and incubated at 20 °C until the L4 stage was reached. Treatment was then carried out in the same set of liquid conditions as experiment 1 for 18 h, with tubes placed in a shaking incubator at 20 °C overnight. As previously, worms were then washed three times and moved onto en masse onto NGM plates (one plate per tube). L4 stage worms were then individually picked from these plates onto seeded NGM plates, 50 per treatment. Worms were then transferred to new plates daily during the reproductive period, with progeny allowed to develop for 2 days before they were counted. Treatments were as follows: First, M9 liquid nutrient media and EHL@[1.51 mg/mL]; second, M9 liquid nutrient media and AuNPs@EHL-3; third, M9 liquid nutrient media and AuNPs@EHL; and fourth, M9 liquid nutrient media.

2.3. RESULTS AND DISCUSSION

2.3.1. Synthesis and Characterization of the Bioconjugated Gold Nanoparticles (AuNPs@EHL)

AuNPs@EHL were synthesized by attaching the protein to the NPs surface through adsorption. This methodology has been widely adopted to prepare many NPs/protein bioconjugates.[125–128] In our case, the bioconjugation was achieved by incubating the

AuNPs@Citrate in water solution, with an EHL solution in PBS. The particles were analyzed by UV-Vis spectroscopy (JASCO Co. Japan), DLS (MALVERN, Panalytical, UK), Zeta Potential (MALVERN, Panalytical, UK), and TEM (JEOL, JEM 1010 Japan) analysis. The ruby red colloidal solution of AuNPs@Citrate presents a Localized Surface Plasmon Resonance (LSPR) band at 519 nm in the UV-Vis spectrum (**Figure 2.1**). TEM analysis shows that the spherical AuNPs@Citrate have an average size 14.4 nm (SD = 1.3) (**Figure 2.1**). DLS experiments indicated that the AuNPs@Citrate measured 18.80 nm in Z-average, with a Zeta Potential equal to −43.6 mV/cm, confirming the NPs stabilization by citrate molecules. The concentration of the gold colloid obtained, in terms of Au(0), was calculated from the absorption at 400 nm.[129–131] For this wavelength, the absorption is mainly due to interband transitions in metallic gold.[130,132] We applied a 1:10 dilution to the colloidal solution to obtain the UV-Vis spectroscopic profile, obtaining an Abs_{400} = 0.19, corresponding to concentration of [Au(0)] = 0.08 mM. Therefore, the precursor colloid used for the protein conjugation presented a concentration of 0.8 mM. (**Figure 2.1**) Thus, we obtained a concentration of [Au (0)] = 0.8 mM.

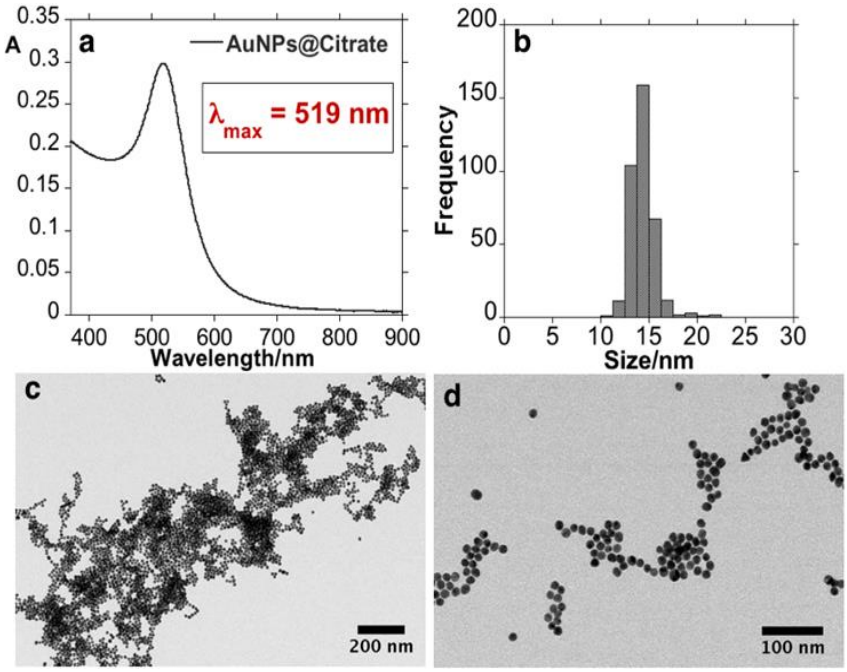

Figure 2.1. (a) UV-Vis spectrum, (b) histogram and (c,d) low magnification TEM images of AuNPs@Citrate. The histogram is derived from measurements of 300 nanoparticles made in ImageJ software.

An incubation process was performed to conjugate the AuNPs@Citrate with EHL; the concentration of the EHL solution used (determined by the Bradford technique) was 1090 ± 40 µg/mL. Six experiments were performed in order to characterize the optimal quantity of EHL to achieve the stabilization of the NPs. The following volumes of EHL solution were used: 25 µL (AuNPs@EHL-1), 50 µL (AuNPs@EHL-2), 100 µL (AuNPs@EHL-3), 200 µL (AuNPs@EHL-

4), 300 µL (AuNPs@EHL-5), and 500 µL (AuNPs@EHL-6). All the NPs obtained were characterized by UV-Vis spectroscopy, DLS, Zeta Potential, and TEM. Results are summarized in **Table 2.1** and **Figure 2.2**.

Table 2.1. AuNPs@EHL solution composition for each experiment, DLS, and Zeta Potential Values and protein amount on the nanoparticles.

AuNPs@EHL Sample	**1**	**2**	**3**	**4**	**5**	**6**
Volume of EHL added (µL)	25	50	100	200	300	500
VT of the reaction (µL)	5025	5050	5100	5200	5300	5500
Mass EHL in the reaction (µg)	27.3	54.5	109	218	327	545
Mass EHL in supernatant (µg/mL)	3.1±0.1	7.4±0.3	4.0±0.1	40±2	61.1±0.4	84 ±3
Mass EHL in VT supernatant (µg)	15.6±0.5	37.4±0.3	20.4±0.1	208.0±10	323.8±2	462.0±17
[EHL] in the NPs (µg)	11.7	17.1	88.6	10.0	3.2	83.0
Z-Average value (nm)	266.4	90.3	54.4	51.7	60.8	51.3
Polydispersity Index (PDI)	0.29	0.26	0.28	0.42	0.44	0.44
Zeta Potential (mV/cm)	−23.1	−19.8	−27.8	−24.6	−20.2	−29.4

[EHL] = concentration of EHL, VT = Volume Total.

To try to observe, using the DLS analysis, the possible excess of EHL in the Gold colloids, we first analyzed a suspension of EHL in water (25 µL of EHL solution in PBS (C = 1.09 mg / mL) dispersed in 5 mL of ultrapure water). To register the DLS measurement of EHL, we did not filter this solution and we defined the same parameters used in the colloids' analysis (Same parameters used to analyze the Au colloids) to keep constant the measurement conditions in all samples (EHL free and Gold colloids). As expected, by dispersing the EHL protein in water, the DLS obtained has two well-differentiated signals. The signal that appears to a smaller diameter is likely to originate from free EHL protein units in solution, while the larger one could be related to EHL aggregates in the aqueous solution. When comparing the data of the pure EHL protein with the functionalized colloids, it can be noted that the sample AuNPs@EHL-3 presents the best functionalization, not detecting excess protein for this case (**Figure 2.2**). Additionally, the analysis of the DLS in water or PBS for this sample offers a similar result in both media (**Figure 2.3**). Based on our analysis of UV-Vis, DLS and TEM, we feel that the sample AuNPs@EHL-3 presents a correct functionalization with EHL, without apparent excesses of protein not adsorbed on the surface of the NPs. In addition, during the purification of gold colloids by centrifugation, the remaining NPs present in the first supernatant in samples obtained for larger amounts of protein used (AuNPs@EHL-4 to AuNPs@EHL-6), making the protein quantification, using colorimetric techniques, can be strongly affected by the presence of this remnant of NPs in the

solution, producing data of doubtful quantification. Based on all these considerations, we selected the sample AuNPs@EHL-3 to complete the proposed biological studies, in order not to mask possible results that would be consequence of non-correctly adsorbed protein in the NPs.

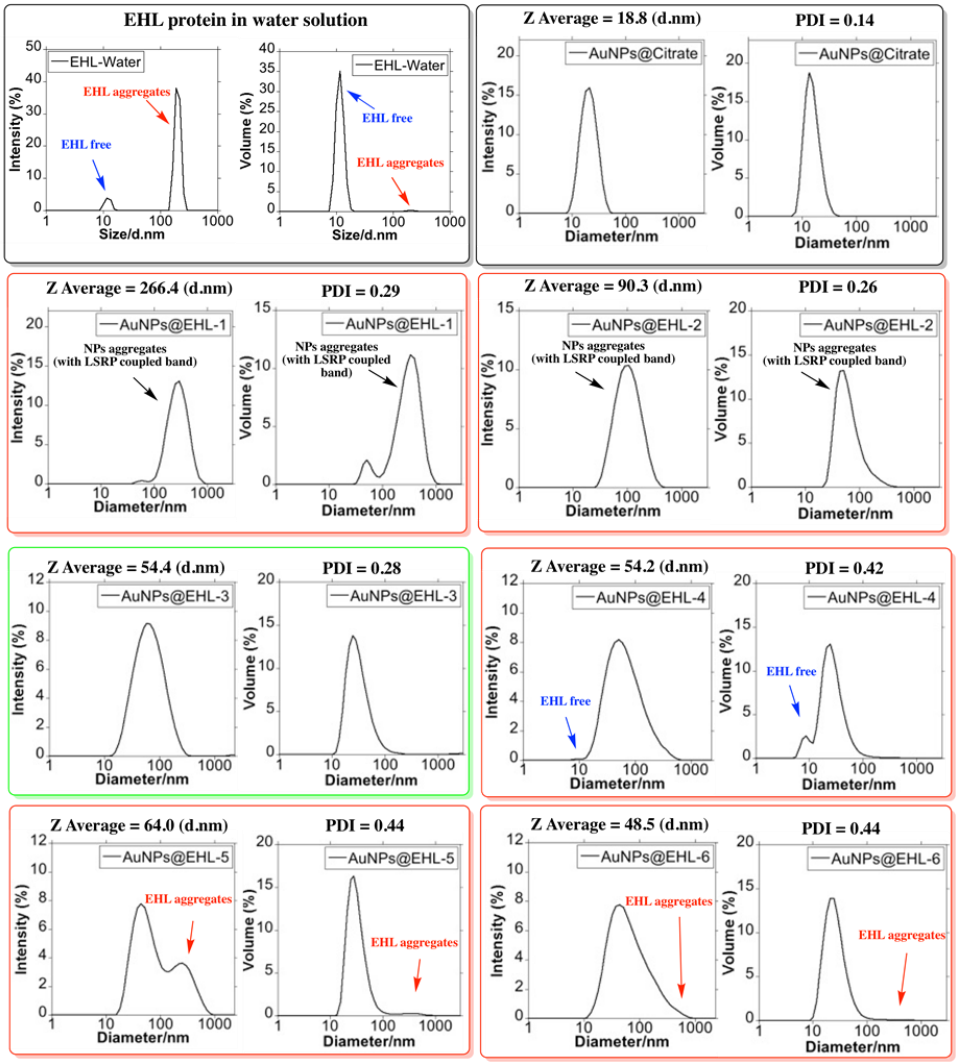

Figure 2.2. Size distribution measured by Dynamic Light Scattering. Distribution by %Intensity and %Volume of all AuNPs@EHL synthetized.

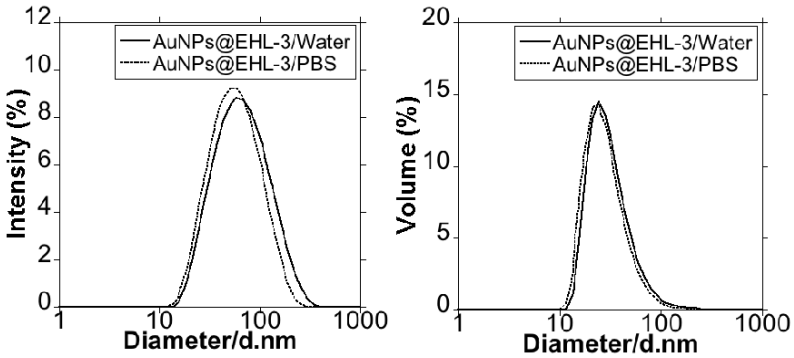

Figure 2.3. Size distribution measured by Dynamic Light Scattering of AuNPs@EHL-3 in water and PBS. Distribution by %Intensity and %Volume.

Addition of low quantities of EHL (AuNPs@EHL-1 and AuNPs@EHL-2) does not allow the stabilization of the colloidal system and induces NPs aggregation by partial functionalization. As it can be seen in **Figure 2.4**, a red shift on the LSPR band was observed. In addition, the aggregation of the NPs was confirmed by the increase in Z-average value obtained for this samples (**Figure 2.5 and Figure 2.3)**. TEM images also confirm that aggregation has occurred (**Figure 2.6a**). Due to its dimeric structure, EHL could act as a link between the NPs, and thus induce aggregation in the colloidal system. Moreover, due to the incomplete formation of the NPs' corona, in the presence of PBS salts it could modify the isotropy charge produced by the citrate adsorbed in the surface, resulting in the formation of nano-aggregates.

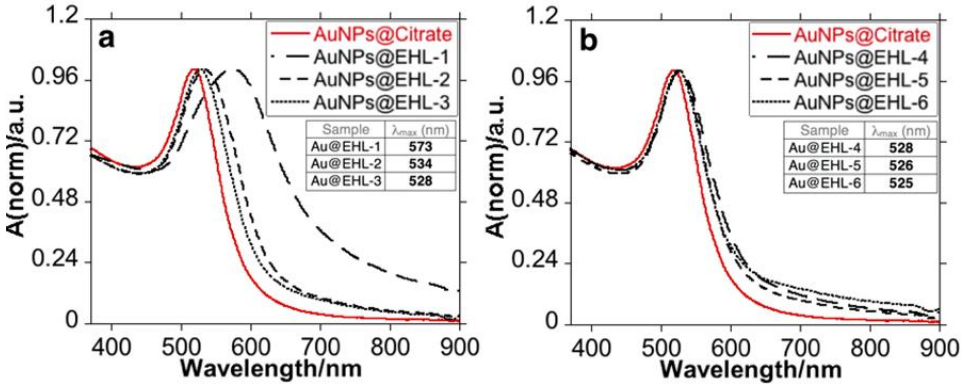

Figure 2.4. UV-Vis spectra of the different AuNPs@EHL samples synthesized: (a) AuNPs@Citrate, AuNPs@EHL-1, AuNPs@EHL-2, and AuNPs@EHL-3, and (b) AuNPs@Citrate, AuNPs@EHL-4, AuNPs@EHL-5, and AuNPs@EHL-6.

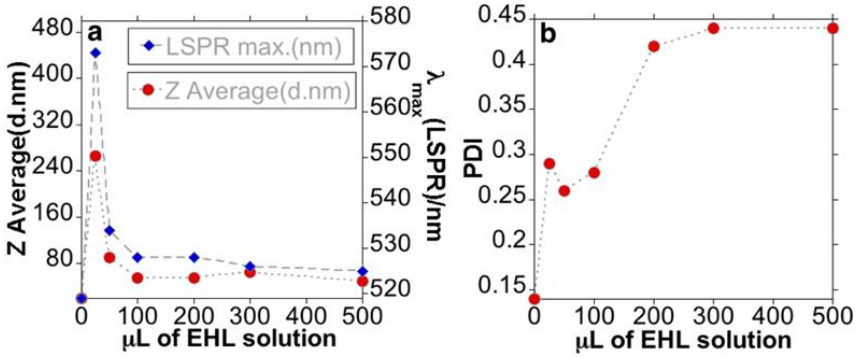

Figure 2.5. (a) Z-average (red dot) and LSPR (Localized Surface Plasmon Resonance) maximum (blue dot) and (b) PDI of the AuNPs@EHL obtained as a function of EHL amounts added.

For higher amounts of EHL (AuNPs@EHL-4, AuNPs@EHL-5, and AuNPs@EHL-6), saturation of the NPs surface occurs, as shown by the similar max of the LSRP band when compared with AuNPs@EHL-3, together with the similar Z average obtained (**Figure 2.5 and Figure 2.2**). Moreover, a significant increase in PDI (polydispersity index) was observed for AuNPs@EHL-4, AuNPs@EHL-5 and AuNPs@EHL-6 (**Figure 2.5 and Figure 2.2**). These

results suggest that the colloidal systems conjugated in these conditions were composed of AuNPs@EHL and an excess of EHL molecules. In our case, additional centrifugation cycles were not able to wash the unreacted EHL. To this respect, the decrease in the rotational speed in the time intervals studied (between 20 min and 1 h) resulted in a considerable increase in the concentration of AuNPs in the supernatant. (**Figure 2.3**).

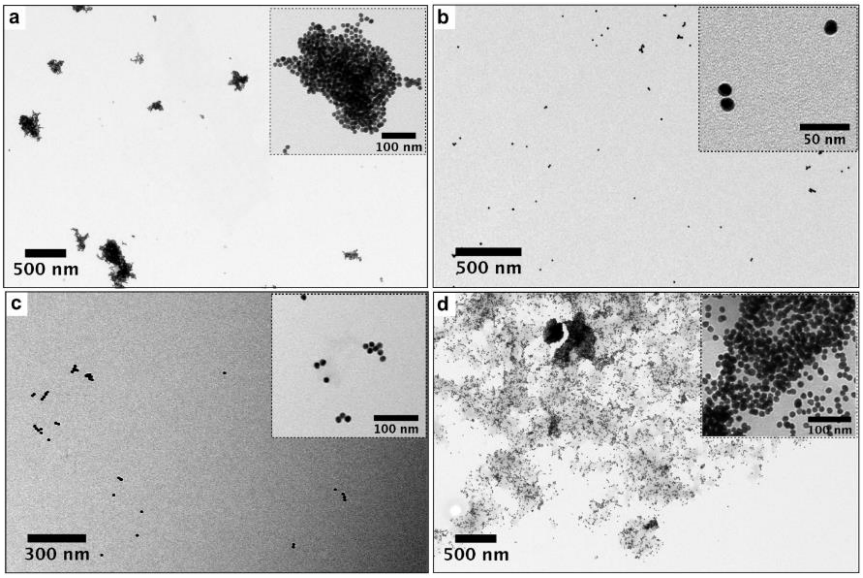

Figure 2.6. TEM images of AuNPs@EHL with different amounts of protein added: (a) AuNPs@EHL-2 (25 µL), (b) AuNPs@EHL-3 (100 µL), (c) AuNPs@EHL-4 (200 µL), and (d) AuNPs@EHL-6 (500 µL). In all cases, the nanoparticles go through two centrifugation cycles (14,000 rpm × 25 min) and are resuspended in MilliQ water.

In an attempt to quantify the amount of protein on the surface of NPs, we have analyzed the first supernatant obtained during the purification process of the NPs using the Bradford technique. For higher amounts of EHL (AuNPs@EHL-4, AuNPs@EHL-5, and AuNPs@EHL-6), this supernatant was not completely clear and still contained NPs, even after filtering, which can produce an erroneous reading using the Bradford technique. This is because in spectroscopic quantification the wavelength used may overlap with the LSPR band of the AuNPs, resulting in the appearance of increased protein values (**Table 2.1**).

The results obtained suggest that the best functionalization is achieved with the addition of 100 µL of protein (1090 ± 40 µg/mL) onto 5 mL of AuNPs@Citrate solution. The AuNPs@EHL obtained (sample AuNPs@EHL-3) show a high percentage of protein functionalized (17.7 g/mL); TEM images and DLS analysis confirm lack of aggregation and the stability of the resulting colloidal solution (**Figure 2.6b and Figure 2.2**). UV-Vis spectra show a redshift in the LSPR band from 519 nm to 528 nm (**Figure 2.5**) suggests a composition change on the surface of the NPs, indicative of the protein adsorption.[133] The Z-average increased from 18.8 nm (for AuNPs@Citrate) to 54.4 nm for AuNPs@EHL-3.

In order to show that the EHL is indeed conjugated to the surface of the NPs, a test was carried out by adding 200 µL of 2 M NaCl to a solution of 3 mL of the respective gold colloid (factor dilution 1:10); results are shown in **Figure 2.7**. When NaCl was added to the AuNPs@Citrate, the colloid aggregation occurred. This phenomenon can be visualized through the color change of the solution from red to blue accompanied by a marked red-shift in λmax of the LSRP band. Due to the presence of electrolytes such as sodium chloride, the negative charge of the colloids is masked causing an imbalance between the repulsive and attractive forces and producing colloid aggregation.[134] The addition of NaCl onto AuNPs@EHL-3 did not result in any destabilization of the system, showing that EHL molecules are on the NPs surface. Analysis by DLS of the sample AuNPs@EHL-3 in 100% PBS again confirms the presence of the EHL protein on the surface of the AuNPs (**Figure 2.3**).

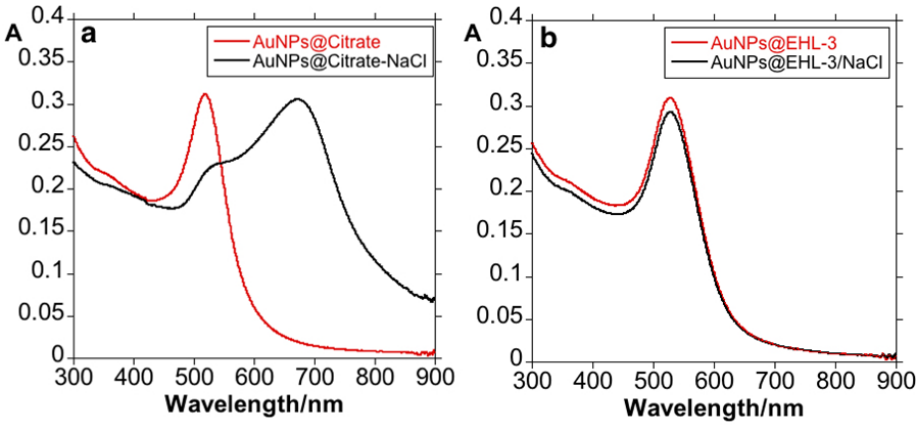

Figure 2.7. UV-Vis study of the effects of adding 200 µL NaCl 2M to 3 mL of (a) AuNPs@Citrate and (b) AuNPs@EHL-3. Dilution factor 1:10.

2.3.2. Biological Activity against *C. elegans*

C. elegans is a well-established model in toxicological research to investigate toxicological responses at a whole organism level.[135–137] The nematode has also been used specifically in relation to the toxicology of NPs.[138,139] The effect of AuNPs@EHL on *C. elegans* was investigated and compared to the effect of AuNPs@Citrate treatment and EHL treatment. The biological studies were performed using AuNPs@EHL-3 (which from now on will be referred to as AuNPs@EHL). Previous work by some of the authors has shown that EHL has biocidal properties against *C. elegans*, producing a significant reduction in fecundity, development and growth. Additionally, the authors reported a high incidence of abnormal *dauer* development when arrested L1 larvae were treated with EHL and then maintained on food, i.e., EHL treatment resulted in *dauer larvae* formation under conditions that produced 100% non-*dauer* development in non-treated worms. These EHL-induced *dauer larvae* were also unable to resume development when

maintained on food. The authors called this a "lectin-induced effect" and suggested that the occurrence of *dauer* formation and a failure to recover in the presence of food indicates that EHL is binding specifically to amphid neurons.[113]

Here, two sets of experiments were performed. The first set was a replication of the work on the effects of EHL on *C. elegans*,[113] using AuNPs@EHL. The second set of experiments (set 2) were carried out using L4 stage (pre-adult) worms and had not previously been conducted with EHL. An observation that the AuNPs@EHL sample did not agglutinate erythrocytes, a characteristic of the native protein, was recorded prior to commencement of the experiments. This effect suggests that conjugation changes important properties in the native protein.

For the first set of experiments L1 stage worms were treated with AuNPs@Citrate, AuNPs@EHL, and EHL, as well as a control group with no treatment. For the treated L1s, the expected *dauer larvae* and developmental arrest in response to EHL treatment was observed. However, there is no *dauer larvae* formation in response to AuNPs@Citrate or AuNPs@EHL, and none in the control. As previously reported, EHL also killed L1s in this assay, whilst the other treatments did not differ in L1 survival (**Table 2.2**). From these results, we conclude that AuNPs@Citrate do not obviously affect L1s, and that the AuNPs@EHL do not replicate the EHL effect. In conjunction with the empirical observation that agglutination properties were absent from the AuNPs@EHL sample, this would indicate that a conformational change has occurred potentially in the protein induced by conjugation to the NPs, which blocks the EHL neuronal binding effects.

Table 2.2. EHL treatment affects survival and development of treated C. elegans L1s. When scored, adult worms were only observed on 3 of the 12 EHL plates, with worms showing varied degrees of developmental delay.

Treatment	No. of Plates	L1s per Plate	Mean % Survival (min. and max.)	Mean % Dauer Formation (min. and max.)
Control	11	54.6 ± 3.8	68 (53–81)	0
EHL	12	64.2 ± 7.0	23 (11–40) *	24 (0–45) *
AuNPs@Citrate	11	58.6 ± 3.2	73 (54–84)	0
AuNPs@EHL	12	48.7 ± 6.6	68 (49–83)	0

** Denotes treatments where the proportion of surviving worms or dauer larvae differs from that observed in the Control ($p < 0.05$, by Mann-Whitney for the analysis of % survival and by Fisher's Exact Test with for the analysis of % dauer larvae formation, both with Bonferroni adjustment to correct for multiple testing).*

In the second set of experiments, using L4 stage worms, there was a small effect on lifetime fecundity in the EHL treated worms, and a delay in reproduction in both the EHL treated and the AuNPs@EHL worms; whilst naked NPs did not obviously affect the L4 stage worms. We can thus conclude and that AuNPs@EHL does have a biological activity. For the treated L4s, there was a difference between treatments in lifetime fecundity (TREATMENT: $F_{3,68} = 2.76$, $p =$

0.049) that is a consequence of a small reduction in lifetime fecundity in the EHL treated worms (EHL treatment significantly different to the control and nanoparticle-treated worms by Fisher's post-hoc testing) (**Figure 2.8a**). There is also variation between treatments in early reproduction ($H = 14.22$, $df = 3$, $p = 0.003$), with both the EHL treated and the EHL conjugated nanoparticle treated worms showing a reduced early fecundity ($p < 0.05$ in comparison to control worms via Mann-Whitney test) (**Figure 2.8b**).

The L4 assays conducted show that AuNPs@EHL do still retain some activity, suggesting that ingestion in the absence of glyconjugate binding (which is absent in the L1 assay) of the molecule may present a low level of toxicity. The observation that AuNPs@EHL do not agglutinate erythrocytes would suggest that this is a factor. Of course, the inverse hypothesis may also be worthy of investigation, that the toxic A-chain activity may have been altered and that binding still occurs without the cytotoxic effects seen in the intact molecule. As non-RIP lectins have been shown to bind to epithelial cells in the gut causing reduced fitness,[140] this requires further study to establish the exact reason for the reduction in toxicity.

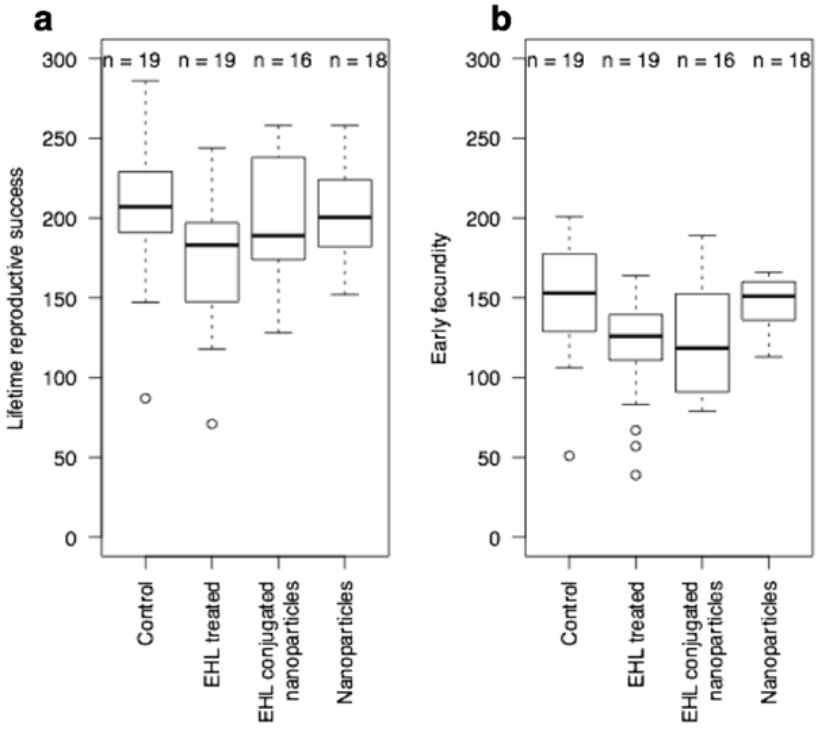

Figure 2.8. EHL conjugated nanoparticles (AuNPs@EHL) affect early reproduction (early fecundity), but not total reproduction (lifetime reproductive success) of *C. elegans* L4 stage.

2.4. CONCLUSIONS

The synthesis and characterization of gold nanoparticles conjugated with EHL (AuNPs@EHL) was successfully carried out; optimal functionalization was achieved with the addition of 100 µL of EHL (concentration 1090 ± 40 µg/mL) on 5 mL of AuNPs@Citrate ([Au(0)] = 0.8 mM). Biological assays on the effect of AuNPs@EHL on *C. elegans* were performed, using first life stage (L1) and pre-adult stage (L4) nematodes, and compared to the effect of naked AuNPs and EHL alone. This work shows that the activity of EHL is altered by conjugation and as such resulted in a lessened biological effect towards L1 stage worms. For the assays performed with L4 nematodes, naked NPs do not produce any obvious effect on the worms, while AuNPs@EHL conjugated NPs do produce a similar biological activity to that produced by EHL alone. This indicates that the biological effects of EHL can be separated. Extension of this work to cell lines would therefore be of interest, particularly to determine the mechanism by which the non-toxic effects on L4 worms are produced.

CHAPTER

3

NEW SYNTHESIS OF GOLD AND SILVER-BASED NANO-TETRACYCLINE COMPOSITES

Contribution: In this chapter, the candidate has realized the synthesis and functionalization as well as the characterization of all silver and gold nanoparticles, as well as all the spectroscopy titrations to evaluate the sensorial studies in solution.

Published in: Djafari, J.; Marinho, C.; Santos, T.; Igrejas, G.; Torres, C.; Poeta, P.; Capelo, J.L.; Lodeiro, C.; Fernández-Lodeiro. J, New Synthesis of Gold and Silver Based Nano-Tetracycline Composites. *Chemistry Open* (2016), **5**, 206-212.
DOI: 10.1002/open.201600016,
Invited Cover Picture **DOI: 10.1002/open.201600056**
Cover Profile **DOI: 10.1002/open.201600055**

Presented in: **(1)** Jamila Djafari, Javier Fernandez Lodeiro, Adrian Fdez Lodeiro, Elisabete Oliveira, Hugo M. Santos, Eduardo Araujo, Susana Jorge, Jose Luis Capelo, Carlos Lodeiro, "New Silver and Gold nano-antibiotic system for environmental applications: Detection of Al(III) in water. Shotgun SG13 (P52) (J. Djafari). II International Symposium on Nanoparticles, Nanomaterials and Applications, 2nd ISN^{2}A-2016, Caparica, Aldeia dos Capuchos, Portugal, 18th-21th January 2016.

(2) Jamila Djafari, Javier Fernandez Lodeiro, Adrian Fernandez Lodeiro, Elisabete Oliveira, Hugo M Santos, Susana Jorge, Eduardo Araujo, Jose Luis Capelo, Carlos Lodeiro, P18, Using the fluorescente tetracycline molecule in a one pot synthesis of gold nanoparticles: Enviromental applications in water. 2nd International Caparica Conference on Chromogenic and Emissive Materials, 2nd IC3EM 2016, Caparica, Aldeia dos Capuchos, Portugal, 5th-8th September 2016.

3.1. INTRODUCTION

Silver and gold NPs have emerged in recent decades as useful chemical tools due to their broad applications in medicine,[119,141] in (micro)biology,[71,142] as chemical sensors[143,144] or as catalysts[77,145] among others. The properties of Au or Ag colloidal systems are a combination of the Au and Ag own properties and the properties created by the molecular system used to decorate them when the nanomaterial is made. Ag and Au metal NPs present extraordinary size-dependent optoelectronic properties derived from the collective oscillation of conduction electrons produced by visible light. This phenomenon is known as surface plasmon resonance (SPR). The SPR is tunable, thus the frequency can be modified by changes in nanoparticle composition, size, shape or spatial disposition.[146]

In addition, metal NPs are sensitive to their local environment. The aforementioned phenomena have opened new possibilities for using such NPs as new chemo-nano-sensors.[26] Further important intrinsic characteristic of this type of nanomaterial are its oxidative properties, its chemical affinity and its chemical reactivity. Moreover, nanoscale dimension allows implementation in biological and biomedical applications.[147] In addition, the properties of these nanomaterials can be modulated by specific functionalization.[148]

Reports about functionalization of pre-synthesized AgNPs with tetracycline have been recently described[149,150] and Shen and co-workers have reported the tetracycline ability to reduce gold under specific conditions.[151] To the best to our knowledge, the simultaneous synthesis of AgNPS using tetracycline as a co-reducer and stabilizer agent has not been reported previously. Thus and following our research line in functionalized nanomaterials,[76,152–155] we report for the first time in literature the synthesis of gold and silver-based Nano-Tetracycline composites.

3.2. MATERIALS AND METHODS

3.2.1. Chemicals Materials

Silver Nitrate ($AgNO_3$), Tetrachloroauric(III) acid ($HAuCl_4.3H_2O$), Tetracycline, Sodium hydroxide (NaOH), Hydrochloric acid (HCl), Sodium chloride (NaCl), Potassium chloride (KCl), Mercury(I) chloride (HgCl), Magnesium(II) trifluoromethanesulfonate ($Mg(OTf)_2$), Calcium trifluoromethanesulfonate ($Ca(OTf)_2$), Manganese(II) nitrate tetrahydrate ($Mn(NO_3)_2.4H_2O$), Copper(II) nitrate hexahydrate ($Cu(NO_3)_2.6H_2O$), Zinc chloride ($ZnCl_2$), Cadmiun(II) trifluoromethanesulfonate ($Cd(OTf)_2$), Mercury(II) chloride ($HgCl_2$), Lead(II) trifluoromethanesulfonate ($Pb(OTf)_2$), Chromium(III) nitrate hexahydrate ($Cr(NO_3)_2.6H_2O$),

Iron(III) chloride hexahydrate ($FeCl_3.6H_2O$), Aluminium nitrate hexahydrate ($Al(NO_3)_2.6H_2O$), Gallium(III) nitrate hexahydrate ($Ga(NO_3)_2.6H_2O$), Indium(III) perchlorate octahydrate ($In(ClO_4)_3.8H_2O$), Ethylenediaminetetraacetic acid (EDTA), have been purchased from Sigma Aldrich, Strem Chemicals, Fluka or Panreac, and used without further purifications. Water was always Milli-Q grade by Millipore. The pH of aqueous solutions was performed using concentrated solutions of NaOH and HCl. The pH was measured by potentiometry.

3.2.2. Preparation of AgNPs@TC

In a two-necked round bottom flask, a solution of silver nitrate (4×10^{-4} M) in 50 mL Milli-Q water was heated up to boiling. Then, a pre-heated (80 °C) mixture of 20 mL of tetracycline (6×10^{-3} M – 6 eq) and NaOH (2.4×10^{-2} M – 24 eq) was added into the solution. The firstly yellow solution turns dark red after the addition of the alkaline solution due to the silver reduction. Then slightly becomes dark brown. The solution was refluxed during 2 h. The round bottom flask was then cooled in an ice/water bath. The NPs were separated from the supernatant by centrifugation twice at 8,000 rpm for 1 h. The pellet was washed one time with Milli-Q water 8,000 rpm for 30 minutes. The final yellow NPs were re-suspended in 15 mL Milli-Q water.

3.2.3. Preparation of AgNPs@TC-2

In a two-necked round bottom flask, a light protected solution of silver nitrate (4×10^{-4} M) in 50 mL Milli-Q water was heated up to boiling. Then, a boiled mixture of 20 mL of tetracycline (6×10^{-3} M – 6 eq) and NaOH (2.4×10^{-2} M – 24 eq) was added into the solution. The firstly yellow solution becomes dark red after the addition of the alkaline solution due to the silver reduction. Then slightly becomes red brown. The solution was refluxed during 15 min under darkness. The round bottom flask was then cooled in an ice/water bath. The NPs were separated from the supernatant by centrifugation twice at 8,000 rpm for 1 h. The pellet was washed one time with Milli-Q water 8,000 rpm for 30 minutes. The final orange NPs were re-suspended in 15 mL Milli-Q water.

3.2.4. Preparation of AuNPs@TC

In a two-necked round bottom flask, a solution of tetrachloroauric(III) acid (4×10^{-4} M) in 50 mL Milli-Q water was heated up to boiling. Then, a boiled mixture of 20 mL of tetracycline (6×10^{-3} M – 6 eq) and NaOH (2.4×10^{-2} M – 24 eq) was added into the solution. The firstly yellow solution becomes dark red after the addition of the alkaline solution due to the gold complex

formation. Then slightly becomes dark brown. The solution was refluxed during 2 h. The round bottom flask was then cooled in an ice/water bath. The NPs were separated from the supernatant by centrifugation twice at 10,000 rpm for 1 h. The pellet was washed one time with Milli-Q water 10,000 rpm for 30 minutes. The final red-pink NPs were re-suspended in 15 mL Milli-Q water.

3.2.5. Spectrophotometric Measurements

Electronic absorption spectra of NPs were recorded using a spectrophotometer Jasco V-630 and Jasco V-650 UV-Vis (Easton, MD, UK from the PROTEOMASS-BIOSCOPE Facility lab.). In both cases, the spectrophotometric characterization and titrations were performed by preparing stock solutions in milli-Q water in 10 mL volumetric flasks. The studied solutions were prepared by appropriate dilution of the stock solutions. In all cases, 1 cm optical path quartz cells were used (Hellma QXX).

To determine the coordinative characteristics of the functionalized NPs and sensorial effects, the absorption spectra in the absence and in the presence of a known concentration of different metal ions (Na^{+}, K^{+}, Hg^{+}, Mg^{2+}, Ca^{2+}, Mn^{2+}, Cu^{2+}, Zn^{2+}, Cd^{2+}, Hg^{2+}, Pb^{2+}, Cr^{3+}, Fe^{3+}, Al^{3+}, Ga^{3+}, In^{3+}) were recorded. The spectra were recorded with the increased addition of metal ion. All measurements were performed at controlled 298 K.

3.2.6. Dynamic Light scattering and Z-Potential measurement

Zeta Potential of samples was measured using Malvern Zetasizer Nano series (Worcestershire, WR14 1XZ, UK) from PROTEOMASS Scientific Society -BIOSCOPE Facility Lab. The measured solution was obtained by centrifugation 10 minutes at 8,000 rpm, and the pellet obtained was re-suspended in the previously prepared pH solution. Samples were analysed using a folded capillary cell at room temperature.

3.2.7. TEM Measurements

The transmission electron microscopy (TEM) images were obtained using a JEOL JEM 1010F transmission electron microscope from the CACTI, University of Vigo, (Spain), operating at 100 kV. Samples were prepared dropping 5 μL of the colloidal suspension on a copper grid coated with a continuous carbon film, and the solvent was allowed to evaporate. TEM Images were characterized using Image J program. Histograms were prepared counting a minimal of one hundred NPs per sample.

3.2.8. Metals screening – CLARIOstar

The screening of metals ions was performed using a CLARIOstar system, BMG Labtech (220-900 nm) in water from the PROTEOMASS Scientific Society-BIOSCOPE Facility Lab. The studies were carried out by preparing aqueous solutions of metals with concentrations between 1.10^{-3} M and 1.10^{-4} M. Concentrations of NPs were normalized to have an absorbance equal to 0.2. Using the 96-well-plate CLARIOstar system, the NPs were added to wells with the required amount of metals from 500 nM.

3.2.9. NPs Concentration and Inductively Coupled Plasma-Atomic Emission Spectrometer determination

The Silver concentration in the AgNPs@TC samples was determined by an ICP analysis using an Horiba Jobin-Yvon, France, model Ultima, equipped with an RF of 40,68 MHz, monochromator of Czerny-Turner with 1,00 m (sequential), automatic autosampler AS500. An CMA (Concomitant Metals Analysis) for the determination of simultaneous presence of Hg, As, Se, Sb and Sn was perform in the Analytical Laboratory REQUIMTE-FCT-UNL. Total NPs concentration (NPs + Tetracycline) was calculated by drying in a lyophilized solution of a 1mL of NPs in an eppendorf. The solid obtained was strict weighed with a microbalance. In this experiment a microbalance Mettler Toledo, Model AT21 comparator was used.

3.2.10. Bacteria and growth conditions

Bacterial strains considered in this study are described on **Table 3.1**. Strains tested were *E. coli* ST648 and *S. aureus* ST398, both resistant to tetracycline, and the control strains *E. coli* K12 and *S. aureus* ATCC 25923, susceptible to tetracycline. Bacteria were seeded on BHI medium agar (Oxoid) and incubated at 35 °C ± 2 °C for 18-20 h.

Table 3.1. Bacterial strains used in this study.

Strain	Relevant phenotype[a]	Reference
Escherichia coli K12 ATCC® 29425™	Non-pathogenic, Gram negative; Tet^s	ATCC®
Escherichia coli ST648	Pathogenic, Gram negative; Tet^r	[156]
Staphylococcus aureus ATCC® 25923™	Gram positive; Tet^s	ATCC®
Staphylococcus aureus ST398	Pathogenic, Gram positive; Tet^r	[157]

a: Tet^s = tetracycline sensitive; Tet^r = resistant to tetracycline.

3.2.11. Preparation of antibiotic and nanoparticles stock solutions

AuNPs@TC solution was diluted on a 60.9, 45.7, 32 - 0.125 μg/mL range and tested on all bacteria. AgNPs@TC (Sample 1) solution was diluted on a 35.5, 26.6, 25, 20, 16 - 0.25 μg/mL range and tested on all bacteria. AgNPsTC-2 (Sample 2) solution was diluted on a 62.3, 46.7, 40, 32 - 0.25 μg/mL range and tested on all bacteria. Tetracycline was tested on a range of 256 – 0.25 μg/mL for *E. coli*, and 1024-0.5 μg/mL for *S. aureus*. Positive (inoculated medium) and negative controls (medium supplemented with NPs/antibiotic) were included on all tests. All tests were performed on triplicate.

3.2.12. Determination of the minimal inhibitory concentration (MIC) of the nanoparticles

Minimum inhibitory concentration (MIC) assay was determined by broth-microdilution method, in order to determine functionalized NPs' antimicrobial effect on *S. aureus* and *E. coli*.[158] A total of three 96-well sterile microliter trays were filled with 100 μL of Luria-Bertani (LB) broth medium (Sigma-Adrich) and appropriate antibiotic dilutions.

Each set were inoculated aseptically with 10 μL of respective bacterial suspension (106 CFU/mL). An antibiotic-free control row was considered in each plate. The pH measuring was determined for first dilution well in each row, after inoculation. Plates were sealed with parafilm and incubated with shaking, at 35°C ± 2 °C for 18-20 h with aeration. Each experiment was performed in duplicate. MICs were recorded by the naked eye determining the lowest concentration that locked bacteria growth.

The effect of NPs on individual bacterial isolates was determined according to the following protocol. Eighteen-hour cultures of bacterial strains resulted from MIC testing were directly inoculated into fresh LB medium on 60 mm x 15 mm plates (100 μL total per sample). Control cultures without NPs were included in all experiments. The number of colony-forming unit (CFU) recovered after incubation for 18-20 h at 35°C ± 2°C with aeration was determined by plate counting. The number of bacteria present in the inoculum was determined for each strain, for each experiment. The colonies present on LB plates for each dilution per sample were counted and the presence/absence was registered.

The MBC is the lowest concentration of NPs that resulted in no bacterial growth after 18 h of incubation at 37 °C. Each experiment was performed in duplicate.

3.3. RESULTS AND DISCUSSION

3.3.1. Synthesis of AgNPs@TC and AuNPs@TC

Nishimura et al. have reported that the pH of the medium can control the reduction of silver ions in the presence of complexing molecules.[159] Using this strategy, we have synthetized AgNPs using tetracycline in basic pH under temperature stimulation. These nano-composites can be stabilized and functionalized with tetracycline through weak bonds in a simple step. Tetracycline is a complex molecule with different tautomeric forms, which makes difficult to determine the structure on the surface of the NPs. However, we assume that tetracycline can interact with silver ions via-amide position due to the affinity observed between silver ions and the amide group.[160] Tetracycline presents four acidic hydrogens, which can be deprotonate in water, Ha, Hb, Hc, and Hd, with their pka values of 3.3, 7.3, 9.0, and 11.8 respectively (**Figure 3.1**).[161]

The protonated species of tetracycline shows very low solubility in water solution. Using sodium hydroxide as a strong base, it is possible to deprotonate the molecule, reducing the silver ions present in solution at the same time (**Figure 3.2**).

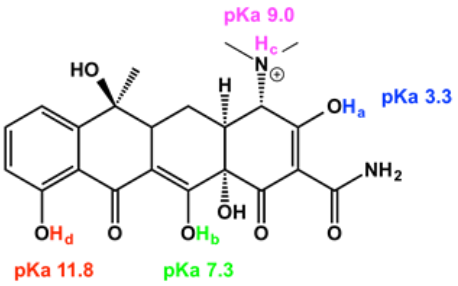

Figure 3.1. Structure of Tetracycline and its deprotonation sites with corresponding pka values.

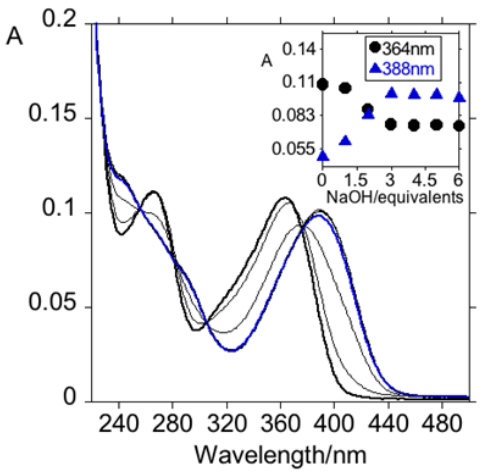

Figure 3.2 UV-Vis absorption spectra of titration of tetracycline with aqueous solution of NaOH. ([Tetracycline]=1.10^{-5}M in DMSO)

Figure 3.2 depicts a NaOH-based UV-Vis titration of tetracycline in DMSO (1.10^{-5} M). The presence of four isosbestic points at ca. 265, 282, 305 and 376 nm confirms the presence of different deprotonated species in water. The system is fully stabilized with the addition of three equivalents of NaOH. In order to ensure the effective deprotonation of the tetracycline, four equivalents of NaOH were used in our experiments. We have observed that the optimal molar ratio of $AgNO_3$/Tetracycline/NaOH for the synthesis of these NPs was 1/6/24.

The reaction was carried out at boiling temperature in order to promote the nitrate silver reduction. Over the boiled silver solution, was rapidly added the pre-heated (80 ºC) basic tetracycline solution. A rapid addition of the pre-heated solution should create lower temperature gradient, shortening the nucleation process. This reaction solution shows a yellow/brown color. After two centrifugation cycles, the AgNPs@TC colloidal system presents the silver colloids´ characteristic yellow color. The AgNPs@TC composites presents an intense SPR band centred at ca. 403 nm. Using transmission electron microscopy, a quasi-spherical shape with average size of 15 ± 5 nm was observed. (**Figure 3.3**).

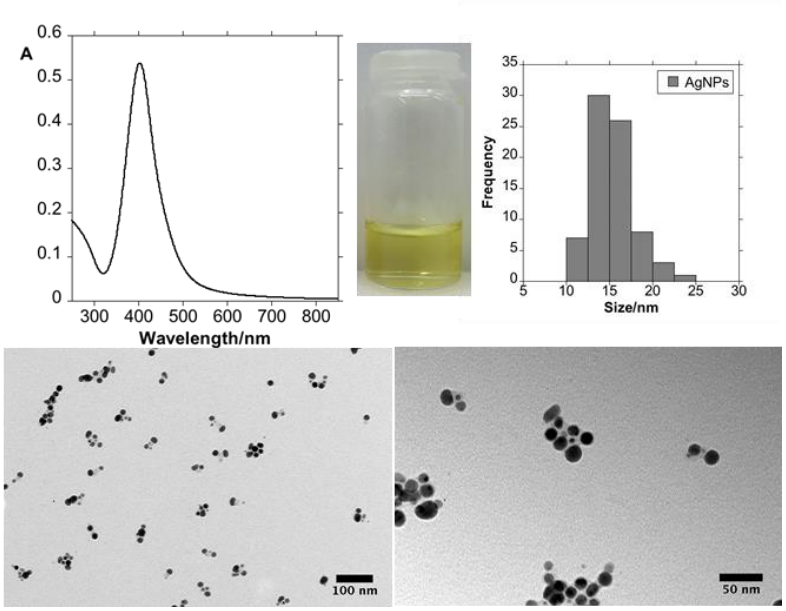

Figure 3.3. UV-Vis absorption spectra, color solution, histogram and TEM images of AgNPs@TC

The yellow colloidal water solution was stable for several weeks. The properties of this colloidal solution are pH dependent. Indeed, according to our UV-Vis studies, intense SPR band is observed at c.a. 403 nm at pH 5.5. For a pH value lower than 4 is observed a decrease of the SPR centered c.a. 403 nm, while forming a new SPR band centered at ca. 474 nm. This colloidal solution changes from yellow to orange (**Figure 3.4**). This phenomenon is due to a plasmonic coupling of discrete units of NPs. This coupling takes place as a result of the protonation of the pH-dependent sites present on tetracycline that leads to a decrease in the formal charge of the

NPs´ surface. This observation is consistent with the protonation values of tetracycline obtained in the literature.

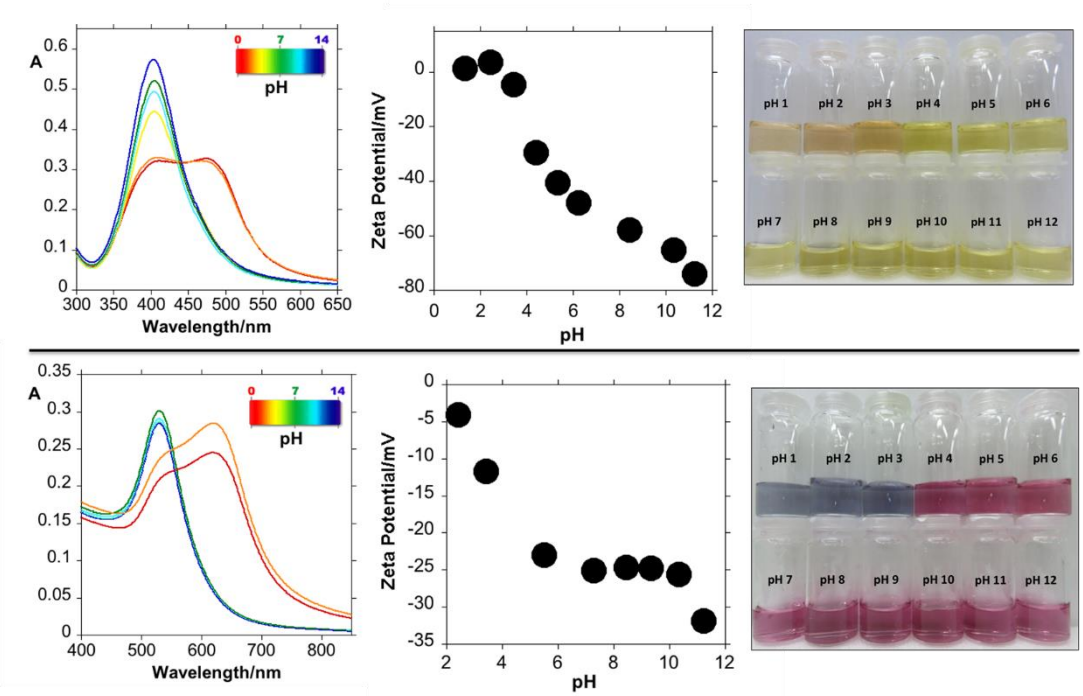

Figure 3.4. UV-Vis absorption spectra, Z potential and color solution of (Up) AgNPs@TC and (Down) AuNPs@TC as a function of pH (pH between 1 and 12).

A study of the Z-potential versus pH was done in order to confirm the above hypothesis. Between pH 4 and 12, the AgNPs@TC composites shows a negative surface charge ranging between -32 and -28 mV. This further confirms the stabilization of the colloidal system by the negative charges located on the tetracycline. However, at acidic values, between pH 2 and 4, the zeta potential was close to zero, and thus there are no charges stabilizing the particles. This fact increases particle aggregation. This aggregation is naked eye observed with the color change from yellow to orange as mentioned above. These findings are in agreement with the pKa values of the tetracycline, in fact, at pH lower than 3.3, tetracycline should be fully protonated. (**Figure 3.4**) In order to compare the antibacterial activity of AgNPs@TC composites, AuNPs@TC were synthesized following the same protocol. This Au-based nano-composites was synthetized to control whether the antibacterial activity of the Ag-based nano-composites was influenced by free silver ions.[65] It is well known, that gold is biocompatible, thus exhibiting low antibacterial activity.[162] The functionalized AuNPs@TC, presents an SPR band centred at ca. 530 nm confirmed by their pink-red color. This result is in agreement with the average size of these AuNPs, 25 ± 10 nm (**Figure 3.5**). As it was observed previously with the AgNPs@TC, the AuNPs@TC properties are pH-dependent in water (**Figure 3.4**). Tetracycline shows different stability depending on reaction time and temperature used. As was reported in the literature,

tetracycline has stronger sensitivity to moderate temperature for long periods than to higher temperature in short periods of time. Eisenhart et al. have previously reported that 90% of the tetracycline ligand is stable for 1 h at 90 ºC.[163,164] Tetracycline is also sensitive to light radiation.[165] Taking this information in mind, a second batch of AgNPs@TC-2 was done. Now the reaction time was settled in 15 minutes and in the dark. We have observed a decrease in the yield of nanomaterial obtained in such conditions. The spectroscopic profile shows a SPR band centred at ca. 400 nm with a shoulder at higher wavenumber. Electron microscopy images showed a greater degree of monodispersity when compared to AgNPs@TC. (**Figure 3.6**).

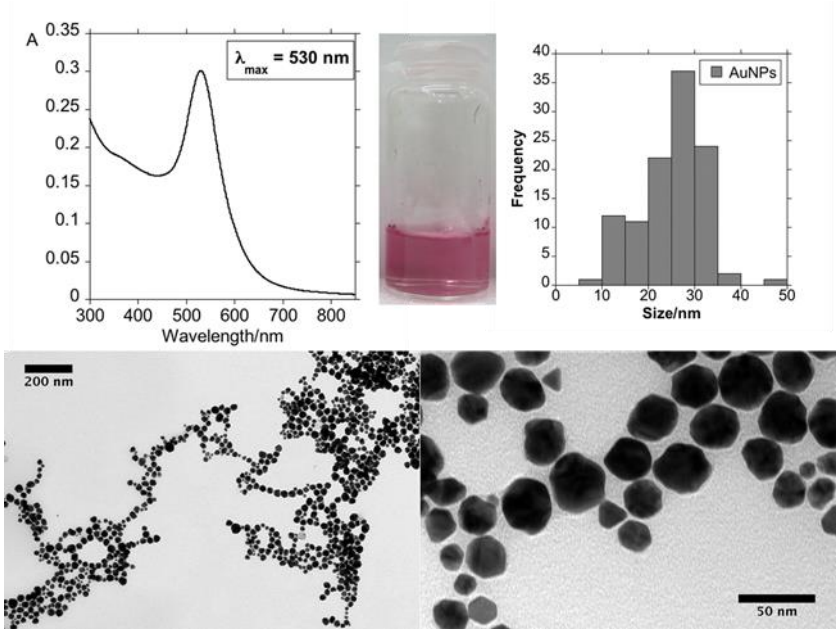

Figure 3.5. UV-Vis absorption spectra, color solution, histogram and TEM images of AuNPs@TC.

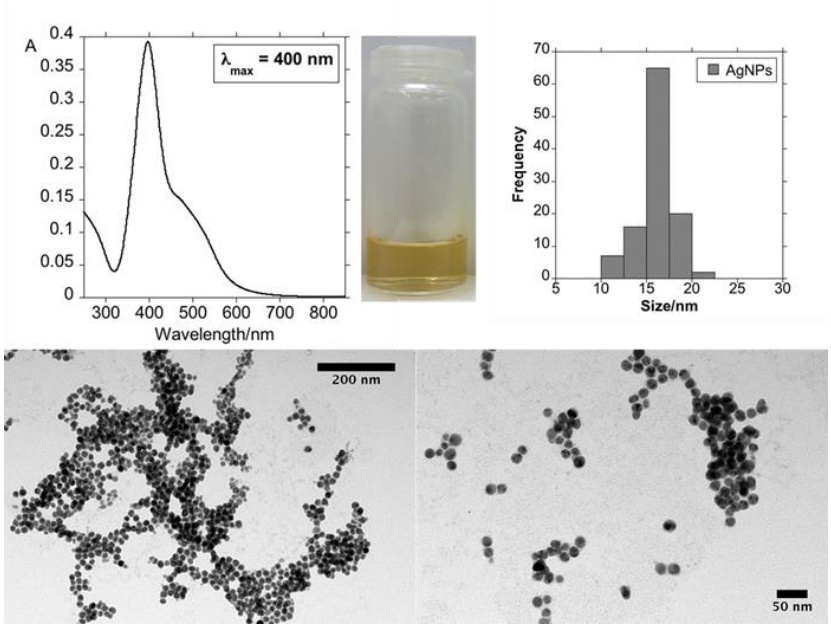

Figure 3.6. UV-Vis absorption spectra, color solution, histogram and TEM images of AgNPs@TC-2.

3.3.2. Metal sensing applications

It is well documented that free tetracycline shows effective interactions with divalent and trivalent metal cations in solution.[166,167] In order to determine any potential metallic interferences during the bacterial studies, and to explore the application as a nanosensor in water, both metallic composites were studied in the presence of Na^{+}, K^{+}, Hg^{+}, Mg^{2+}, Ca^{2+}, Mn^{2+}, Cu^{2+}, Zn^{2+}, Cd^{2+}, Hg^{2+}, Pb^{2+}, Cr^{3+}, Fe^{2+}, Fe^{3+}, Al^{3+}, Ga^{3+}, In^{3+} ions. In our conditions, both systems do not show any remarkable interaction with the metal ions studied with the exception of trivalent cations. The strongest affinity was observed towards Al^{3+}. It is interesting to note that the pink-red colloidal solution of AuNPs@TC shows greater sensitivity (nM range) towards this metal when compared to the AgNPs@TC system (μM range). Moreover, the addition of 500 nM Ga^{3+} or 500 nM In^{3+} promotes a change in the color from red to violet (**Figure 3.7**).

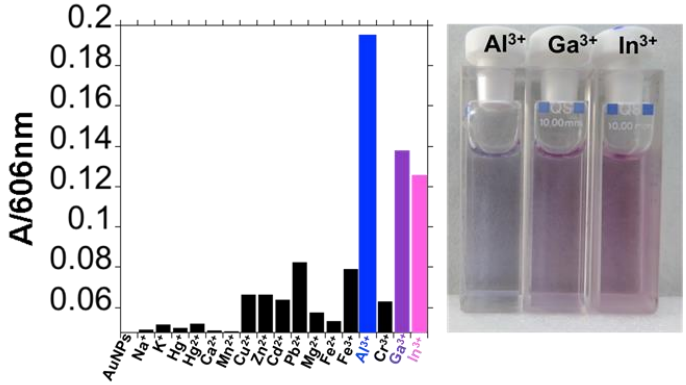

Figure 3.7. Bar diagram showing the intensity of LSRP band at 606 nm for addition of 500 nM of Na^{+}, K^{+}, Hg^{+}, Mg^{2+}, Ca^{2+}, Mn^{2+}, Cu^{2+}, Zn^{2+}, Cd^{2+}, Hg^{2+}, Pb^{2+}, Cr^{3+}, Fe^{2+}, Fe^{3+}, Al^{3+}, Ga^{3+}, In^{3+} and color solution with addition of Al^{3+}, Ga^{3+} and In^{3+}.

The results obtained for the AgNPs@TC composites are showed in **Figure 3.8**.

As a result of the interaction between the Al^{3+} and the AuNPs@TC system, the SPR shifted to lower energy values (red-shift). This confirms the aggregation as a result of lower negative surface charge. The net negative charged surface in the gold system, due to the presence of the tetracycline oxygen atoms, produces a high affinity for trivalent metal cations. Moreover, the larger size obtained with the AuNPs@TC composite induce an increase of sensitivity when compared with the smaller silver material. The increase in the average size of NPs produces a lower surface area of the resulting colloidal system, indicating minor tetracycline molecules functionalized onto the surface of the NPs. With the intention of generating a naked eye colorimetric system, solutions with different SPR absorptions were used. The AuNPs@TC solution producing a color that can be seeing by the naked eye has an absorption value of 0.2. (**Figure 3.9**). Spectroscopic studies with solutions with lower SPR absorption (0.1) showed improvement in sensitivity towards Al^{3+}.

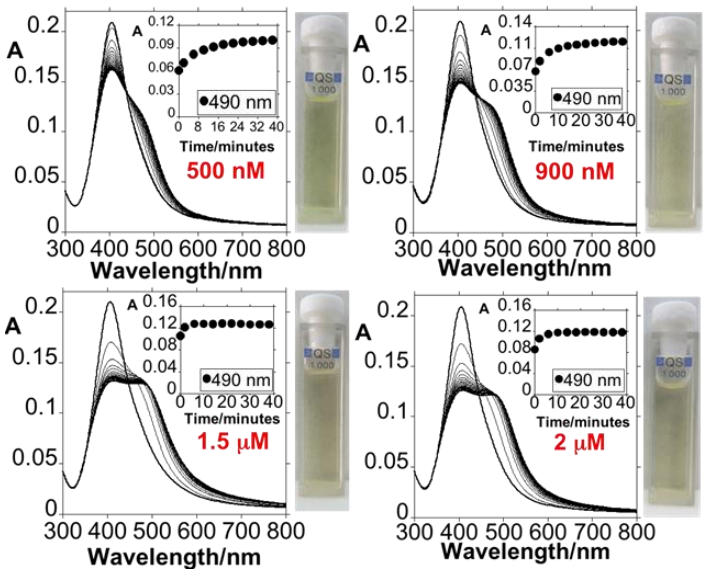

Figure 3.8. Spectrophotometric titration of AgNPs@TC with the addition of increasing amounts of $Al(NO_3)_3$ and naked eye detection.

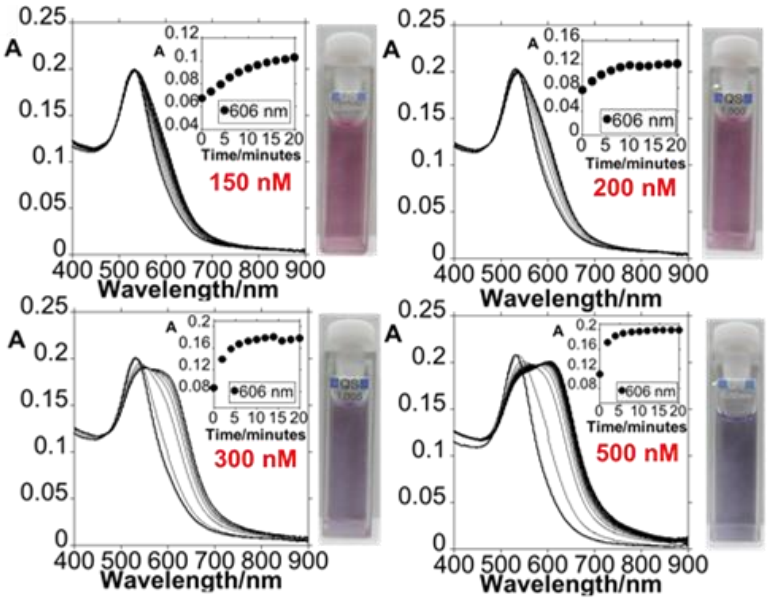

Figure 3.9. Spectrophotometric titration of AuNPs@TC with the addition of increasing amounts of $Al(NO_3)_3$ and naked eye detection.

However, solutions with low SPR absorption cannot be seeing by naked eye. (**Figure 3.11**). The naked eye sensing ability to Al^{3+} was observed for aluminium concentrations ranging between 200 nM and 500 nM. Below 200 nM, the AuNPs@TC exhibits pink color, moving to blue for Al^{3+} concentrations between 200 nM and 500 nM. For concentrations higher than 500 nM, the system moves to blue (**Figure 3.9 and Figure 3.12**).

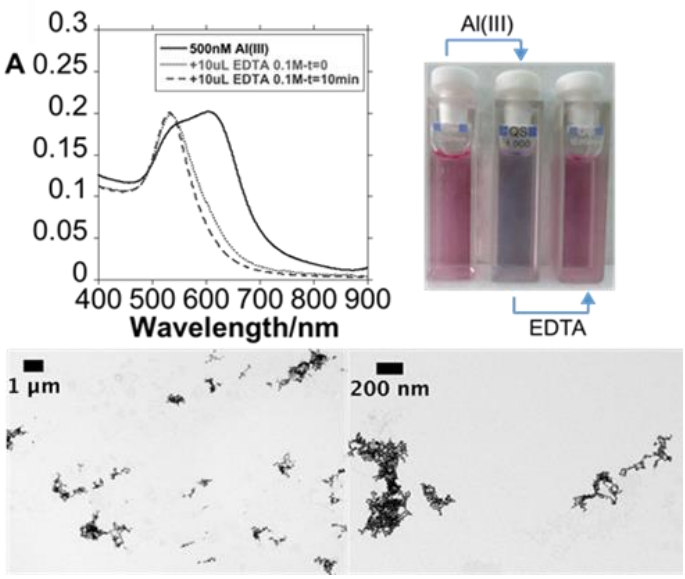

Figure 3.10. Reversible colorimetric change upon addition of EDTA in aqueous solution and TEM images of AuNPs@TC with the addition of 500 nM of $Al(NO_3)_3$

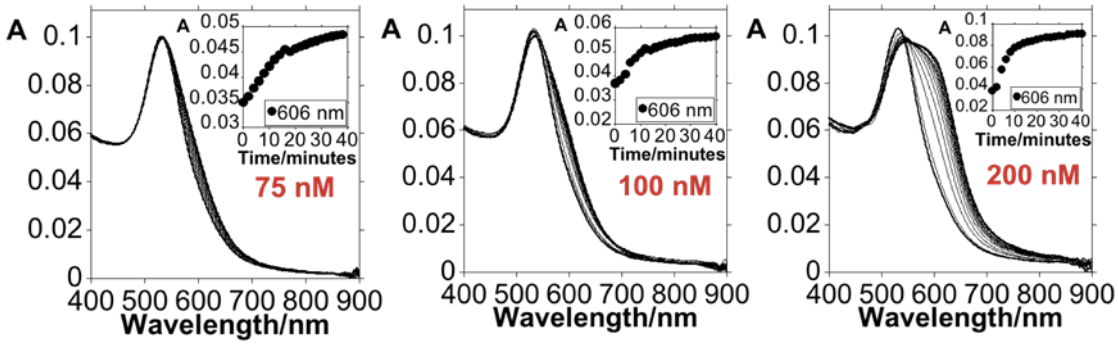

Figure 3.11. Spectrophotometric titration of AuNPs@TC with addition of different fixed quantities of Al(III) with A= 0.1

As can be seen in **Figure 3.10**, large NPs aggregates were observed when AuNPs@TC composite was mixed with a 500 nM Al^{3+} solution. The spatial arrangement of the colloidal system in solution was studied by DLS analysis. A value of 34.03 nm (volume distribution data) was obtained for the free AuNPs@TC composite. Following the addition of 500 nM of Al^{3+}, this value increases up to 381.73 nm (volume distribution data). The formation of aggregates in solution produced by the interaction with Al^{3+}, is supported by the results obtained in the analysis of Z potential. Indeed, the Z potential of AuNPs@TC system present a value of -27.4 mV/cm, and this value rises to -14.16 mV/cm after the addition of 500 nM Al^{3+}.

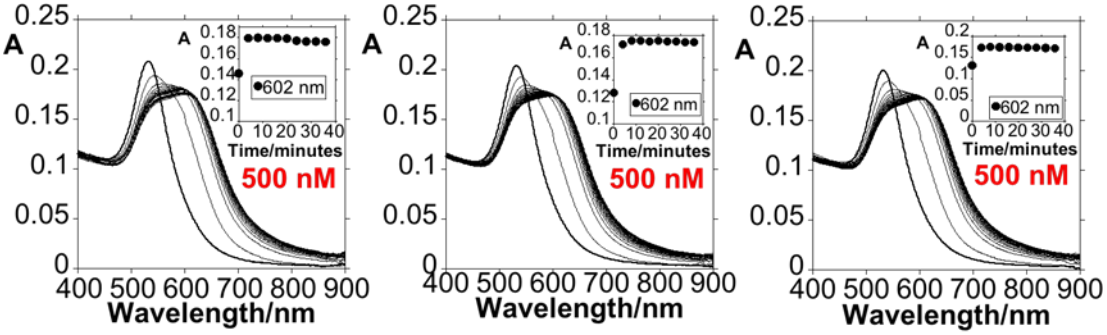

Figure 3.12. Three different replics of spectrophotometric titration of AuNPs@TC with the addition of 500 nM of $Al(NO_3)_3$.

In order to explore the reversibility, the colloid system AuNPs@TC-Al was treated with an EDTA solution. Interestingly, our system recovers its initial optical properties as a result of the complexation of Al^{3+} cations by the EDTA molecule. (**Figure 3.10 and Figure 3.13**)

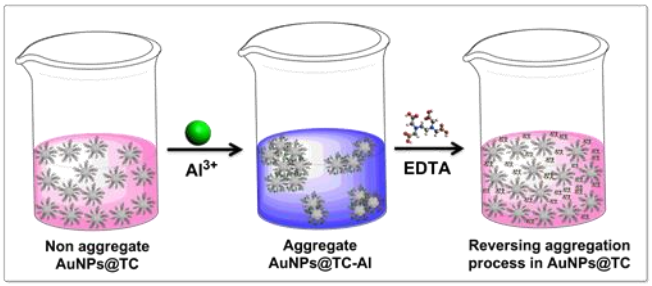

Figure 3.13. Illustrative representation of reversible naked eye sensing of AuNPs@TC towards Al^{3+}.

3.3.3. Exploring Antibacterial activity

As a potential application the use as a bactericidal was tested. To this end *E. coli* and *S. aureus* bacteria susceptible to tetracycline or resistant to tetracycline were used. The AuNPs@TC composites were found not bactericidal (data shown in **Table 3.2**, MBC) neither able to inhibit the growth of *E. Coli* and *S. Aureus* resistant to tetracycline. However, these NPs were able to inhibit the growth of susceptible *E. Coli* and *S. Aureus*. AgNPs@TC composites were found to inhibit growth as well as to kill (i) *E coli* susceptible and resistant and (ii) *S. aureus* susceptible. The best performance was obtained with AgNP@TC-2 composite, as it was found to inhibit and to kill *E. coli* susceptible and resistant as well as *S. aureus* susceptible. However, it fails in killing resistant *S. aureus* at the maximum assayed concentration level. When the bactericidal effects of the nano-composites are compared with the tetracycline alone, the amount of tetracycline required is equal or considerably lower.

Table 3.2. Antimicrobial effect of nanoparticles functionalized with tetracycline, on tetracycline-susceptible and – resistant *E. coli* and *S. aureus* strains.

Nanoparticle	Strain	MIC (μg/mL)	MBC (μg/mL)	pH
AuNPs@TC	*E. coli* K12 ATCC 29425 (**S**)	6	ND	6.8
	E. coli ST648 (**R**)	ND	ND	6.8
	S. aureus ATCC 25923 (**S**)	16	ND	6.6
	S. aureus ST398 (**R**)	ND	ND	6.6
AgNPs@TC	*E. coli* K12 ATCC 29425 (**S**)	16	20	6.8
	E. coli ST648 (**R**)	25	35.5	6.8
	S. aureus ATCC 25923 (**S**)	16	35.5	6.8
	S. aureus ST398 (**R**)	ND	ND	7.0
AgNPs@TC-2	*E. coli* K12 ATCC 29425 (**S**)	32	32	7.2
	E. coli ST648 (**R**)	40	40	6.8
	S. aureus ATCC 25923 (**S**)	32	40	7.0
	S. aureus ST398 (**R**)	62.3	ND	6.8
Tetracycline	*E. coli* K12 ATCC 29425 (**S**)	0.5	16	6.4
	E. coli ST648 (**R**)	128	256	6.0
	S. aureus ATCC 25923 (**S**)	8	128	6.8
	S. aureus ST398 (**R**)	64	256	6.0
AgNPs 15 nm[168]	*E. coli* ATCC 25922[169] (**S**)	30	50	ND
	E. coli ATCC 10536 (**S**)	90	110	ND
	S. aureus ATCC 25923 (**S**)	100	110	ND

TC = Tetracycline; S = Susceptible to tetracycline; R = Resistant to tetracycline; ND = Not Determined. MIC = Minimum Inhibitory Concentration (μg/mL). MBC = Minimum Bactericidal Concentration (μg/mL).

This finding is in agreement with previous studies.[170,171] AuNPs are known to be non-cytotoxic, biocompatible and useful therapeutic drug delivery vehicles.[53,162,172] In this context, we determined that AuNPs@TC is, in fact, nontoxic to bacteria, since it was possible to recover viable bacteria after 36 h of growth in the presence of our AuNPs@TC. Although, it is not bactericidal, AuNPs functionalized with tetracycline are capable of inhibiting tetracycline-susceptible Gram-negative and Gram-positive bacteria.

AgNPs are effective antimicrobial agents, despite the adverse effects of toxicity to both bacteria and eukaryotic cells. In contrast, the cytotoxicity of AuNPs is quite low.[170,172] Our results are in agreement with these fact, once AgNPs@TC showed an improved bactericidal capability than AuNPs, which may arise from the cytotoxicity of silver instead of gold harmlessness. Actually, we concluded that the highest concentration of AgNPs on AgNPs@TC solutions leads to a greater bactericidal and inhibitory effect. As it was previously reported the synergistic effect of silver and tetracycline is evident in our results, since AgNPs@TC solutions had a largely enhanced bactericidal proficiency than tetracycline.[173] The synergistic effect of silver and tetracycline is also demonstrated by comparing microbiological results with those present in the literature using antibacterial AgNPs with similar size without tetracycline and stabilized by citrate molecule, against the same bacteria (different strains).[168] By analysing the MIC and MBC values obtained, our AgNPs@TC have better antibacterial activity against Gram-negative and Gram-

positive bacteria compared to AgNPs stabilized by an innocent citrate molecule which require more concentration to inhibit bacteria growth.

3.4. CONCLUSIONS

A new one-pot method for the synthesis of gold and silver NPs using tetracycline and sodium hydroxide has been described. The new method is less time consuming, requires less handling and ensures that all the tetracycline used is attached to the composite. The nanocomposites are stable during several weeks. The average composite size obtained,15 ± 5 nm and 25 ± 10 nm, guarantees an area to volume ratio appropriate to deliver tetracycline in enough quantity to kill bacteria. Remarkably, the AgNPs@TC-2 system shows bactericidal abilities against Gram-negative and Gram-positive tetracycline-susceptible and tetracycline-resistant bacteria, with better results than tetracycline free and AgNPs. An additional feature of the nanocomposites here described is the enormous sensitivity and selectivity towards Al^{3+} in water. This finding opens the possibility to use this gold system as a reversible colorimetric Al^{3+} nanosensor. Further studies are in progress focusing on the functionalization of Ag and Au NPs with other specific antibiotics.

CHAPTER

4

EXPLORING THE CONTROL IN ANTIBACTERIAL ACTIVITY OF SILVER TRIANGULAR NANOPLATES BY SURFACE COATING MODULATION

Contribution: In this chapter, the candidate has realized the synthesis and functionalization as well as the characterization of all silver triangle nanoplates.

Published in: Djafari, J.; Fernández-Lodeiro, C.; Fernández-Lodeiro, A.; Silva, V.; Poeta, P.; Igrejas, G.; Lodeiro, C.; Capelo, J.L.; Fernández-Lodeiro, J. Exploring the Antibacterial Activity of Silver Triangular Nanoplates by Surface Coating Modulation. *Front. Chem.* (2019), **6**.
DOI: 10.3389/fchem.2018.00677

Presented in: (1) Jamila Djafari, Javier Fernandez Lodeiro, Adrián Fernández-Lodeiro, Carlos Fernández-Lodeiro, Elisabete Oliveira, Hugo M. Santos, José Luis Capelo, Carlos Lodeiro, P41 New silver triangular nanoplates as antibacterial agents: Synthesis and studies. 3rd International Symposium on Nanoparticles, Nanomaterials and Applications, 3rd ISN^{2}A in Aldeia dos Capuchos, Caparica, Portugal, 22th-25th January 2018.
(2) Jamila Djafari, Javier Fdez Lodeiro Adrian Fdez Lodeiro, Carlos Fdez Lodeiro, E. Oliveira, Carlos Lodeiro, Hugo Santos, Susana Jorge, Eduardo Araujo, Jose L. Capelo, P27. Synthesis and characterization of silver triangular nanoplates as antibacterial agent. 2nd International Caparica Christmas Conferences on Translational Chemistry, 2nd IC3TC in Aldeia dos Capuchos, Caparica, Portugal, 4th-7th December 2017.

4.1. INTRODUCTION

Silver nanoparticles (AgNPs) have attracted enormous attention as a result of their particular optoelectronic,[174,175] catalytic,[145,176] or antibacterial properties.[61,71] Engineering modifications of AgNPs size and shape is a fascinating synthetic challenge that allows modification of the final nanomaterial's properties. These structural modifications at the nano-scale level, strongly affect the macroscopic properties of the silver colloidal solutions. For instance, the intense colors of silver colloids are the result of different electron oscillation modes that arise when an electromagnetic field, in the visible range, is coupled to the collective oscillations of conduction electrons.[174] The optical properties can be significantly modified by adjusting the size and/or to the shape of the NPs, allowing a spectral tuning that ranges from the visible to the near IR region. This is particularly true for anisotropic structures such as nanoprisms or nanoplates among others.[30,177]

Similarly to optoelectronic properties, the chemical behavior of silver colloids such as catalytic[178] or antibacterial properties[179] are also much affected by these structural changes aforementioned. In this regard, many researchers have been stated that AgNPs' chemical behavior seems to be related with the different reactivity of the atoms located at the intersections, or in corners, of these nanostructures.[178,180]

Furthermore, the antibacterial effect is one of the most explored applications lying in its excellent effect against a broad spectrum of bacteriological organisms. During the previous decades, the scientific community has debated over the different mechanisms in which AgNPs exert their toxicity towards bacteria and other microorganisms. It has been proved in numerous studies the critical role of silver free ions (Ag^+) in the mechanism of antibacterial action of AgNPs.[65] In this vein, it has been suggested that the morphology of the AgNPs also affects the antimicrobial activity, as an essential indirect factor that mainly influences the release of Ag^+.[62,65]

In this respect, several studies have shown that silver nanoprisms (AgNTs) have more bactericidal action than nanorods or nanospheres proving that the nanomaterial shape strongly influences the bactericidal effect of AgNPs.[60,72,181] Indeed, the presence of high atomic density facets in nanoprim structures such as {111} (like triangular or decahedral shape), induce the increase of the nanoparticle antibacterial activity and seems to be important in the direct interaction within the bacteria surface.[71,179] Furthermore, AgNTs exhibit high surface energy, mainly located at their tips and edges, where silver atoms can be readily oxidized, resulting in either truncation of prism tips or their complete dissolution.[30,177] This significant drawback can significantly limit their physicochemical properties advantages and therefore could reduce the antibacterial application of these nanostructures. Different coating methods have been developed in order to avoid this disadvantage, minimizing this effect and enabling the manipulation of this material as a building block in futures applications.

Many studies around spherical AgNPs have been proved that whether there is organic[65,182,183] or inorganic (usually mesoporous silica) coating[184–186] has an essential influence on AgNPs' antibacterial effect. In this regard, it has been confirmed that the Ag^+ release could be controlled, and as an important consequence, the environmental impacts could be strongly mitigated.

In contrast, the case of AgNTs has been much less investigated. A. Yu et al provided a significant advance about AgNT stabilization using different alkanethiols.[187] These authors report that the Ag-S interactions considerably delay the dissolution of AgNT structures. These important chemical observations were later exploited by Xue et al.,[72] in an elegant work in which the authors demonstrate the perfect AgNT silica coating.

Additionally, it has been demonstrated that amorphous silica coating over AgNPs presents porosity, allowing the diffusion of ions that can oxidize the silver core.[188] The porosity of the amorphous silica has already been proved in studies by different groups.[189,190] Nevertheless, unfortunately, according to the best of our knowledge, the antibacterial properties of AgNTs subjected to alkanethiol or silica coating have not yet been explored.

The goal of the present work is, therefore, to investigate the influences of surface coating of well-defined AgNTs (organic and inorganic) on their optical properties as well as the effects of antibacterial activity against *E. coli* and *S. aureus*. The effect of the surface charge and terminal functional groups (NH_2 or COOH) on AgNTs@SiO_2 was also investigated.

4.2. MATERIALS AND METHODS

4.2.1. Materials

Silver nitrate 99% ($AgNO_3$), sodium borohydride 99% ($NaBH_4$), Sodium citrate tribasic dihydrate 99%, hydrogen peroxide 30% (H_2O_2), polyvinylpyrrolidone (PVP-29K), 16-mercaptohexadecanoic acid 90% (MHA), dimethylamine (DMA) 40% in water, tetraethylorthosilicate (TEOS), (3-Aminopropyl)trimethoxysilane 97% (APTMS), Succinic anhydride 99% (SA) and anhydrous Tetrahydrofuran (a-THF) were obtained from Sigma-Aldrich, and used without previous purification. Anhydrous Ethanol (a-EtOH) was purchased from Carlo Elba. Water was used at Milli-Q grade by Millipore (MQ).

4.2.2. Synthesis of AgNTs in water (AgNTs@PVP) and MHA stabilization (AgNTs@MHA)

The synthesis was carried out in a total volume of 50 mL of MQ water at 30 °C, under ambient atmosphere and laboratory light. Over an aqueous solution of $AgNO_3$ (final concentration of 0.2 mM), under vigorous stirring, trisodium citrate (150 mM, 1 mL), PVP 29K (135 mg/mL, 3 mL), and hydrogen peroxide (30 wt%, 240 µL) aqueous solutions were added. Afterward, a freshly prepared aqueous solution of $NaBH_4$ (final concentration of 1.6 mM) was rapidly added. The solution then immediately turned clear yellow. After 10 min, the colloid solution changed to intense yellow, showing the formation of spherical AgNPs, and then the color solution turned to orange, red, purple, and finally blue. The silver nanoplates were centrifuged at 10,000 rpm during 30min and re-dispersed in ethanol.

The coating of AgNTs@PVP with 16-MHA was carried out by quick addition of an ethanolic solution of MHA (final concentration of 60 µM) on the AgNTs@PVP in EtOH under vigorous stirring and darkness. After 15 minutes, the colloid was centrifugated at 11,000 rpm and re-suspended in ethanol.

4.2.3. Silica coating of AgNTs@MHA to produce AgNTs@Si-OH

An ethanolic solution of TEOS (final concentrations explored between 0.9 mM and 0.4 mM) was added to the colloid AgNTs@MHA in EtOH. Then, an aqueous DMA solution was rapidly injected into the mixture (final concentrations explored between 0.6 M and 0.4 M). The solution was left stirring for 180 or 90 min. at ambient temperature in the dark. The AgNTs@Si-OH were centrifuged several times and washed in ethanol and ultra-pure water. Then the purified colloid was resuspended in ethanol.

4.2.4. Amine derivatization of AgNTs@Si-OH to produce AgNTs@Si-NH_2

The AgNTs@Si-OH colloid was coated with amine silane to convert the AgNTs' surface with amine function. Briefly, under stirring, APTMS in ethanol solution (final concentration of 33.7 µM) was added to an ethanolic solution of AgNTs@Si-OH. Then 1.32% (of total volume reaction) of MQ water was added as catalyzer agent.[191] The reaction was left under stirring overnight. The resulting solution was purified by repeated centrifugation using ethanol and Milli-Q water.

4.2.5. Carboxylic acid derivatization of AgNTs@Si-NH_2 to produce AgNTs@Si-COOH

AgNTs@Si-NH_2 were washed several times in a-THF and finally suspended a-THF. A solution of succinic anhydride in a-THF was added drop-wise to the colloid solution AgNTs@Si-NH_2 until it reached a concentration of 0.52 mM. The reaction was then stirred for 24 h under dark conditions. The resulting AgNTs@Si-COOH were purified several times using THF and then MQ.

4.2.6. Characterization technics

UV-Vis spectroscopy analysis

The UV-Vis spectroscopy studies were performed using a JASCO 630 spectrophotometer provided by the PROTEOMASS-BIOSCOPE facility. The spectra were run between 200 and 1000 nm using a quartz cell (1 cm pathway) under temperature control.

Z-Potential analysis

A MALVERN model ZS instrument provided by the PROTEOMASS-BIOSCOPE facility was used to obtain the Z potential values. A "dip" cell was used to measure the Z potential.

Transmission electron microscopy (TEM) analysis

Microscopy analyses were performed at the CACTI, University of Vigo (Spain). A JEOL JEM1010 TEM operating at 100 kV. All TEM samples were prepared by placing a drop of the sample (5 μL) on a TEM copper grid coated and then air-dried.

Inductively coupled plasma (ICP) analysis

Ag contents in each studied sample were determined in the REQUIMTE-Chemistry Department, FCT-UNL analytical laboratory using an ICP instrument from Horiba Jobin-Yvon (France, model Ultima), equipped with an RF of 40.68 MHz, a 1.00 m Czerny-Turner monochromator (sequential), and an AS500 autosampler.

Fourier-transform infrared spectroscopy (FTIR) analysis.

A Bruker TENSOR spectrophotometer was used to obtain the FT-IR spectra. FT-IR experiments were performed in a KBr disk, provided by the Chemistry Department, LAQV-REQUIMTE, FCT Facilities. To obtain the KBR discs for analysis, each sample was centrifuged and washed in anhydrous EtOH several times until finally resuspending each sample in 100 μL of anhydrous

EtOH. These concentrated solutions were mixed with KBr and the solids were dried under a vacuum pump for 4 h before the preparation of the disks.

4.2.7. Bacterial strains, culture media and growth conditions.

The bacterial strains considered in this study were *Escherichia coli* ATCC 29425 and *Staphylococcus aureus* ATCC 25923 (**Table 4.1**). Bacterial strains were grown in BHI agar (Oxoid, UK) for 24 h at 37 ºC.

Table 4.1. Different strains used in the present study

Strain	Relevant phenotype	Reference
E. coli K12 ATCC 29425	Gram-negative	ATCC
S. aureus ATCC 25923	Gram-positive	ATCC

4.2.8. Preparation of stock solutions

Each solution containing AgNTs was diluted to final concentrations of 1, 5, 10, 25, 50, 75, 100, 150, 200, 300 and 500 µg/mL, and tested on both bacteria.

4.2.9. Antibacterial susceptibility test

The minimum inhibitory concentration (MIC), described as the lowest concentration of NPs that inhibits the bacterial growth, was determined by broth-dilution method using a 96-well polystyrene microtiter plate. Luria-Bertani (LB) (Sigma–Aldrich) broth was prepared, and 135 µL was added to each well. Ten microliters of each solution containing different NPs with concentrations ranging from 1 to 500 µg/mL were added to each well, and 10 µL of overnight cultures of the selected bacteria were inoculated into the wells and incubated at 37ºC. After 24 h, the absorbance was measured with a microplate spectrophotometer. Positive (inoculated medium) and negative controls (medium supplemented with NPs) were included for all tests. All tests were performed in triplicate.

To determine the minimum bactericidal concentration (MBC), which is characterized by no bacterial growth, 100 µL of the cultures resulting from MIC testing were inoculated onto LB medium plates and incubated at 37ºC for 20h. Control cultures without NPs were included in all experiments.

4.3. RESULTS AND DISCUSSION

4.3.1. Synthesis of silver triangular nanoplates and alkane-thiol functionalization

In the present work, all the experiments have been conceived to determine the antibacterial effects of AgNTs as a function of the surface coating. In the literature, a variety of works that report the synthesis of different triangular nanoplates or nanoprisms with an organic coating to explore their antibacterial properties, but to the best of our knowledge only two works report the controlled silica deposition on AgNTs, and none of them explores the antibacterial properties of the resulting product.[72,192]

In the first synthetic step, we synthesized AgNTs@PVP using a *non-seed mediated methodology* based on thermal synthesis developed by Mirkin et al.,[193] and lately revisited by Yin and al. group.[194,195] This photochemical reaction was performed in water with several modifications (see experimental section). We used PVP (29K) as stabilizer, and sodium borohydride as reducing agent, in the presence of shape directors: citrate ion and hydrogen peroxide.

As can be seen in **Figure 4.1** the blue-colored solution obtained and showed an intense absorption band centered at *ca.* 669 nm with a weak shoulder at *ca.* 420 nm that can be assigned to the in-plane dipole and in-plane quadrupole plasmon resonances of AgNTs, respectively. The absence of bands *ca.* around 400 nm (typical of spheres) is indicative of the high yield of AgNTs obtained in this reaction.[30,194]

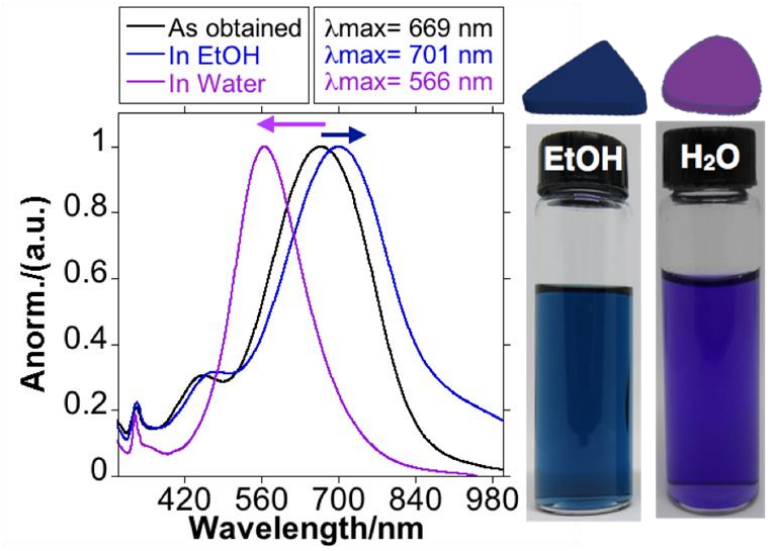

Figure 4.1. Spectroscopic profile and color of AgNTs@PVP resuspended in (blue) EtOH and (purple) Water.

This colloid solution showed high sensitivity to the purification processes, using water as a dispersant. When the NPs were re-suspended in ultra-pure water, there was a fast blue-shift of in-plane dipole plasmon band to *ca.* 566 nm and a disappearance of the in-plane quadrupole plasmon band, with change of the color solution to purple (**Figure 4.1**). This behavior results from the enormous sensitivity of the AgNTs@PVP to suffer tip truncation, or partial dissolution during their manipulation, which strongly affects the final properties.[187]

Purification of the AgNTs@PVP using absolute EtOH as a dispersant did not produce this effect. As shown in **Figure 4.1**, the SPR band red-shifted from *ca.* 669 nm to *ca.* 701 nm as a consequence of the solvent change, which increases the dielectric constant of the medium.[196,197] Another critical factor to be controlled was the centrifugation conditions during the purifications process. We observed that increases in the rotation speed, or in the time cycle, produced the formation of remarkable aggregates, especially when the AgNTs were resuspended in absolute EtOH. The selection of these purification conditions allowed us to obtain well-dispersed AgNTs in the EtOH solution. This final solution was stable for several days without noticeable spectral changes.

TEM analysis of the colloid obtained in EtOH showed AgNPs@PVP with triangular platelet geometry of an average size of 28.8 ± 5.4 nm and a disc width of 5.9 ± 0.9 nm (**Figure 4.2b, d-f**).

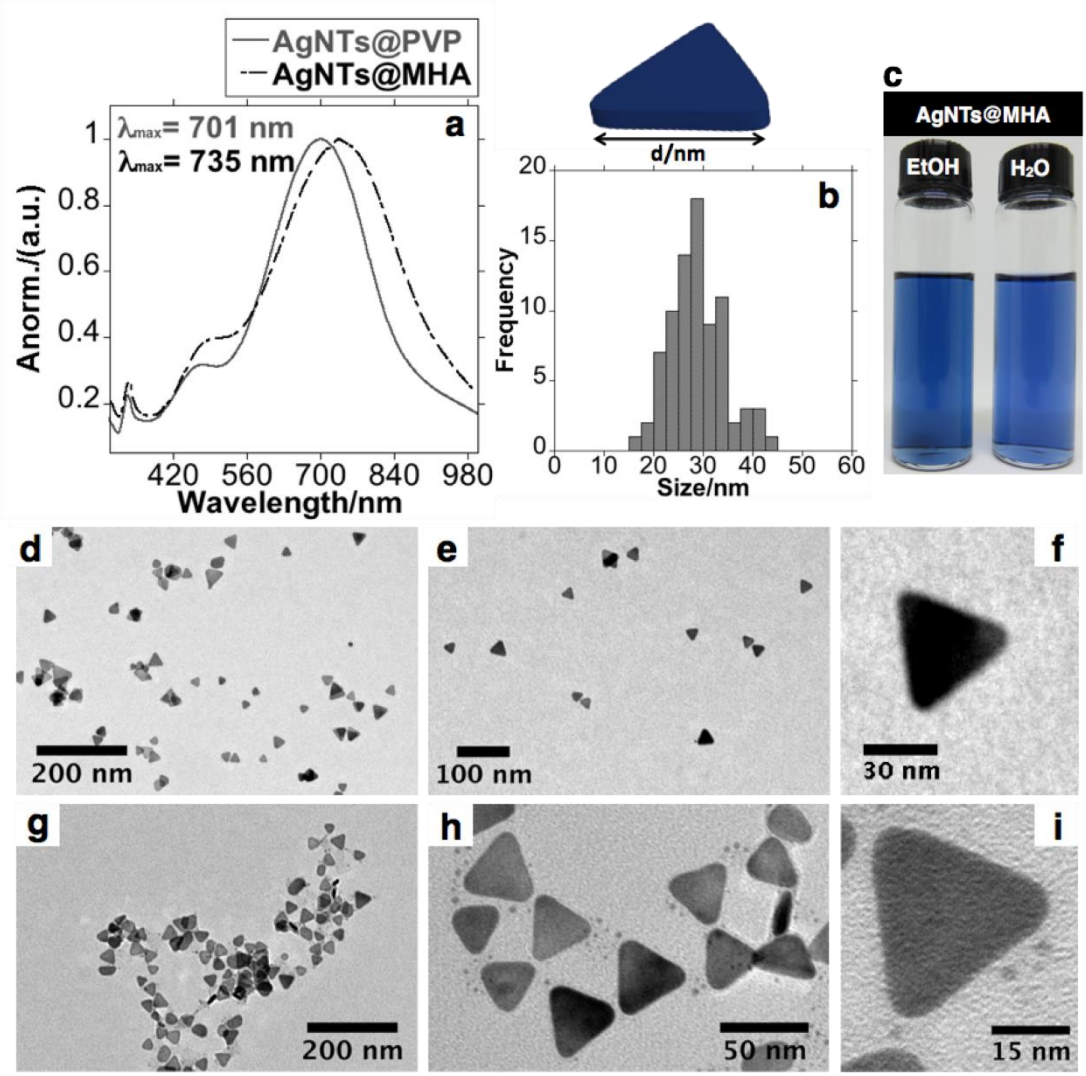

Figure 4.2. (a) Spectroscopic profile of AgNTs@PVP and AgNTs@MHA in EtOH solution. (b) Size histogram of lateral distance of AgNTs@MHA. (c) Color solution of AgNTs@MHA resuspended in EtOH and water. (d, e, f) TEM images obtained of AgNTs@PVP and (g, h, i) AgNTs@MHA.

The marked sensitivity of AgNTs@PVP to manipulation in aqueous solution limits its potential application in antibacterial preparations.

Therefore, in order to increase stability in aqueous solution, the organic functionalization of AgNTs' surface was done by rapid addition of an ethanolic solution of 16-mercaptohexadecanoic acid (MHA) on the AgNTs@PVP solution under vigorous magnetic stirring following previous published methods. The dipole plasmon resonant band red-shifted 34 nm upon organic functionalization with MHA.[72] As presented by the TEM images in **Figure 4.2g-i**, the anisotropic geometry does not show important structural modifications. The thiol-stabilized colloid presents high stability in both EtOH and water solution. The Z-potential analysis of AgNTs@MHA in aqueous solution showed a stable potential of -35.8 mV, confirming the presence of carboxylate groups on the surface of the AgNTs (**Figure 4.7b**)

The FT-IR spectroscopy was employed to inspect the composition of this colloid solution. The CH_2 stretching vibrations peaks detected in AgNTs@MHA correspond to the frequencies observed in the free MHA at 2919 and 2851 cm^{-1}.[198] Contrary to the spectrum of the pure compound, for AgNTs@MHA no signals were detected at 2555 cm^{-1}, which assigned to the ν(S-H) stretching vibration. This fact is indicative, on the one hand, that MHA molecules have adsorbed to the AgNTs' surface through the sulfur group, and on the other hand, of the absence of unreacted MHA molecules on the AgNTs@MHA colloid suspension.[198–200] The band observed at 1559 cm^{-1} in AgNTs@MHA could be assigned to ν(COO^-) symmetric stretch[198] as a consequence of a partial ionization of the carboxylic group of MHA molecules exposed at the silver surface. Finally, the signal observed at 1652 cm^{-1} could be related to the ν(C=O) stretching vibration of carboxylic acid in MHA, or also to the ν(C=O) stretching vibration amide group of remnant PVP adsorbed on the surface of AgNTs@MHA. (**Figure 4.3**). These organic coating AgNTs (AgNTs@MHA) was selected for antibacterial studies.

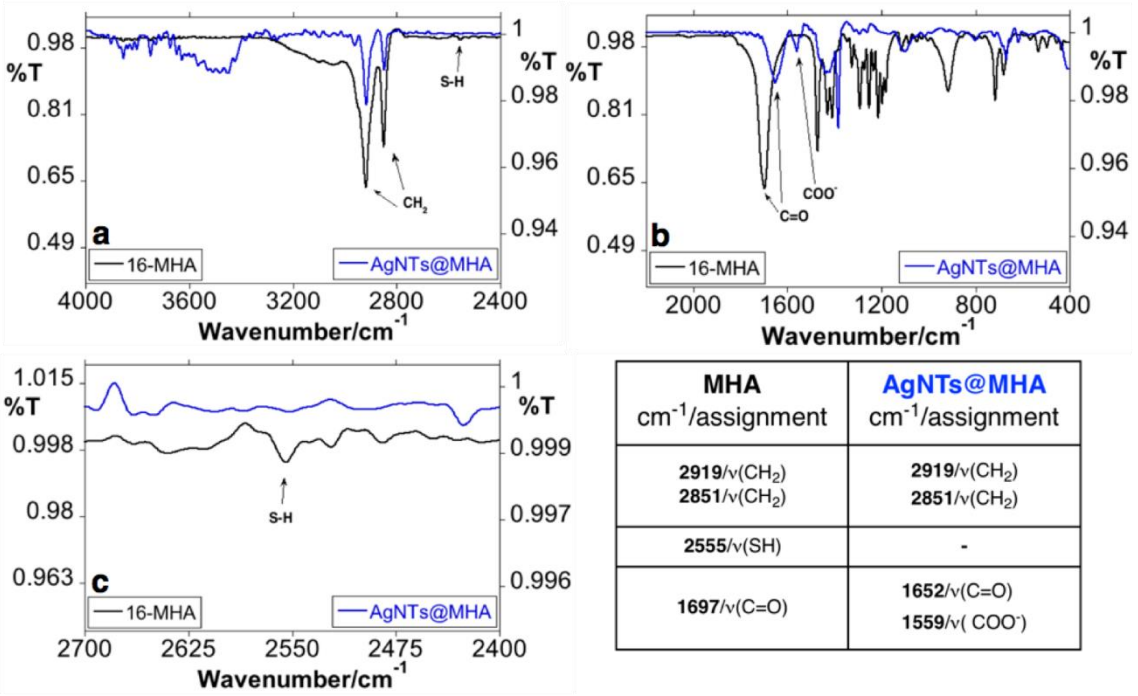

MHA cm^{-1}/assignment	AgNTs@MHA cm^{-1}/assignment
2919/ν(CH_2) **2851**/ν(CH_2)	**2919**/ν(CH_2) **2851**/ν(CH_2)
2555/ν(SH)	-
1697/ν(C=O)	**1652**/ν(C=O) **1559**/ν(COO^-)

Figure 4.3. FT-IR spectroscopic profile of 16-MHA and AgNTs@MHA in KBr disk. Overview between (a) 4000-2400 cm^{-1} and (b) 2000-400 cm^{-1}. (c) Enlargement spectra in the S-H region between 2700-2400 cm^{-1} and FT-IR peak table.

4.3.2. Silica coating of AgNTs@MHA

As reported previously by Mirkin et al. thiol-stabilized AgNTs can be used satisfactorily in the next control of the coating with silica, without affecting the anisotropic structure of the AgNTs.[72] In that work, the authors started with silver nanoprisms synthesized through a photochemical process, using a single beam excitation system in the presence of citrate and bis

(p-sulfonatophenyl) phenylphosphine (BSPP). Then, the AgNTs were functionalized with MHA, and later with a thin and highly uniform silica coating using TEOS as a precursor of silica, and DMA as a catalyst.

In our case, we used AgNTs@PVP as starting material to obtain AgNTs@MHA, and then to produce AgNTs@Si. The silica coating offers an exciting possibility to study how the antibacterial properties of AgNTs@MHA are affected when they are subjected to a dense inorganic coating.

Our intention concerning the silica deposition was to explore the synthetic conditions that allow obtaining a thin but uniform coating, without substantially affecting the anisotropy of the NPs. In this way, keeping constant the DMA concentration (0.5 M) and the reaction time (180 min), we have explored the coating process obtained using different TEOS concentrations between 0.9 mM and 0.5 mM. As can be seen in **Figure 4.4**, for our case, the decrease in the concentration of TEOS during the coating does not permit obtaining a fine homogeneous silica coating. Additionally, all the analyzed samples showed in **Figure 4.4** presented an essential loss of the triangular geometry of the platelets. Interestingly, for the higher concentrations of TEOS explored, we detected the presence of holes within the silica nanostructure **(Figure 4.4a**).

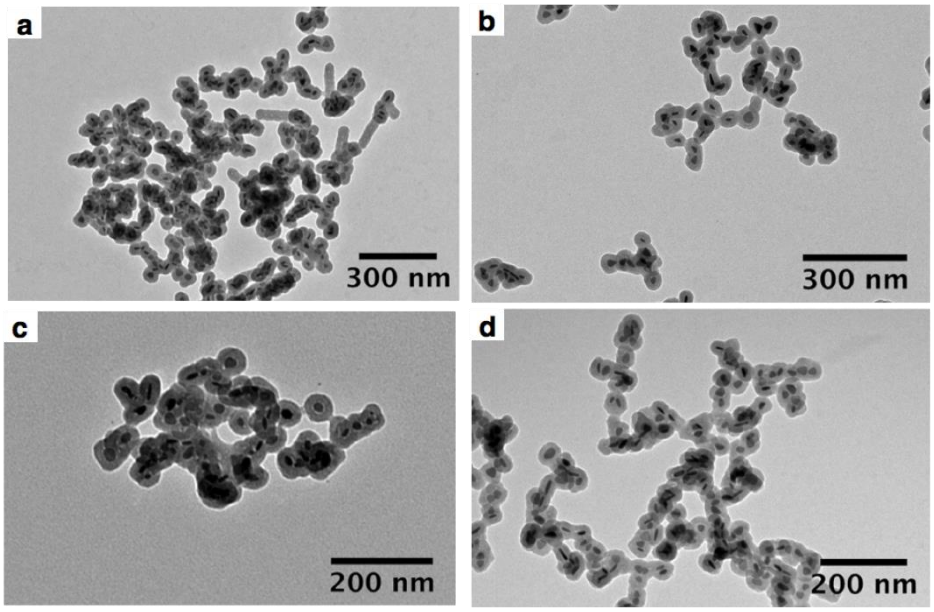

Figure 4.4. Low-resolution TEM images in different magnification of AgNTs@Si-OH obtained under [DMA] = 0.5 M and 3 hours of reaction using different TEOS concentrations. (a) 0.9 mM, (b) 0.7 mM, (c) 0.6 mM and (d) 0.5 mM.

Considering the nanostructures obtained, the dissolution process suffered by AgNTs during the silica deposition seems to be affected to a large extent by the contact time of the nanostructures with the DMA and/or the concentration of the same.

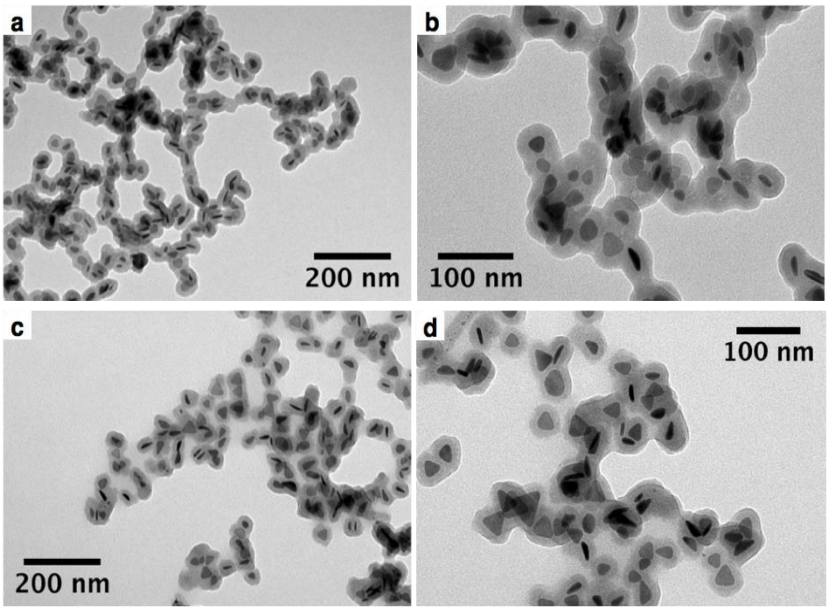

Figure 4.5. Low-resolution TEM images in different magnification of AgNTs@Si-OH obtained under [TEOS] = 0.5 mM, [DMA] = 0.5 M for (a and b) 180 min and (c and d) 90 min.

Based on the previous observations related to the TEOS concentrations, using 0.5 mM, we have decreased the reaction time to 90 min. In **Figure 4.5**, it can be seen after just 90 min. of reaction, the silica coating showed a homogenous character overall of silver cores. Remarkably, we conclude that in our process, the re-shaping of AgNTs is preserved to a greater extent for the reaction obtained with 90 min, indicating that more significant contact with DMA, produces higher re-shaping of the AgNTs, probably by diffusing of DMA through the already-formed silica shell.

Finally, for a concentration of TEOS of 0.5 mM, and 90 min of reaction, we have explored the decrease in the concentration of DMA to 0.4 M. The reduction of the concentration of DMA, not only allowed us to preserve to a greater extent the anisotropy of the AgNTs but also allowed us to obtain relatively homogeneous silica coating. Consequently, the refined synthetic conditions were [TEOS] = 0.5 mM, [DMA] = 0.4 M and 90 min. allowing us to obtain a silica coating thickness around 5 nm (**Figure 4.6a-c, g**).

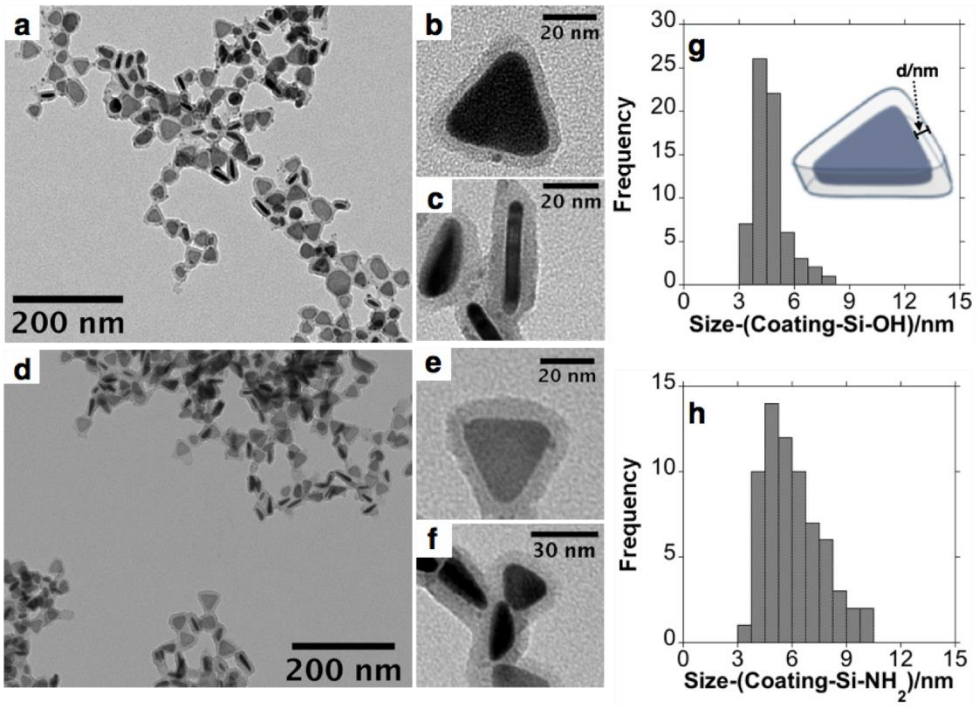

Figure 4.6. Low magnification TEM images at different magnifications obtained for (a to c) AgNTs@Si-OH and (d to f) AgNTs@Si-NH_2 and size histogram of silica coating for (g) AgNTs@Si-OH and (h) AgNTs@Si-NH_2.

The dipole plasmon resonant band of AgNTs@MHA red-shifted in 27 nm, upon silica coating (**Figure 4.7a**), following previous similar reports.[72]

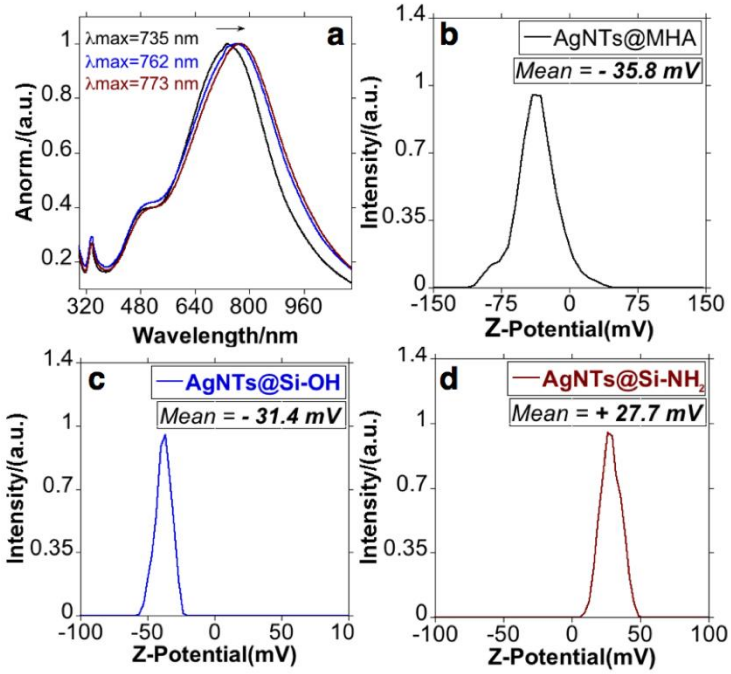

Figure 4.7. Spectroscopic profile of (a) AgNTs@MHA, AgNTs@Si-OH and AgNTs@Si-NH_2 in EtOH, and graphic representation of the Z-potential for (b) AgNTs@MHA, (c) AgNTs@Si-OH and (d) AgNTs@Si-NH_2.

Using FT-IR spectroscopy, the characteristic signals for silica were observed at 467, 800, 960 and 1094 cm^{-1} (**Figure 4.8**). These signals can be assigned to the bending vibration of Si–O-Si, stretching and bending vibrations of Si-OH and asymmetric stretching vibration of O-Si-O respectively[201–203] confirming the polymerization of silane on the silver cores.

In a subsequent step, we have derivatized the terminal -OH group of AgNTs@Si-OH into $–NH_2$ through a silane coupling reaction with APTMS, based on established protocols.[191] As shown by the TEM images in **Figure 4.6d-f** through APTMS coupling on AgNTs@Si-OH, we obtained a slight increase in shell silica size (≈ 1.3 nm) (**Figure 4.6h**). This functional group conversion can be readily confirmed using Z-potential analysis of the colloids in water. Therefore, the AgNTs@Si-OH have a surface charge equal to -31.4 mV, which is reversed to positive values +27.7 mV for AgNTs@Si-NH_2 (**Figure 4.7c,d**). This Zeta potential value reversion is the consequence of the different energies of ionization in water presented by the -OH and -NH_2 groups.[204,205]

These positively-charged AgNTs@Si-NH_2 were selected as the second sample for bacteriological analysis.

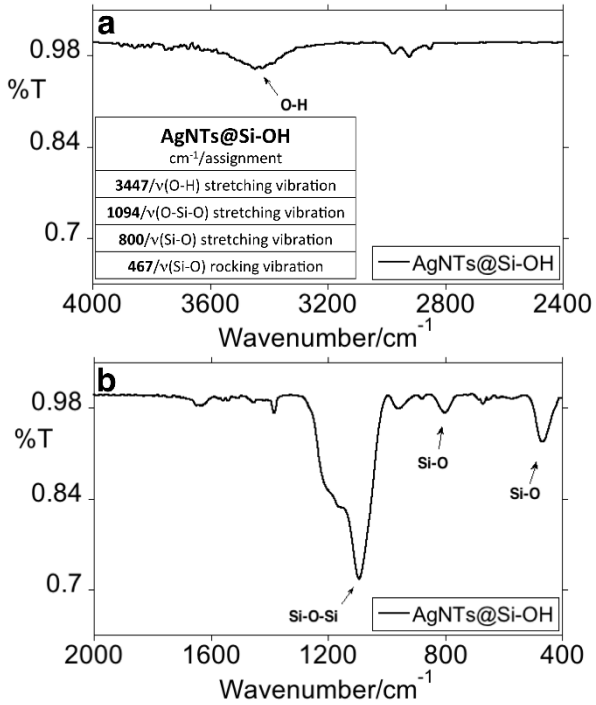

Figure 4.8. FT-IR spectroscopic profile of AgNTs@Si-OH in KBr disk. Overview between (a) 4000-2400 cm^{-1} and peak table and (b) 2000-400 cm^{-1}.

Finally, to explore if the effect of surface charge can affect the antimicrobial properties of silica-coated AgNTs, we have converted the terminal organic amine group (-NH_2) into the carboxylic acid (-COOH) reacting AgNTs@NH_2 with succinic anhydride in anhydrous THF. As can be seen in the **Figure 4.9a**, the LSRP was not significantly affected. On the other hand, upon

conversion of an amine into the carboxylic group, the Z-potential of the colloid in ultrapure water was moved from +27.7 mV to -26.0 mV which was in accordance with previous reports about AgNPs@Si functionalization.[206]

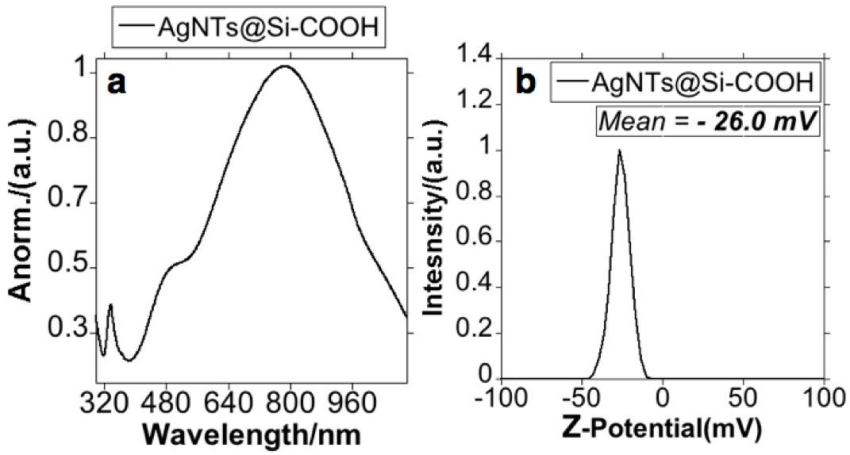

Figure 4.9. Spectroscopic profile of (a) AgNTs@Si-COOH and (b) graphic representation of the Z-potential for AgNTs@Si-COOH.

The negatively-charged AgNTs@Si-COOH were selected as the third sample for bacteriological analysis.

4.3.3. Exploring bactericidal properties

The antibacterial susceptibility tests were performed by the broth dilution method. Previous studies have proved that AgNPs alone and silver composites have high antibacterial effectiveness against bacteria, fungi, and virus.[207–209] The minimum inhibitory concentration (MIC) and the minimal bactericidal concentration (MBC) values are shown in **Table 2**.

Based on the MIC/MBC values obtained for the three selected samples, we have confirmed that the AgNTs that were only subjected to organic coating (AgNTs@MHA) showed the best antimicrobial properties, with MIC/MBC values of 10/10 and 5/10 (µg/mL) for *E. coli* and *S. aureus* respectively. Compared with other studies using different spherical silver NPs, AgNTs@MHA show suitable antimicrobial properties.

For instance, AgNPs@citrate ranged in size between 5 and 100 nm, showing MICs that varied from 20 to 160 µg/mL for the two tested strains *E. coli*.[168] Besides, AgNPs@PVP in a range of sizes between 9 and 16 nm showed higher MBC values than those obtained in our case for AgNTs@MHA for the same bacterial strain *S. aureus* (ATCC 25923).[210]

Note that in our previous study using 15 nm spherical AgNPs stabilized with tetracycline, higher MIC values against the same bacterial strains studied in the present work were visible (between 16 and 32 µg/mL).[211] These important results show how the rational selection of the

shape in silver NPs could overcome the synergistic effect produced by spherical shape and tetracycline.

The present results, therefore, are in agreement with previous works which elucidate a greater antibacterial effect of NPs with {111} basal plane.[71] More specifically, Sadeghi and co-workers studied the antimicrobial effect of PVP-stabilized nanospheres, nanobars, and nanoplates against *E. coli* and *S. aureus*.[179] These authors proved a marked increase in the antimicrobial effect for nanoplates when compared to nanobars and nanospheres, as consequence of higher surface area observed for nanoplates.

Studies on the impact of AgNTs' surface coating on antibacterial activity remain limited to organic coating, and have highlighted antibacterial properties.[212–216] For instance, pluronic-coated nanoprisms have been successfully used as a bactericidal agent against two methicillin-resistant *S. aureus* strains. These authors observe strong bacteriostatic and bactericidal activity related to the high sensitivity of the tips and edges of AgNTs to undergo oxidation.[214]

However, the inorganic coating of AgNTs has never been explored for antibacterial applications. Silica is presented as an ideal candidate since it favors stability to oxidation,[192] decreases non-specific interactions between the metallic surface and biomolecules,[217] increases solubility in aqueous media or facile production and post-functionalization processes[206] among others advantages.

Related the samples subjected to silica coating, a decrease in the antibacterial effect concerning AgNTs@MHA can be noted by the MIC/MBC values summarized in **Table 4.2**. We believe that the subsequent coating of AgNTs@MHA with silica should delay the dissolution processes of AgNTs, decreasing the Ag^+ ratio released.

Despite this, the MIC/MBC values obtained between 5 and 50 μg/mL showing notably antimicrobial effect. More important, the bactericidal effect against *S. aureus* ATCC 25923 was not altered after silica coating for the case of AgNTs@Si-NH_2, indicating that the release of silver ions is probably not a determinant factor in the antibacterial activity of positively charged AgNTs against this specific strain. Note that the antibacterial effect obtained for AgNTs@Si-COOH in the two bacterial strains was decreased when compared to AgNTs@MHA. Therefore, the surface charge of AgNTs should be considered in the mode of action against *S. Aureus*. In this regard, it has been previously suggested that positively-charged AgNPs grant a higher antimicrobial effect when compared to similar negatively-charged NPs.[182]

Finally, and supporting our results, it has been pointed out by different authors that after the silica coating the AgNPs retain their antibacterial properties.[184,218]

Table 4.2. The minimum inhibitory concentration (MIC) and minimum bactericidal concentration (MBC) of AgNTs@MHA, AgNTs@Si-NH_2, and AgNTs@Si-COOH toward *E. coli* K12 ATCC 29425 and *S. aureus* ATCC 25923.

Sample	Strain	MIC (µg/mL)	MBC (µg/mL)
AgNTs@MHA	*E. coli* K12 ATCC 29425	10	10
	S. aureus ATCC 25923	5	10
AgNTs@Si-NH_2	*E. coli* K12 ATCC 29425	25	50
	S. aureus ATCC 25923	5	10
AgNTs@Si-COOH	*E. coli* K12 ATCC 29425	25	50
	S. aureus ATCC 25923	10	25

4.3.4. Proposed mechanism

The antibacterial effect of silver ions and AgNPs has been known for decades. Silver ions (Ag+) are reported to disrupt the outer membrane of target bacterial cells, however, this effect has been observed at concentrations much higher than those used for AgNPs. The antibacterial effect of AgNPs may be due to the large surface area provided by the AgNPs which facilitates the attachment of the NPs to the cell membrane and, consequently, an easier penetration into the bacteria.[219] Several studies and reviews[64,220,221] have elucidated the probable modes of action of AgNPs: 1) the AgNPs adhere and accumulate on the bacteria surface then penetrating the cell wall which can cause structural changes in the cell membrane leading to a higher permeability. Besides, the accumulation of AgNPs on the bacterial membrane produces gaps compromising the integrity of the membrane causing increased permeability and, consequently, cell death; 2) the AgNPs may release silver ions that interact with the enzyme's thiol groups inactivating them. The silver ions may also enter the cell membrane inhibiting some cell functions; 3) silver ions may inhibit the respiratory chain enzymes or interfere with membrane permeability due to the uncoupling of respiratory electron transport from oxidative phosphorylation resulting in impaired DNA replication. The reactive oxygen species (ROS) are produced through the inhibition of respiratory chain enzymes which have a known powerful antibacterial activity; 4) the silver ions have the ability to enter the bacterial cell, inhibiting the protein synthesis and interfering with the translation and transcription; 5) finally, silver is an acid and the cells are mostly made out basic components (phosphorous and sulfur), therefore, they tend to react with each other resulting in cell death. Besides, the major components of DNA are bases, and the AgNPs may interfere with them destroying the DNA of the bacterial cell.

We believe that the mechanism of action of AgNTs should proceed in a similar way to that observed for spherical NPs, but with increased Ag^+ release ratios, as well as a greater surface adsorption on bacteria. **Figure 4.10** illustrates the possible mechanisms of the antibacterial effects of AgNTs.

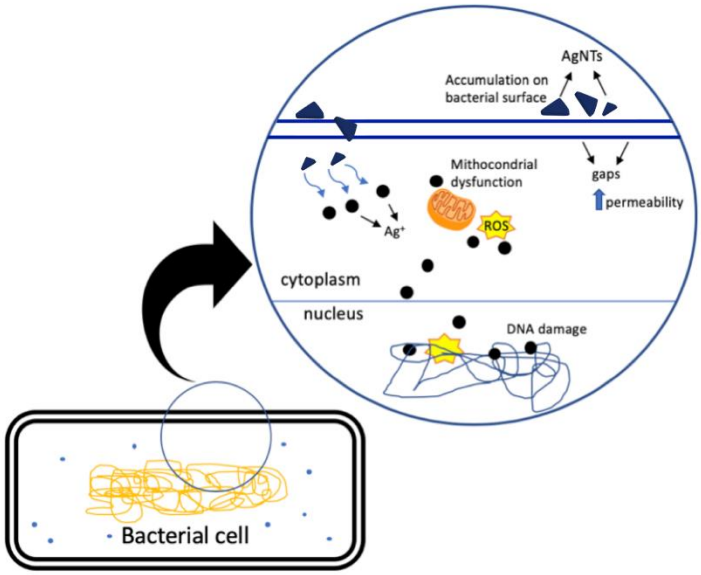

Figure 4.10. Plausible antibacterial mechanisms of AgNTs action

4.4. CONCLUSIONS

We have successfully synthesized silver nanotriangles, AgNTs@PVP, in aqueous solution. Afterward, functionalization with 16-mercaptohexadecanoic acid (AgNTs@MHA) and the subsequent silica deposition were deeply investigated. We have determined the ideal synthetic conditions to obtain amorphous silica coating with ≈ 5 nm. Terminal amine functionality was introduced through a chemical reaction with APTMS, increasing the shell thickness to ≈ 1.3 nm. Amino group terminated nanoparticles (AgNTs@SiNH$_2$) then reacted with succinic anhydride in THF to obtain AgNTs@Si-COOH. The bacterial properties of AgNTs with a molecular coating (AgNTs@MHA), and silica coating (AgNTs@Si-NH$_2$ and AgNTs@Si-COOH) were investigated against Gram-positive and Gram-negative bacteria.

Comparing the three explored samples, the higher antibacterial effect was observed for the silica-free sample as expected, showing the best MIC values against *S. aureus* (ATCC 25923) equal to 5 µg/mL. We have observed that the silica coating decreases the antibacterial effect for all the strains studied, except for the case of the positively charged AgNTs@Si-NH$_2$ against *S. aureus* (ATCC 25923). These results indicate that the release of silver ion is not the unique critical point in the mode of action of AgNTs; nonetheless, the surface charge must also be taken into consideration. Even so, the MIC/MBC values for the silica-coated samples showed a similar range to the values reported in the literature for another type of uncoated-silica AgNPs.

As an important final remark, it should be mentioned that the high aqueous colloidal stability and the presence of terminal organic groups (COOH or NH_2) in the explored nanomaterials, both open the door to the design of more sophisticated nano-antibiotics though rational organic functionalization with bactericide-active molecular agents. Currently the application of these materials as building blocks to produce hybrid nano-antibiotics is under development in our laboratory.

CHAPTER

5

IRON(II) AS GREEN REDUCING AGENT IN GOLD NANOPARTICLE SYNTHESIS

Contribution: In this chapter, the candidate has realized the synthesis and characterization of gold nanoparticles.

Published in: Djafari, J.; Fernández-Lodeiro, A.; García-Lojo, D.; Fernández-Lodeiro, J.; Rodríguez-González, B.; Pastoriza-Santos, I.: Pérez-Juste, J.; Capelo, J.L.; Lodeiro, C. Iron(II) as green reducing agent in gold nanoparticle synthesis. *ACS Sustainable Chem. Eng.* (2019), **7**, 8295-8302.

DOI: 10.1021/acssuschemeng.8b06690.

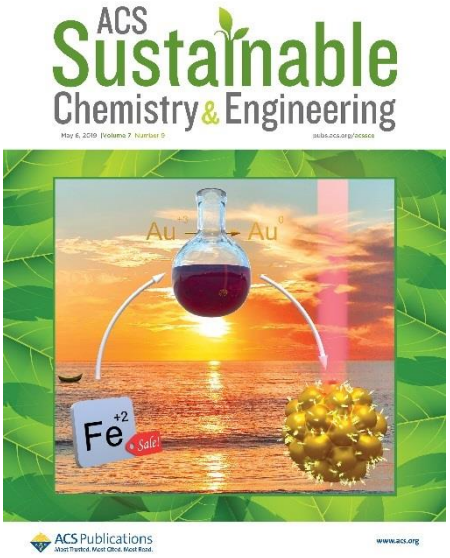

5.1. INTRODUCTION

Since the seminal studies on the interaction of light with metal NPs of Michael Faraday[13] and the development of Turkevich's citrate method in 1951,[58] countless efforts have been made not only to fine-tune shape, size and composition of metal NPs but also to investigate their uncommon physical and chemical properties. Particularly, such size- and shape-dependent properties have made AuNPs highly attractive for a wide range of applications in sensing,[144] imaging,[222] therapy,[223] photovoltaics,[224] (photo)catalysis,[225] among others. AuNPs are often obtained as colloids in aqueous or non-aqueous solvent through the reduction of a gold precursor (in the presence or absence of preformed Au seeds). In the last two decades, a wide range of strategies has been developed to synthesize AuNPs with tailored size, shape and surface functionality.[226] Interestingly, despite the inherent low toxicity of AuNPs, numerous synthetic approaches employ hazardous chemicals, which can be problematic for further application of gold, especially in biomedicine. Thus, organic solvents, such as DMF or polyol,[227] capping ligands, such as CTAB,[131] oleylamine,[228] polymers,[229] or reducing agents, such as sodium borohydride or hydrazine, are hazardous compounds commonly used for AuNPs preparation. In response to these concerns, scientists are actively working in the development of green synthetic approaches involving the use of extracts from organisms,[230] human and microbial living cells,[231,232] or biomolecules such as proteins, sugars or nucleic acids.[233–235] Unfortunately, most of these bio/green-related methods do not allow a fine tuning of AuNPs size and morphology.

From an Earth perspective, iron is the most abundant element by mass, being inexpensive and easy to obtain. Besides iron oxides and iron salts exhibit low toxicity which makes their use in nanoparticle synthesis sustainable. Historically, iron(II) sulphate have been extensively exploited in food technologies,[236] chemical industry,[237] and precious metal recovery technologies.[238] For instance $FeSO_4$ has been widely used for recovery, through precipitation, of Au produced during the large scale extraction of nickel, copper and other elements in mining.[238] Recently, "urchin-like" Au mesostructures have been obtained by reducing a gold precursor with Fe suspension in water. Nevertheless, the mechanism involved in the Au salt reduction is not elucidated.[96]

In the present work, we demonstrate that $FeSO_4$ can be used as green and sustainable reducing agent for the aqueous synthesis of AuNPs. The effect of different parameters such as, temperature, Au(III):Fe(II) molar ratio and presence of non-toxic capping agents in the reduction process of Au salt and in the AuNPs growth are analyzed. Additionally, we have investigated the effect of modulating the formal redox potential of Fe(II), through its complexation with citrate, in the synthesis of AuNPs. Finally, using a Raman active molecule, such as 4-nitrothiophenol (4-NTP), we evaluate the Surface Enhanced Raman Scattering (SERS) efficiency of the different

AuNPs obtained for three excitation laser lines. Additionally, the limit of detection (LOD), the quantification range and the analytical enhancement factors (AEFs) are also reported.

5.2. MATERIALS AND METHODS

5.2.1. Materials

Tetrachloroauric acid trihydrate ($HAuCl_4.3H_2O$), iron (II) sulfate heptahydrate ($FeSO_4.7H_2O$), trisodium citrate dihydrate ($Na_3C_6H_5O_7.2H_2O$), iron (II) chloride tetrahydrate ($FeCl_2.4H_2O$), sodium chloride (NaCl), poly(sodium 4-styrenesulfonate) (PSS, Mw 70,000) and 4-nitrothiophenol (4-NTP) were purchased from Sigma-Aldrich. Potassium bromide (KBr) was purchased from Alfa-Aesar. All chemicals were used without further purification. Milli-Q grade (type I) was used in all preparations.

5.2.2. Iron(II) mediated synthesis of AuNPs.

PSS free synthesis: In a typical experiment, to 28 mL of water thermostatized at 30 or 60 ºC, 1 mL of $HAuCl_4$ aqueous solution (7.5 mM) was added under vigorous stirring. Subsequently, 1 mL of $FeSO_4$ aqueous solution (0.75, 1.5 and 2.25 mM, final concentrations) was rapidly injected. The reaction was allowed to react for 15 minutes before cooling down to room temperature (RT). Finally, the resulting NPs were purified by centrifugation (4,000 rpm for 15 min) and resuspended in water.

5.2.3. PSS-assisted Au nanoparticles synthesis

Briefly, to 28 mL of PSS aqueous solution (see text for details) thermostatized at certain temperature (30, 60 or 100 ºC) 1 mL of $HAuCl_4$ aqueous solution (7.5 mM) was added under vigorous stirring. Afterwards, 1 mL of $FeSO_4$ aqueous solution was rapidly injected. The reaction was allowed to react for 15 minutes and then the solution was cooled down to RT. Finally, the resulting NPs were purified by centrifugation (4,000 rpm for 5 min) and the pellet resuspended in 8 mL of water.

5.2.4. (Fe^{2+}/Citrate)-mediated synthesis of Au nanoparticles

In a typical synthesis, 1 mL of a freshly prepared $FeSO_4$ aqueous solution was added to 28 mL of aqueous solution containing sodium citrate (see text for details) and PSS at 40 ºC.

Subsequently 1 mL of 15 mM $HAuCl_4$ solution in water was rapidly added. After 60 min the solution was cooled down to RT and the obtained NPs were centrifuged twice (6,000 rpm for 15 min) and the pellet redispersed first in an aqueous solution of 2.4 mM sodium citrate and finally in water.

5.2.5. Characterization techniques.

The extinction spectra were recorded using a JASCO 650 UV-Vis-NIR spectrophotometer provided by the Proteomass-Bioscope facility (Caparica – Portugal). In all spectra a HELMA 1 cm light path quartz cell was used. DLS and Z Potential analysis were carried out in A Malvern model ZS instrument provided by the Proteomass-Bioscope facility (Caparica – Portugal). Fourier Transform Infrared (FT-IR) analysis was performed using a Bruker Tensor 27 instrument. Low magnification transmission electron microscopy (TEM) images were obtained using a JEOL JEM 1010 TEM microscope, working at 100 kV. Additionally, a JEOL JEM 2010F field-emission gun TEM working at 200 kV was used to obtain high resolution TEM (HRTEM) images. Particle size and mean size distribution were calculated from TEM micrographs using ImageJ package.[239]

Scanning electron microscopy (SEM) images were obtained in a Carl Zeiss AURIGA CrossBeam FIB-SEM and in a JEOL JSM 6700F cold FEG gun. Samples were prepared by dropping the sample onto a silicon wafer and air-dried. Inductively coupled plasma (ICP) analysis to determine Au content of samples was carried out with a Horiba Jobin Yvon ULTIMA 2 ICP OES spectrometer equipped with a 40.68 MHz RF generator, and a 1.00 m Czerny–Turner monochromator with 1.00 m (sequential) and an autosampler AS500.

Raman and SERS measurements were conducted with a Renishaw InVia Reflex system. The spectrograph used a high-resolution grating (1200 or 1800 grooves/cm) with additional band-pass filter optics, a confocal microscope and a 2D-CCD camera. SERS characterization was carried out using a macrosampler accessory for measurements in the liquid state. For SERS measurements the concentration of the samples were adjusted to 0.5 mM in terms of gold concentration. To each sample the model analyte at desired concentration was added and after 90 min, time enough to reach thermodynamic equilibrium, SERS spectra were recorded (10 measurements were collected for each sample) using an excitation laser line of 633 (7.6 mW), 785 (72 mW), 830 (1.2 mW) with an acquisition time of 10 s. WiRE Software v.4.3 (Renishaw, UK) was used for data analysis.

5.3. RESULTS AND DISCUSSION

Considering the standard reduction potentials for Fe(III) to Fe(II) (**Equation 5.1**) and for Au(III) to Au(0) (**Equation 5.2**), the reduction of Au(III) ions by Fe(II) cations should be favorable under standard conditions (**Equation 5.3**).

$Fe^{3+} + e^- \leftrightarrows Fe^{2+}$	$E^0 = 0.77\ V$	**Equation 5.1**
$AuCl_4^- + 3e^- \leftrightarrows Au^0 + 4Cl^-$	$E^0 = 0.93\ V$	**Equation 5.2**
$3Fe^{2+} + AuCl_4^- \leftrightarrows Au^0 + 3Fe^{3+} + 4Cl^-$	$E_r = +0.16\ V$	**Equation 5.3**

To investigate the reducing capabilities of Fe(II) to synthesize AuNPs from $AuCl_4^-$ as precursor, experiments maintaining constant Au(III) concentration (0.25 mM) and varying Fe(II) concentration from (0.75 mM to 2.25 mM) were carried out at 30 ºC. Thus Au(III):Fe(II) molar ratios of 1:3, 1:6 and 1:9 were studied. $FeSO_4$ was used as Fe(II) precursor. Regardless of the molar ratio, the mixing of both compounds (See experimental section for details) gave rise to a color change in 15-20 s from light yellow (from the Au(III) salt) to colorless to green/grey indicating that, as predicted by the standard reduction potentials, the redox reaction (**Equation 5.3**) is favorable. It should be mentioned that the observed color change from light yellow to colorless (15-20 s) could be ascribed to an initial reduction step from Au(III) to Au (I) as observed by Moodly and coworkers.[240] The characterization of the resulting dispersions by Vis-NIR spectroscopy (**Figure 5.1A**) revealed the formation of AuNPs with broad localized surface plasmon resonance (LSPR) bands centered in 700-900 nm region. Moreover, it should be noted

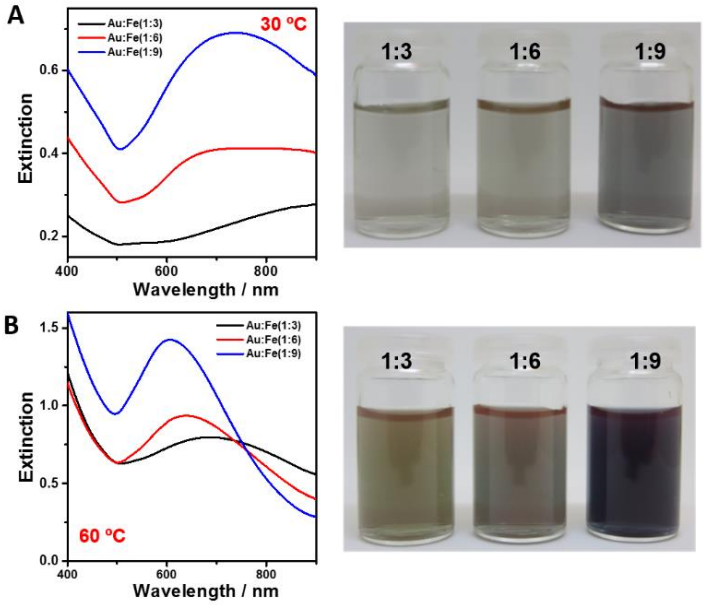

Figure 5.1. (Left) Extinction spectra and (Right) corresponding photographs of AuNPs dispersions obtained with different Au(III):Fe(II) molar ratios, as indicated, at 30 ºC (A) and 60 ºC (B).

that as the Au(III):Fe(II) molar ratio decreased, there is an overall decrease in extinction intensity (less amount of Au(0)) indicating that the reaction is far from being stoichiometric.

Since the reaction is not stoichiometric at 30 ºC and the reducing power is often temperature dependent,[241] similar experiments were performed at 60 ºC. As shown in **Figure 5.1B**, the extinction spectra of the resulting dispersions show larger extinction intensities and LSPR bands at higher energies than those obtained at 30 ºC (**Figure 5.1A**). This indicates a higher Au(III) reduction yield and smaller NPs (larger amount of nuclei during nucleation step). Nevertheless, the reduction yield was still dependent of the Au(III):Fe(II) molar ratio reaching the best yields for 1:9. At this molar ratio the colloids exhibit a broad LSPR band centered at ca. 600 nm and transmission electron microscopy (TEM) (**Figure 5.2**) revealed the presence of polydisperse AuNPs with a surface coating. FT-IR analysis of the AuNPs indicates that the coating most probably consists of different Fe(III) or Fe(II) oxo/hydroxo sulfates that precipitated on the NPs surface (acting as nucleation center) due to its relatively low solubility (**Figure 5.3**).

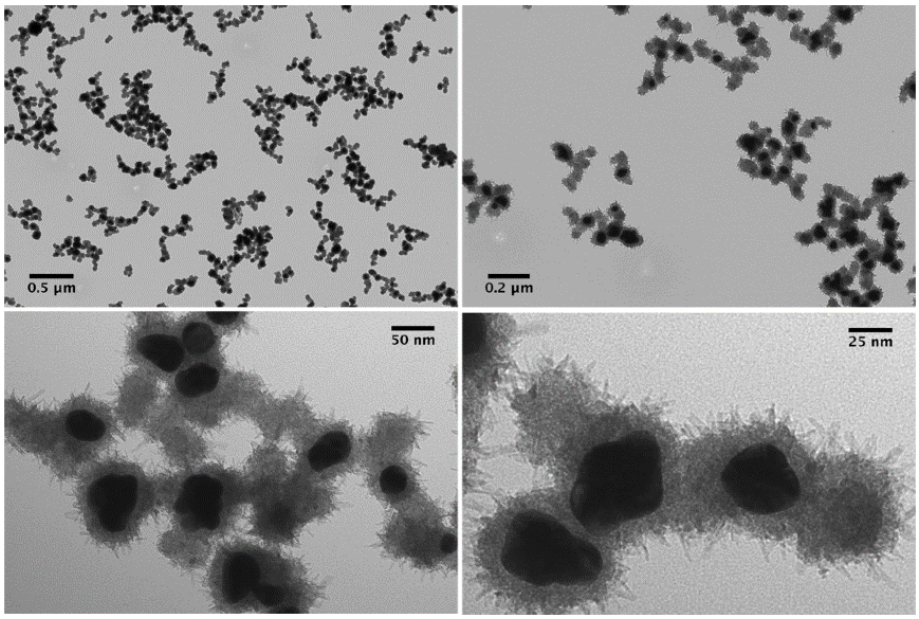

Figure 5.2. Representative TEM images of AuNPs obtained with an Au(III):Fe(II) molar ratio of 1:9 at 60 ºC.

In order to analysis the nature of the coating on the AuNPs surface (**Figure 5.2**), we performed FT-IR analysis of the AuNPs (Au(III):Fe(II) ratio of 1:9 and 60 ºC) and of another sample obtained under similar conditions but without Au(III). To this end, 30 mL of $FeSO_4$ aqueous solution was subjected to oxygen bubbling, and vigorous magnetic stirring for 2 h. A pale-yellow precipitate was observed. The solid (denoted as oxidation product) was purified by centrifugation and then analyzed by FT-IR.

The FT-IR spectra obtained from AuNPs and oxidation product showed similar FT-IR pattern. The presence of different Fe(II)/Fe(III) oxo-hydroxo sulfates could be easily identified in

both samples. Thus, a wide and intense band located at 3452 cm^{-1} could be assigned to ν(OH) stretching vibrations, peaks at 1647 and 1649 cm^{-1} to water bending vibrations,[242,243] and the bands between 1100 and 1200 cm^{-1} and peaks at 619 and 450 cm^{-1} to SO_4^{2-} stretching vibrations.[242–244] Finally Fe-O and Fe-OH signals were detected around 470 cm^{-1} and 703 cm^{-1}, respectively.[244–246]

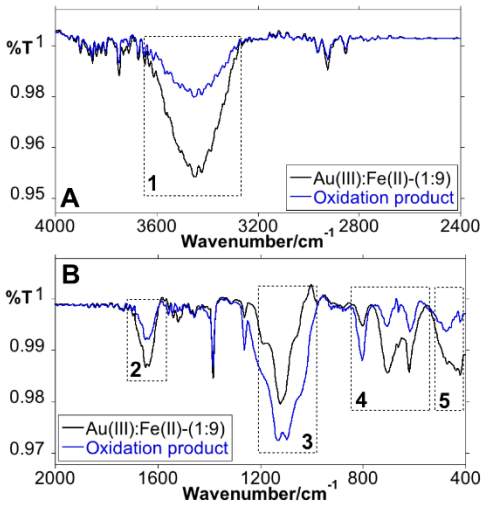

C

	Au:Fe(1:9) cm^{-1}/assignment	Oxidation product cm^{-1}/assignment
1	3452/ν(OH)	3452/ν(OH)
2	1647/ν(OH)	1649/ν(OH)
3	1122/ν(SO_4^{2-})	1130/ν(SO_4^{2-}) 1097/ν(SO_4^{2-})
4	802 703/ν(Fe-OH) 661/ν(Fe-O) 619/ν(SO_4^{2-})	803 703/ν(Fe-OH) 661/ν(Fe-O) 617/ν(SO_4^{2-})
5	470/ν(SO_4^{2-}) 455/ν(Fe-O)	476/ν(SO_4^{2-}) 451/ν(Fe-O)

Figure 5.3. (A and B) FT-IR spectra of AuNPs synthesized at 60 ºC for Au(III):Fe(II) molar ratio of 1:9 (black spectra) and the oxidation product (blue spectra) obtained in the absence of Au(III) under similar conditions. (C) Table showing the vibrational assignments.

Therefore, considering that the reduction of gold precursor is not stoichiometric, and the particles are poisoned by an iron oxo/hydroxo sulfate shell, we explored the possibility of adding a ligand (PSS) during AuNPs synthesis. PSS is generally recognized as a safe compound, noncytotoxic in nature and commonly used as a non-toxic peptizing agent in numerous commercial products.[247]

Moreover, it has been previously used as stabilizer in different metal NPs synthesis[248,249] or as secondary capping ligand for the detoxification of CTA-stabilized Au nanorods.[250] Similar experiments to those shown above at 60 ºC were performed but in the presence of PSS (0.5 mg/mL). To ensure that enough reducing agent is present in the reaction medium the Au(III):Fe(II) molar ratio of 1:3 was not used. Regardless the Au(III):Fe(II) molar ratio (1:6 or 1:9), the Fe(II) salt addition led a rapid color change (< 5 s) from light yellow to dark blue or purple depending on the conditions. **Figure 5.4A** shows the Vis-NIR extinction spectra of the Au dispersions obtained for Au(III):Fe(II) molar ratios of 1:6 and 1:9. In both cases a relatively broad LSPR band centered at around 580-600 nm was observed. The Au(III) reduction yield was analyzed by ICP-MS spectrometry (see experimental section for details) revealing an almost stoichiometric conversion to Au(0) (97.3% and 98.5% for Au(III):Fe(II) molar ratios of 1:6 and 1:9, respectively).

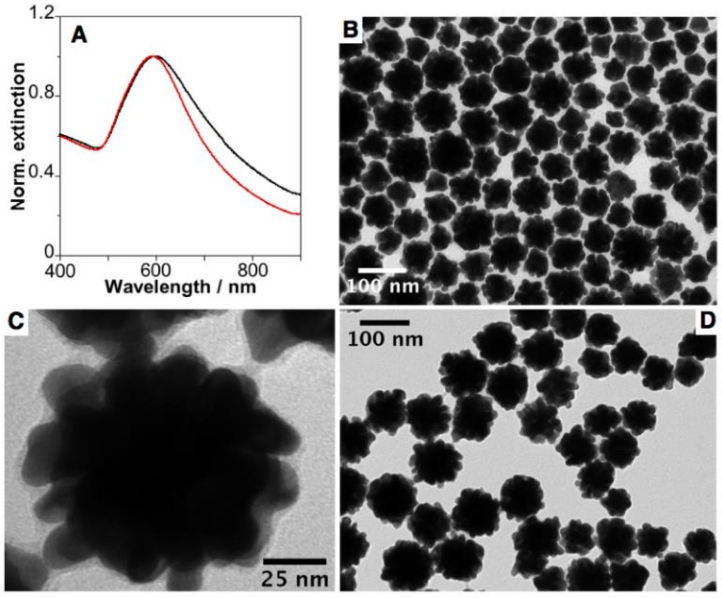

Figure 5.4. (A) Normalized extinction spectra of AuNPs synthesized at 60 ºC for Au(III):Fe(II) molar ratios of 1:6 (red spectrum) and 1:9 (black spectrum). [Au(III)] was 0.25 mM and [PSS] was 0.5 mg/mL. (B-D) Corresponding TEM images of AuNPs for Au(III):Fe(II) molar ratios of 1:6 (B) and 1:9 (C-D).

TEM characterization of both samples (**Figure 5.4**) shows that AuNPs present a quasi-spherical geometry, a remarkable surface roughness, resembling a raspberry-like nanoparticle and a relatively high polydispersity (> 10%). TEM analysis shows that the mean average size increased as the Au(III):Fe(II) ratio increases from 69.9 ± 22.4 nm for 1:6 to 87.9 ± 23.9 nm for 1:9 **(Figures 5.4 and 5.5)**. Contrary to that reported in the absence of PSS (see above) no coating

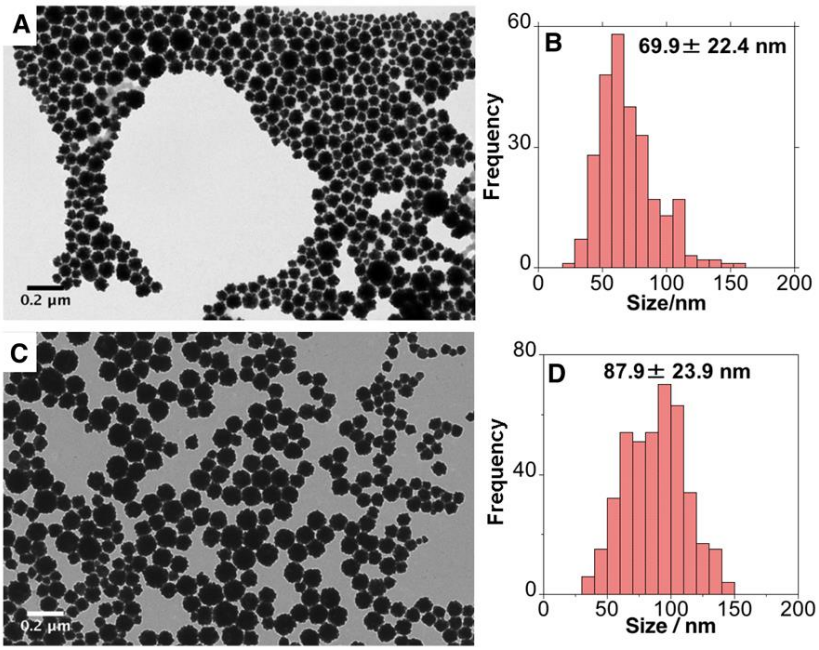

Figure 5.5. (A and C) Representative TEM images and (B and D) the corresponding size distribution histograms of AuNPs synthesized at 60 ºC for Au(III):Fe(III) molar ratios of (A and B) 1:6 and (C and D) 1:9. [Au(III)] was 0.25 mM and [PSS] was 0.5 mg/mL.

was observed on the Au surface. In fact the FTIR analysis did not show the presence of iron oxo/hydroxo sulfates most probably due to the iron complexation with PSS (**Figure 5.6**).[251]

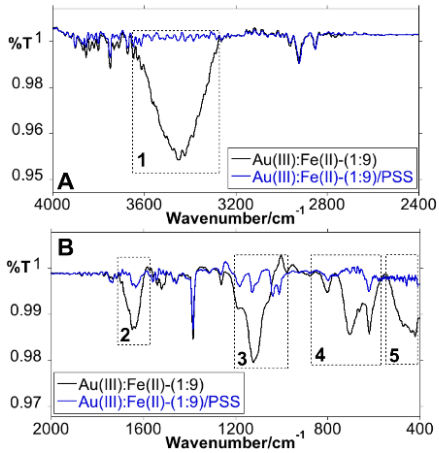

C	Au:Fe(1:9) cm^{-1}/assignment	Au:Fe(1:9)/PSS cm^{-1}/assignment
1	3452/ν(OH)	-
2	1647/ν(OH)	1631/ν(OH)
3	1122/ν(SO_4^{2-})	1182/ν(SO_3^-) 1126/ν(SO_3^-) 1038/ν(SO_3^-) 1011/ν (Aromatic ring in
4	802 703/ν(Fe-OH) 661/ν(Fe-O) 619/ν(SO_4^{2-})	798 - - 622/ν(SO_4^{2-})
5	470/ν(SO_4^{2-}) 455/ν(Fe-O)	- -

Figure 5.6. (A and B) FT-IR spectra of AuNPs synthesized at 60 ºC for Au(III):Fe(II) molar ratio of 1:9 (black spectra) in the absence (black spectrum) and in the presence (blue spectra) of PSS (0.5 mg/mL). (C) Table showing the vibrational assignment.

Nevertheless, it clearly revealed the presence of PSS on the NPs surface (**Figure 5.7)**.

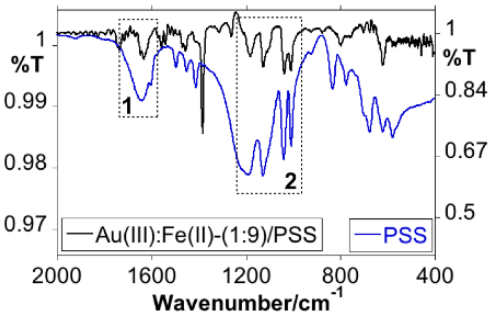

	Au(III):Fe(II)-(1:9)/PSS cm^{-1}/assignment	PSS cm^{-1}/assignment
1	1632/ν(OH)	1641/ν(OH)
2	1182/ν(SO_3^-) 1126/ν(SO_3^-) 1038/ν(SO_3^-) 1011/ν (Aromatic ring in plane)	1192/ν(SO_3^-) 1128/ν(SO_3^-) 1040/ν(SO_3^-) 1009/ν (Aromatic ring in plane)

Figure 5.7. (Left) FT-IR spectra of AuNPs synthesized at 60 ºC for Au(III):Fe(II) molar ratio of 1:9 in the presence of 0.5 mg/mL PSS (black spectra) and PSS (blue spectrum). (Right) Table showing the vibrational assignment.

The crystalline structure of the raspberry-like NPs was analyzed by High Resolution TEM (HRTEM). **Figures 5.8 and 5.9** show representative bright field images of two NPs displaying a rough nanostructured surface formed by numerous tips. The corresponding selected area electron diffraction (SAED) displays bright spots distributed in rings instead of ordered arrays (**Figure 5.8B**) demonstrating the polycrystalline character of these NPs. Moreover, HRTEM analysis of the nanoparticle tips reveals the presence of twinning planes in some of them (**Figure 5.8C-D**). The corresponding Fourier transform (**Figure 5.8E**) demonstrates the presence of two reciprocal nets, indicated in red and yellow in **Figure 5.8F**; showing a common twinning plane, and one of the nets being the result of the rotation of the other in a common axis by 70.43º (**Figure 5.10)**.

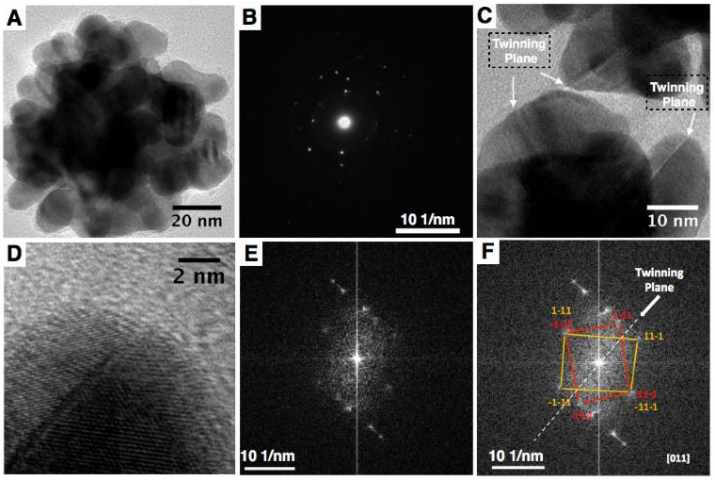

Figure 5.8. (A) Representative TEM image of AuNP showing its multi-tipped morphology. (B) Fourier Transform (FT) of the NP shown in (A). (C and D) HRTEM images showing the presence of twinning planes at the tips (indicated by arrows). (E and F) FT obtained from the tip shown in (D) demonstrating the presence of twinning planes in [011] twinning axis with rotation angle of 70.53º as shown in (F).

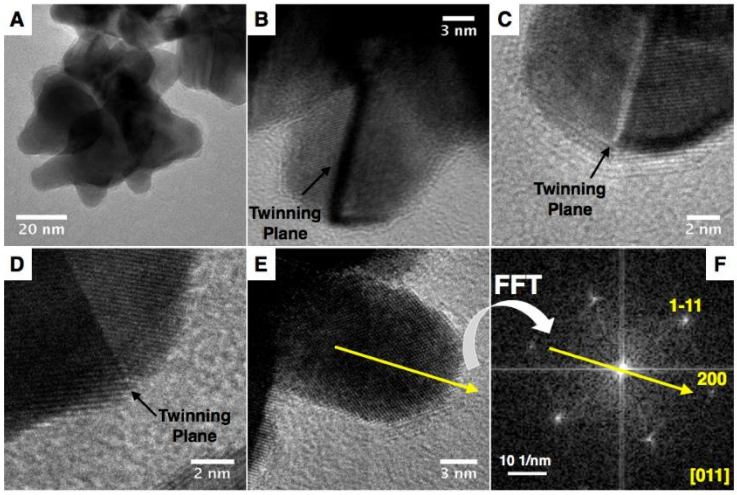

Figure 5.9. (A) Representative TEM image of AuNP showing its multi-tipped morphology. (B-E) HRTEM images showing the presence of twinning planes at the tips (indicated by arrows). (F) FFT obtained from the tip shown in (E) showing the growing direction of the tip.

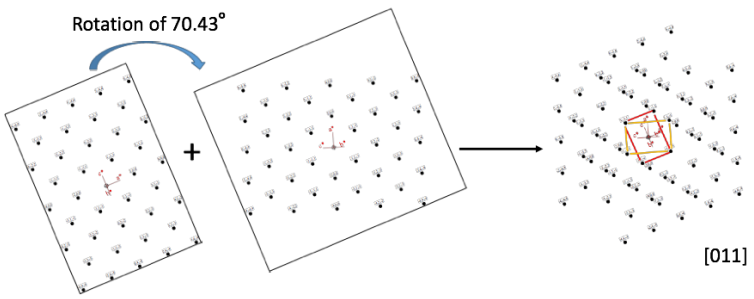

Figure 5.10. Simulation of the electron diffraction pattern using the [011] twinning axis with rotation angle of 70.43°.

To investigate the influence of PSS on the AuNPs synthesis, an experiment (Au(III):Fe(II) molar ratio 1:9) was performed using a higher amount of PSS (2 mg/mL). The results showed that the nanoparticle size (and size distribution) was barely affected (79.1 ± 20.9 nm for 2 mg/mL vs 87.9 ± 23.9 nm for 0.5 mg/mL) although remarkable changes were observed in the NPs morphology. Interestingly, a PSS concentration of 2 mg/mL led to AuNPs with a more faceted surface (**Figure 5.11**). This behavior suggests that PSS is not able to modulate the nucleation step during the NPs synthesis.

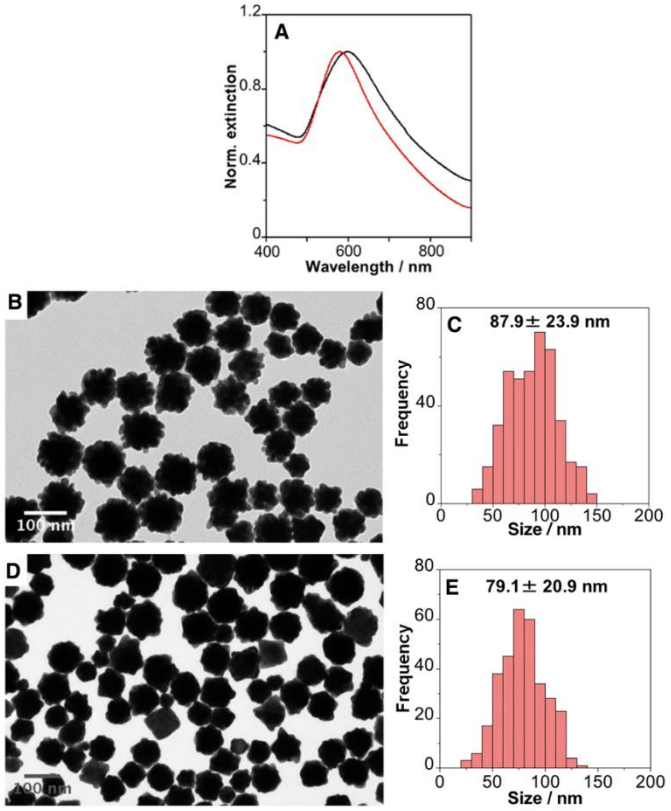

Figure 5.11. (A) Normalized extinction spectra of AuNPs synthesized at Au(III):Fe(II) ratio of 1:9 in the presence of 0.5 mg/mL PSS (red spectrum) and 2 mg/mL PSS (black spectrum). [Au(III)]= 0.25 mM and T= 60 ºC. (B and D) Representative TEM images and (C and E) the corresponding size distribution histograms of AuNPs synthesized in the presence of 0.5 mg/mL PSS (B and C) and 2 mg/mL PSS (D and E).

Additionally, taking into account that the redox potential might be strongly influenced by temperature the synthesis of AuNPs were performed at 100 ºC (Au(III):Fe(II) molar ratio 1:6 and [PSS] of 0.5 mg/mL). As shown in **Figure 5.12**, the increase in temperature gave rise to AuNPs with different optical features. The extinction spectrum exhibits a main LSPR band red-shifted (753 nm) which corresponds to a dipole mode and a less intense LSPR band located at higher energies assigned to a quadrupole mode (**Figure 5.12A**).[252] This indicates that an increase in the temperature leads to larger NPs. TEM analysis corroborated that, as shown in **Figure 5.12B** and

Figure 5.13C and D, AuNPs synthesized at 100 ºC are over 100 nm in diameter, although maintains similar raspberry morphology.

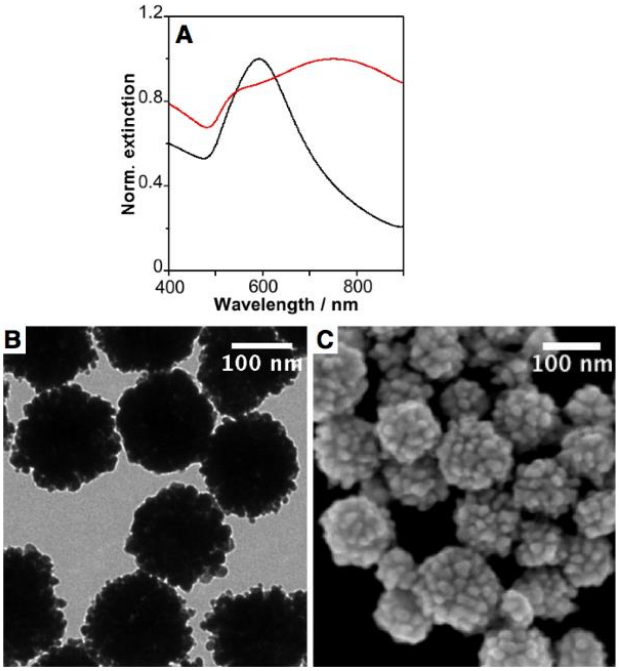

Figure 5.12. (A) Extinction spectra of AuNPs synthesized at 100 °C (red) and 60 ºC (black) for Au(III):Fe(II) molar ratio of 1:6. [Au(III)] was 0.25 mM and [PSS] was 0.5 mg/mL. (B and C) Corresponding TEM and SEM images of AuNPs obtained at 100°C and 60°C respectively.

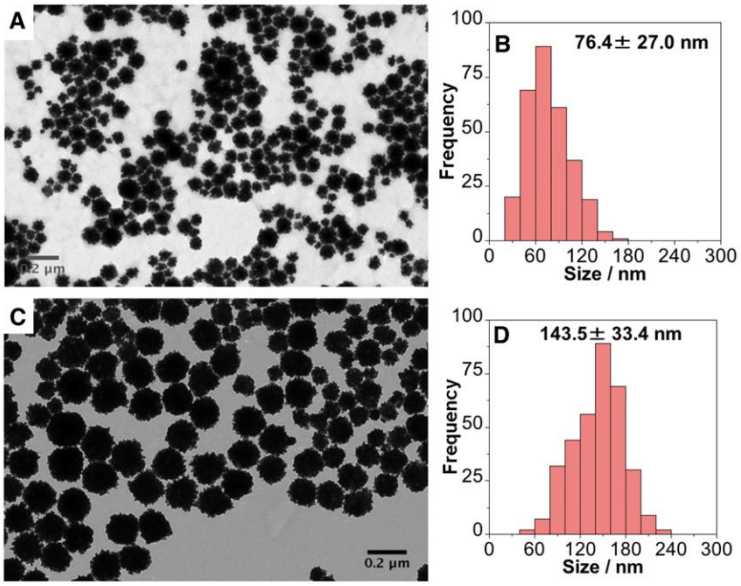

Figure 5.13. (A and C) Representative TEM images and (B and D) the corresponding size distribution histograms (right) of AuNPs synthesized with Au(III):Fe(III) ratio of 1:6 at 30 ºC (A and B) and 100 ºC (C and D). [Au(III)]= 0.25 mM and [PSS]= 0.5 mg/mL.

5.3.1. Modulation of Fe(III)/Fe(II) redox potential.

The formal potential of transition metals redox couples can be modulated through the complexation with a suitable ligand.[253,254] Particularly, it has been reported that the redox potential of the Fe(III)/Fe(II) couple is shifted to more negative values upon complexation with ions such as citrate, oxalate or ethylenediaminetetraacetic acid (EDTA).[254–256] Herein, we studied the effect of complexation of Fe(II) with citrate and chloride ions in the AuNPs synthesis. Thus, experiments in the presence of different citrate concentration (0.5, 0.75 and 1 mM) were performed at 40 ºC for Au(III):Fe(II) molar ratio of 1:3 and for concentrations of PSS and Au(III) of 0.5 mg/mL and 0.5 mM, respectively. After the addition of Au(III) salt over the Fe(II)/citrate/PSS solution, a colour change was rapidly observed (< 5 s) from yellow to red. It is remarkable that the presence of citrate in the reaction medium, regardless its concentration, led to complete reduction of the Au(III) to Au(0), as analyzed by ICP-MS spectrometry, at 40 ºC (data non shown). Moreover TEM analysis of the obtained AuNPs showed pseudo-spherical NPs with higher degree of uniformity in comparison with previous experiments performed in the absence of citrate (**Figure 5.14 and Figure 5.15**). Regarding the effect of the sodium citrate concentration, a decrease in the mean average size from 70.2 ± 18.5 nm to 45.4 ± 6.5 nm and 43.4 ± 9.1 nm is observed when it increases for 0.5 mM to 0.75 mM and 1 mM, respectively (**Figure 5.14 and Figure 5.15**). This seems to indicate that complexation of Fe(II) with citrate favours the nucleation vs growth, as expected. It should be noted that citrate is considered as a mild reducing agent. Thus, citrate ions are unable to reduce Au(III) to Au(0) at either 40 ºC or 60 ºC in the time scale of the reactions (typically less than 1 min, data non shown). Therefore, in the present case its role will be as stabilizer and also as modulator of the redox potential of the Fe(III)/Fe(II) pair. More precisely, the value of the reduction potential shifts to more negative values from 0.72 V for $Fe_2(SO_4)^-/Fe^{2+}$ to 0.38 V for Fe (III)-Cit/Fe(II)-Cit.[257]

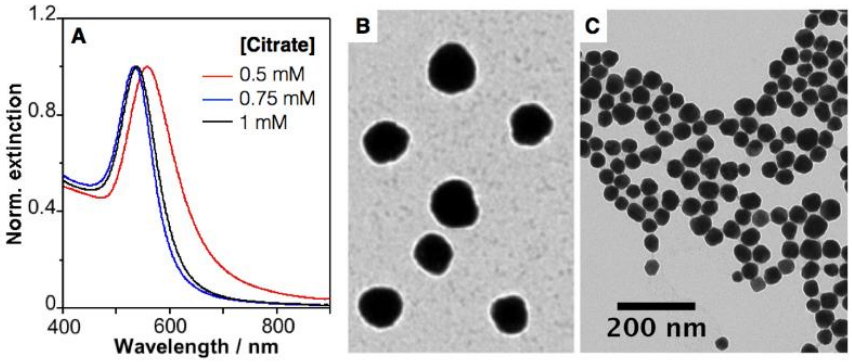

Figure 5.14. (A) Vis-NIR extinction spectra of AuNPs synthesized at 40 ºC for Au(III):Fe(II) molar ratio of 1:3 in the presence of different amounts of citrate (0.5 (red), 0.75 (blue) and 1 mM (black)). [Au(III)] was 0.5 mM, [PSS] was 0.5 mg/mL. (B and C) Corresponding TEM images of AuNPs synthesized in the presence of citrate 0.5 mM (B) and 0.75 mM (C). The scale bar is the same for both images.

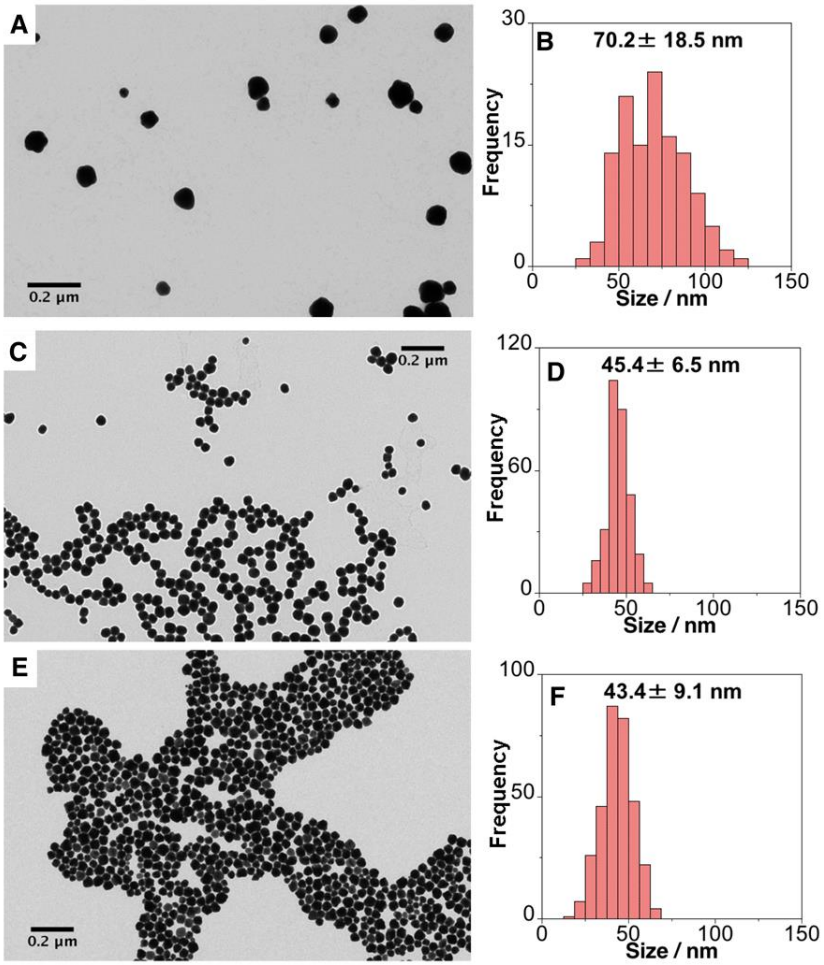

Figure 5.15. (A, C, E) Representative TEM images and (B, D, F) the corresponding size distribution histograms of AuNPs obtained in the presence of 0.50 mM (A and B) and 0.75 mM (C and D) and 1.0 mM (E and F) sodium citrate at 40 ºC. [Au(III)]= 0.5 mM, [Fe(II)]= 1.5 mM and [PSS]= 0.5 mg/mL.

We also analyzed the influence of $FeCl_2$ as a source of Fe(II) ions instead of $FeSO_4$ (**Figure 5.16**). The obtained AuNPs present a pseudo-spherical shape with a LSPR centred at ca. 558 nm and an average size of 59.4 nm. Thus, the AuNPs synthesized with $FeCl_2$ are smaller and more spherical than those obtained with $FeSO_4$ (**Figures 5.4 and 5.16**). The observed behavior seems to indicate that the presence of chloride ions induces a faster reduction of Au salt (more rapid nucleation step). This could be ascribed to a more negative value of the redox pair $FeCl_3/FeCl_2$ (0.54 V) versus $Fe(SO_4)_2^-/Fe^{2+}$ (0.72 V).[258] A similar effect was observed when mixing $FeSO_4$ as a source of Fe(II) ions by in the presence of NaCl (**Figure 5.17**), indicating the critical role of the chloride ion complexation with Fe(II) ions.

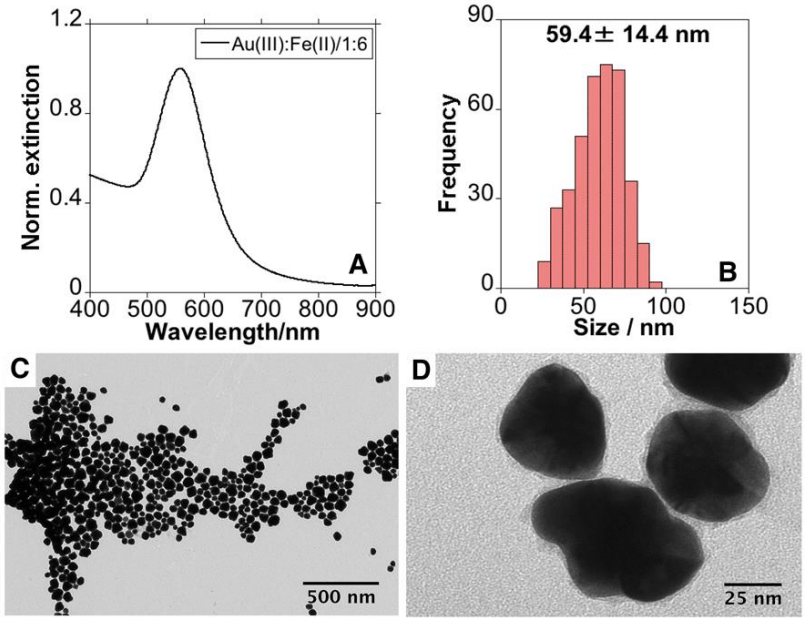

Figure 5.16. (A) Normalized extinction spectra of AuNPs synthesized using $FeCl_2.4H_2O$ at Au(III):Fe(II) ratio of 1:6 in the presence of 0.5 mg/mL PSS. [Au(III)]= 0.25 mM and T= 60 ºC. (B) Size distribution histograms and (C and D) representative TEM images.

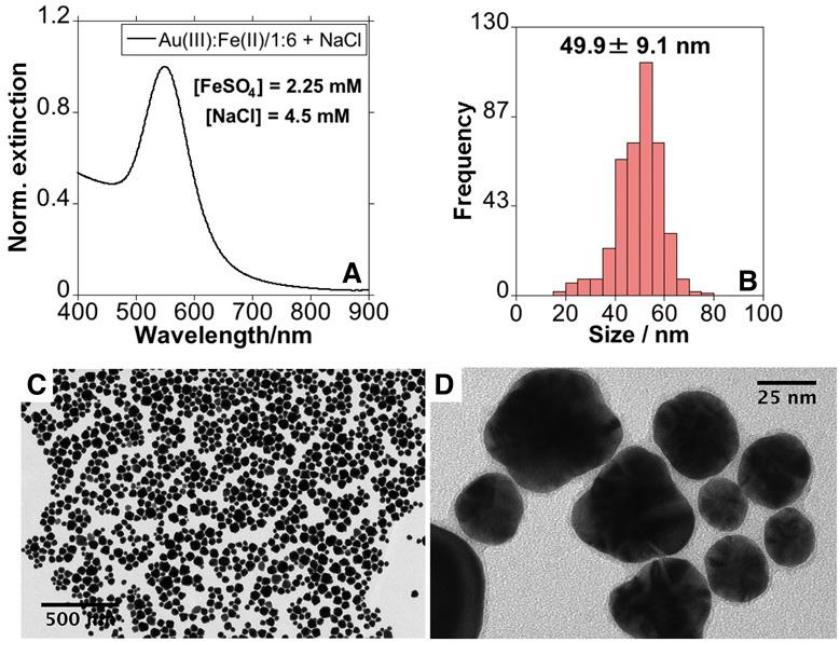

Figure 5.17. (A) Normalized extinction spectrum of AuNPs synthesized using $FeSO_4$ at Au(III):Fe(II) ratio of 1:6 in the presence of 0.5 mg/mL PSS. [Au(III)]= 0.25 mM and T= 60 ºC. (B) Size distribution histograms and (C and D) representative TEM images. The $FeSO_4$ solution was contaminated with NaCl prior to the injection in the reaction ($FeSO_4$/NaCl molar relation = 1/2).

5.3.2. Mechanism of AuNPs synthesis induce by Fe(II) ions.

In order to propose a plausible mechanism for the synthesis of AuNPs there are several points that should be taken into consideration:

i) By simply mixing Fe(II) ions and the gold salt precursor, that is in the absence of any capping agent or complexing agent, the reaction takes place but it is not stoichiometric (even at 60 ºC and Au(III):Fe(II) molar ratio of 1:9). Besides, the resulting AuNPs are coated by an iron oxo/hydroxo sulfate shell formed probably due to its low water solubility.

ii) The presence of PSS during the AuNPs synthesis leads to the Au(III) reduction yield of almost 100% and avoids the formation of such iron oxo/hydroxo sulfate shell, most probably due to the Fe(III) and/or Fe(II) complexation with the sulfonate moieties of PSS.[259]

iii) In the presence of PSS an increase in the reaction temperature from 30 ºC to 100 ºC (**Figure 5.8** and **Figure 5.13**) leads to AuNPs with larger sizes and rougher surfaces. This suggests that the particles formation takes place through a *particles-mediated growth process*.[260]

iv) The complexation of Fe(II) with citrate ions leads to a shift in the redox potential to more negative values.[261] Thus, the potential of the overall reaction will be more positive and the reaction can be considered as instantaneous (< 5 s). Furthermore, the overall size of the obtained spherical NPs decreases with the increase of citrate concentration. It indicates that the nucleation process dominates over the growth process which is in accordance to a classical growth method.[260] On the basis of these observations and attending to the structural characterization of the AuNPs synthesized in the presence of PSS but in the absence of citrate, which resemble to mesocrystalline NPs,[96] we suggest that the particles could be formed through a particle-mediated growth process. On the other hand, in the presence of PSS and citrate ions simultaneously the nucleation process dominates over the growth process in accordance to a classical growth method.[90,96,260,262]

5.3.3. SERS performance

SERS performance of AuNPs synthesized using Fe(II) ions has been analyzed using 4-nitrothiophenol (4-NTP) as model analyte. Thus, three representative samples were chosen depending on their synthetic procedure; in the presence of PSS (PSS60 and PSS100) and with PSS and citrate (Cit40) (where the numbers represent the mean average size) (**Table 5.1**). 4-NTP has been selected as model analyte since it exhibits high binding affinity for metal surfaces. The SERS efficiency of AuNPs was evaluated for three different laser lines: 633, 785 and 830 nm.

For doing that, SERS spectra of 10 µM 4-NTP were recorded after mixing with 0.5 mM AuNPs (in terms of gold metal).

Table 5.1. Summary of the experimental conditions for the synthesis of the different AuNPs employed in the SERS studies and the analytical enhancement factor (AEFs) estimated at 1332 cm^{-1} and 785 excitation.

Sample	[Au] / mM	Fe(II) / mM	PSS (mg/mL)	[Citrate] / mM	Temperature (°C)	Average size / nm	AEF (785 nm)
PSS60	0.25	2.25	2	--	60	60 ± 16	$3.4x10^4$
PSS100	0.25	2.25	0.5	--	60	94 ± 27	$1.0x10^4$
Cit40	0.50	1.5	0.5	1.0	40	44 ± 10	$9.3x10^1$

The extinction spectra of AuNPs before and after 4-NTP addition did not show any change which would be indicative of NPs aggregation. As shown in **Figure 5.18** for PSS60, regardless of the excitation laser line, 4-NTP is characterized by prominent SERS peaks assigned to C-H wagging (854 cm^{-1}), C-C-C in plane bending/C-S stretching (1108 cm^{-1}), CN stretching (1120 cm^{-1}), O-N=O symmetric stretching (1332 cm^{-1}) and C-C stretching/C-H in plane bending (1568 cm^{-1}).[263] Similar results were obtained for Cit40 and PSS100 (data not shown). **Figure 5.18C** shows the SERS intensity at 1332 cm^{-1} for the three AuNPs when excited with the three excitations laser lines. Interestingly, PSS60 shows the best performance and in all cases the 633 nm laser line leads to the best SERS efficiency.

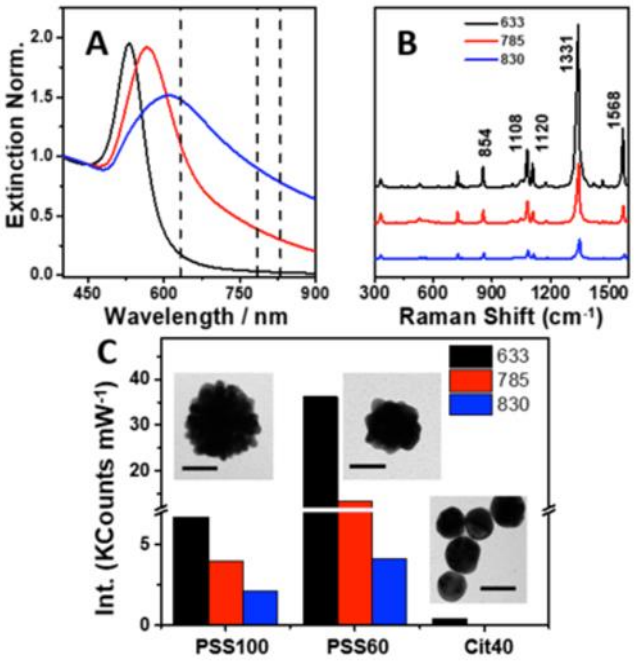

Figure 5.18. (A) Extinction spectra of the three selected AuNPs for SERS analysis; Cit40 (black), PSS60 (red) and PSS100 (blue). The dashed lines indicate the excitation laser line used. (B) SERS spectra of 4-NTP obtained with PSS60 for the three excitation lines as indicated. (C) SERS intensities corresponding to NO_2 symmetric stretching (1332 cm^{-1}) for the three AuNPs for the three excitation laser lines, as indicated. The insets show a representative TEM image of each particle. Scales bars represent 50 nm in all cases.

It should be noted that larger particles (PSS100) present a lower efficiency compare to PSS60 which could be ascribed to a stronger radiation damping resulting in a weaker local field enhancement.[264]

Therefore, PSS60 NPs were selected to determine the limit of detection (LOD) for 4-NTP. Thus, SERS spectra of 4-NTP at concentrations from 10^{-4} to 10^{-12} M were recorded in the presence of 0.5 mM AuNPs (**Figure 5.19A**). It should be noted that the SERS spectral background of the samples can be attributed to the surfactant PSS since they show similar profiles (**Figure 5.20**).[265]

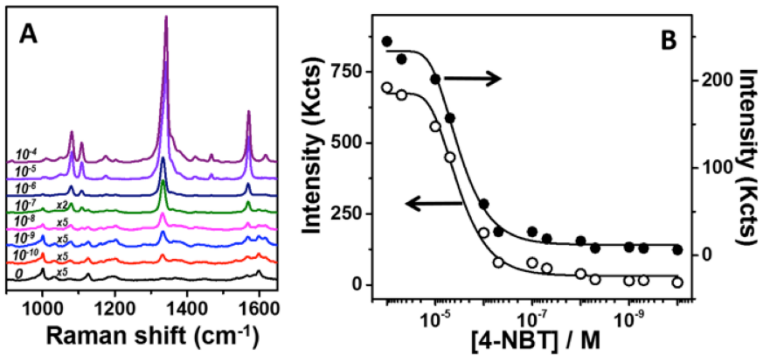

Figure 5.19. Limit of detection of 4-NTP determined using PSS60 (see text for details). (A) SERS spectra for different 4-NTP concentrations (as indicated in the labels) at constant concentrations of Au (0.5 mM) and 633 nm laser line. (B) Changes in the intensities of the NO_2 symmetrical stretching (1332 cm^{-1}, open circles) and CC stretching (1568 cm^{-1}, closed circles).

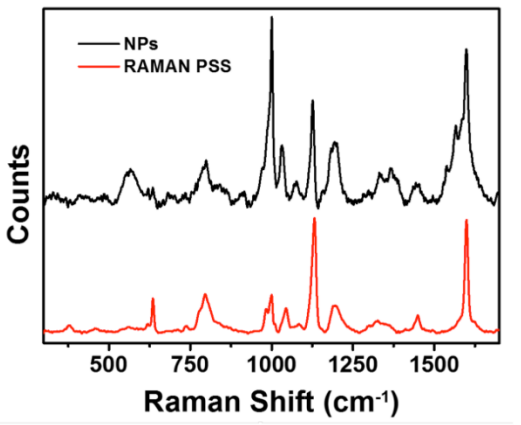

Vibrational assignment	**poly(sodium 4-styrenesulfonate) sodium salt (PSS) / cm^{-1}**
ν(CC) benzene ring stretching	1598
ν(SO_2) sulfonate	1190
ν(SO_2) sulfonate	1130
ν(CC) aromatic ring	1000
ν(CS) sulfonate	797

Figure 5.20. Raman and SERS spectra of PSS and Table showing the main vibrational assignment of PSS.

As observed in **Figures 5.19B and 5.21**, the SERS intensity decay of the signals at 1332 cm^{-1} (open circles) and at 1568 cm^{-1} (closed circles) indicates a LOD of 10^{-10} M. Additionally, **Figure 5.20** also shows a quantification regime from 10^{-4} to 10^{-10} M. This demonstrates that these particles provide high sensitivity for molecular sensing and quantitative information about the

amount of molecules attached to the particle surface and being comparable to that reported in the literature.[266]

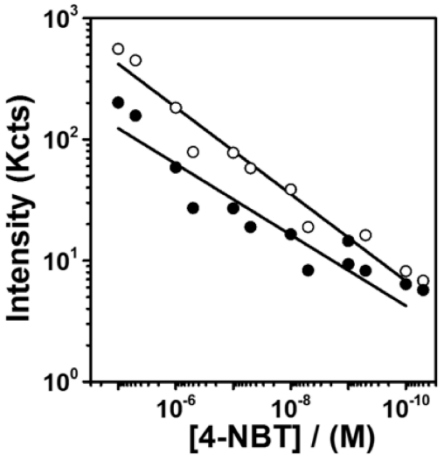

Figure 5.21. SERS intensity of 4-NTP signals at 1332 cm^{-1} (open circles) and 1568 cm^{-1} (closed circles) as a function of 4-NTP concentration. The lines are linear fits in the quantitative detection region. All measurements were performed at constant concentrations of Au (0.5 mM) and using 633 nm as excitation laser line.

Finally, SERS performance was also analyzed in terms of the analytical enhancement factor (AEF). This parameter can be defined as

$$AEF = \frac{I_{SERS}/c_{SERS}}{I_{RS}/c_{RS}}$$

where I_{SERS} is the SERS intensity for a selected mode of a given analyte, I_{RS} is the corresponding non-enhanced Raman intensity under identical experimental conditions and c_{SERS} and c_{RS} are the analyte concentrations in the SERS and Raman experiments, respectively.[267] The obtained AEFs range between 2.4×10^2, 3.9×10^3 and 2.1×10^4 for Cit40, PSS100 and PSS60, respectively and at 1332 cm^{-1} and 633 nm excitation. Generally, matching the excitation laser to the extinction maximum does not to yield the best SERS activity. Such increase is expected for situations in which the laser line is shifted to the red, compared to the extinction maximum.[268,269] We found the highest SERS activity for the 633 nm excitation laser and for the particles with average size of 60 nm and extinction maximum at ca. 570 nm. Summarizing, the highest SERS enhancement has been identified at 633 nm excitation for the sample PSS60 with AEF of 2.1×10^4. Additionally, the SERS performance was also determined for the 785 nm excitation showing similar AEF values (**Table 5.1**).

5.4. CONCLUSIONS

In summary, we have showed the possibility of using Fe(II) as reducing agent for the rapid synthesis of AuNPs. The method is based on the fast reduction of $AuCl_4^-$ ions by Fe(II) in the presence of PSS as surfactant. The obtained NPs are polycrystalline and present a rough nanostructured surface with a raspberry-like morphology. Besides, the morphology of the resulting AuNPs can be varied by shifting the redox potential of the Fe(III)/Fe(II) couple to more negative values through Fe(II) complexation with citrate ions. In fact the presence of citrate alters the nucleation step leading to pseudo-spherical AuNPs at room temperature in few seconds. In addition, SERS properties of AuNPs were investigated at three different excitation wavelengths yielding analytical enhancement factors between 2.4×10^2 to 3.4×10^4 and subnanomolar limit of detection (10^{-10} M) for 4-NTP. Thus AuNPs are expected to be excellent candidates for SERS based analytical and imaging applications.

CHAPTER

6

CONCLUSIONS AND PERSPECTIVES

As the main conclusions, the present doctoral thesis focuses on the development of gold and silver NPs. We emphasized on the analysis of the optoelectronic and chemical properties attending to changes in metal composition (gold or silver), surface functionalization, organic or inorganic, as well as in the structural modification of the shape of the NPs. The physicochemical properties that arise from the explored changes enable the application of colloidal metal systems in various scientific/technological fields, such as chemical sensing, antibacterial properties, imaging, catalysis or bio-chemistry among many others. Therefore, the control precise and controlled synthetic methodology in the liquid phase can be considered as a powerful tool providing NPs with specific size, shape and composition for the desired final application.

CHAPTER 2: In **Chapter 2**, The application of spherical AuNPs as vectors of toxic biomolecules at the cellular level was explored. We have successfully synthesized AuNPs using the Turkevich method and functionalized them through ligand exchange with a proteinaceous toxic *Eranthis hyemalis* lectin (EHL), a biomolecule which disrupts protein synthesis and subsequent cell death. This attractive molecule was extracted from the plant *Eranthis hyemalis* (Winter Aconite) appears as a solid candidate as an antibacterial and anticancer applications. Bioconjugates of biocompatible AuNPs with EHL protein was produced (AuNPs@EHL). Biological assays for the study of AuNPs@EHL effect on C. elegans were performed in collaboration with the Christ Church University of Canterbury, UK, showing that the activity of EHL activity was altered by conjugation, resulting in a lessened biological effect towards L1 stage worms. The lessened biological effect proves the possibility of using AuNPs as nanocarrier of

toxic EHL protein towards target cells, decreasing their adverse effect on non-target cells. Future research should focus on the investigation about the release of the toxic protein at cellular level and on development of stabilization methods using biocompatible capsules to protect the hybrid nanomaterial until the cell target is reached.

Functionalization of NPs can also be envisaged in order to produce interesting chemical properties in NPs, as in the case of the AgNPs and their toxicity, which can be increased by functionalization with molecular antibiotics. In our opinion, this method of functionalization using pre-formed AgNPs could induce an incomplete functionalization of NPs surface.

CHAPTER 3-1: In order to achieve a complete surface functionalization, in **Chapter 3**, a synthetic process to produce pseudo-spherical AgNPs and AuNPs using the antibiotic tetracycline (TC) as a reducing and stabilizing agent was developed. The elegant one-pot aqueous synthesis facilitates the production of Ag or AuNPs fully functionalized with an antibiotic (AgNPs@TC and AuNPs@TC). The antimicrobial studies towards Gram negative and Gram positive bacteria were performed and highlighted the synergistic effect of the antibiotic-association with the metallic surface of the AgNPs. This synergy increases the antibacterial effect on the sensitive and resistant tetracycline bacteria. Furthermore, our results confirmed that the size of the AgNPs@TC NPs influenced their antibacterial action. Future research can be implemented by studying more precisely the impact of the size of silver nanoparticles functionalized by tetracycline on the bactericidal action. In addition, it would be interesting to study the surface of nanoparticles determining the exact nature of the molecule. However available techniques are still limited to determine in a non-questionable way the nature of the molecule on the nanoparticles surface, especially when molecules were easily tautomerizable as is the case of tetracycline.

In addition to the increase observed on the toxicity of the AgNPs using organic functionalization, structural changes in the geometry of NPs have shown dramatic effects in the toxic properties of the resulting final nanomaterial.

CHAPTER 4: In **Chapter 4**, was exploring the change in the geometry of the NPs for antimicrobial studies. We have synthesized well defined Ag nanoplates with a different surface coating. This specific geometry for silver at the colloidal level presents a high sensitivity to oxidation processes due to the presence of (111) basal planes. The organic and inorganic functionalization explored allowing AgNTs application as an antibacterial agent against bacteria strains Gram negative and Gram positive. It is noteworthy that for the same bacterial strains explored before in Chapter 3, the AgNTs without the presence of additional antibiotic shows much higher antimicrobial properties. These critical results demonstrate how the rational selection of

the shape in silver NPs could overcome the synergistic effect produced by spherical shape and the tetracycline. The functionalization of nanoplates surface can be further developed by refining the chemical functionalization methods knowing that they are very sensitive to their environment. Furthermore, in the same way as in Chapter 3, the combination of antibiotics on the surface of the silver nanoplate could lead to an increase of the antibacterial synergistic effect and it might be interesting to study these materials in future antibacterial tests.

Besides, the optoelectronic properties of Ag or AuNPs are strongly dependent on their shape, size, composition, surface, and environment. These optical properties allow us the implementation of colloidal systems as chemical sensors or as SERS supports.

CHAPTER 3-2: Nevertheless, another important conclusion reported in **Chapter 3**, the AuNPs functionalized with Tetracycline, although they did not have a significant bactericidal effect, the colloid solution showed a remarkable application as a naked eye colorimetric sensor for Al(III) at the nanomolar range. Although the silver colloidal solution AgNPs@TC has the same sensing capability to detect Al(III), the higher limit of detection observed was probably due to the presence of Ag^{+} ions coming from the oxidation of the NPs, which could block the adsorption of Al(III). The future objective would be to synthesize and perfect this system being selective of the ions of interest even in the presence of other ions. In addition, the idea would be to adapt this system to environmental systems for extracting specific ions and thus clean the desired medium contaminated by the ions in question.

Therefore, the fascinating optical properties of these silver materials can be seen as strongly altered as a result of the instability of NPs to oxidation processes. Conversely, AuNPs are more prone to sensing or SERS applications as a consequence to not only to their interesting optical properties, but also their high stability to oxidation and degradation.

Relating to SERS applications of AuNPs, in the last decade, an enormous interest was noted for specific geometries where the concentration of the electromagnetic field can be increased in the corners or tips of the anisotropic NPs creating hot spots highly active in SERS.
This idea was explored in the case of the star or multi-tip shape AuNPs reported in Chapter 5. To date, an increasing number of synthetic processes of these nanostructures can be found in the literature. However, they usually involve multiple synthetic growth steps or processes with toxic reagents and contaminants.

CHAPTER 5: Conclusively, in **Chapter 5**, to achieve an advance in the SERS applications, a more environmentally friendly one-pot chemical approach to the synthesis of

AuNPs with different shapes, from pseudo-spherical to multi-tip or raspberry like NPs, was developed. The sustainable method runs in an aqueous medium and at low temperatures. The application of non-toxic reagents, considered to have low contaminant impact, $FeSO_4$, sodium citrate, and PSS, give rise to a newly developed process with higher advantages that should be contemplated. The SERS properties of AuNPs were investigated at three different excitation wavelengths, yielding an important analytical enhancement factors at the subnanomolar limit of detection for 4-NTP, a model analyte. Our results remark our multi-tips AuNPs excellence as exciting candidates for SERS applications based on analysis and imaging. For futures studies, one-pot synthesis of multi-tip AuNPs could be focus on the understanding of their formation in order to build a wide range of gold-based nanostructures efficient in SERS detection.

The experimental results summarized in this PhD thesis has highlighted the chemical and physical properties of gold and silver NPs. These properties could be incremented thanks to the functionalization of their surface by molecules of interest, and by the change of their shape — the implementation of new sustainable synthetic procedures allowed to control their properties and specific applications. The advanced synthetic techniques developed to allow us to further control of the size, shape and indirectly control of their optical and chemical properties. Moreover, the addition of different molecules to their surface makes them more specific and adaptable to sensing, SERS, antibacterial, and biomedical applications.

References

1. Kauffman, G. B. The role of gold in alchemy. Part I. *Gold Bull.* **18,** 31–44 (1985).
2. Louis, C. & Pluchery, O. *Gold Nanoparticles for Physics, Chemistry and Biology*. *Imperial College Press* (IMPERIAL COLLEGE PRESS, 2012).
3. Horikoshi, S. & Serpone, N. Introduction to Nanoparticles. *Microwaves Nanoparticle Synth.* 1–24 (2013).
4. Alexander, J. W. History of the Medical Use of Silver. *Surg. Infect. (Larchmt).* **10,** 289–292 (2009).
5. Kauffman, G. B. The role of gold in alchemy. Part II. *Gold Bull.* **18,** 69–78 (1985).
6. Schwartz, A. T. & Kauffman, G. B. Experiments in alchemy. Part I: Ancient arts. *J. Chem. Educ.* **53,** 136 (1976).
7. Möncke, D., Papageorgiou, M., Winterstein-Beckmann, A. & Zacharias, N. Roman glasses coloured by dissolved transition metal ions: redox-reactions, optical spectroscopy and ligand field theory. *J. Archaeol. Sci.* **46,** 23–36 (2014).
8. Freestone, I., Meeks, N., Sax, M. & Higgitt, C. The Lycurgus Cup — A Roman nanotechnology. *Gold Bull.* **40,** 270–277 (2007).
9. Brill, R. H. The Chemistry of the Lycurgus Cup. *Int. Congr. Glas. Comptes Rendus, II* **223,** 1–13 (1965).
10. Barber, D. J. & Fresstone, I. C. An investigation of the origin of the colour of the Lycurgus Cup by analytical transmission electron microscopy. *Archaeometry* **32,** 33–45 (1990).
11. Norton, S. A Brief History of Potable Gold. *Mol. Interv.* **8,** 120–123 (2008).
12. Hunt, L. B. The true story of Purple of Cassius. *Gold Bull.* **9,** 134–139 (1976).
13. Faraday, M. The Bakerian Lecture: Experimental Relations of Gold (and Other Metals) to Light. *Philos. Trans. R. Soc. London* **147,** 145–181 (1857).
14. Edwards, P. P. & Thomas, J. M. Gold in a Metallic Divided State—From Faraday to Present-Day Nanoscience. *Angew. Chemie Int. Ed.* **46,** 5480–5486 (2007).
15. Graham, T. Liquid Diffusion Applied to Analysis. *Philos. Trans. R. Soc. London* **151,** 183–224 (1861).
16. Mokrushin, S. G. Thomas Graham and the Definition of Colloids. *Nature* **195,** 861–861 (1962).
17. Zsigmondy, R. A. Nobel Lecture: Properties of Colloids. *Nobelprize.org. Nobel Media AB 2014* (1926).
18. Tyndall, J. On the Blue Colour of the Sky, the Polarization of Skylight, and on the Polarization of Light by Cloudy Matter Generally. *Proc. R. Soc. London* **17,** 223–233 (1868).
19. Maxwell, J. C. On physical lines of force. *Philos. Mag.* (1861).
20. Maxwell, J. C. A Treatise on Electricity and Magnetism. *Oxford Clarendon Press* (1873).
21. Horvath, H. Gustav Mie and the scattering and absorption of light by particles: Historic developments and basics. *J. Quant. Spectrosc. Radiat. Transf.* **110,** 787–799 (2009).

22. Mie, G. Beiträge zur Optik trüber Medien, speziell kolloidaler Metallösungen. *Ann. Phys.* **330,** 377–445 (1908).

23. Wood, R. W. LXIX. The absorption, dispersion, and surface-colour of selenium. *London, Edinburgh, Dublin Philos. Mag. J. Sci.* **3,** 607–622 (1902).

24. Moores, A. & Goettmann, F. The plasmon band in noble metal nanoparticles: an introduction to theory and applications. *New J. Chem.* **30,** 1121 (2006).

25. Ghosh, S. K. & Pal, T. Interparticle Coupling Effect on the Surface Plasmon Resonance of Gold Nanoparticles: From Theory to Applications. *Chem. Rev.* **107,** 4797–4862 (2007).

26. Sepúlveda, B., Angelomé, P. C., Lechuga, L. M. & Liz-Marzán, L. M. LSPR-based nanobiosensors. *Nano Today* **4,** 244–251 (2009).

27. Garcia, M. A. Surface plasmons in metallic nanoparticles: fundamentals and applications. *J. Phys. D. Appl. Phys.* **44,** 283001 (2011).

28. Bastús, N. G., Comenge, J. & Puntes, V. Kinetically Controlled Seeded Growth Synthesis of Citrate-Stabilized Gold Nanoparticles of up to 200 nm: Size Focusing versus Ostwald Ripening. *Langmuir* **27,** 11098–11105 (2011).

29. Bastús, N. G., Merkoçi, F., Piella, J. & Puntes, V. Synthesis of Highly Monodisperse Citrate-Stabilized Silver Nanoparticles of up to 200 nm: Kinetic Control and Catalytic Properties. *Chem. Mater.* **26,** 2836–2846 (2014).

30. Millstone, J. E., Hurst, S. J., Métraux, G. S., Cutler, J. I. & Mirkin, C. A. Colloidal Gold and Silver Triangular Nanoprisms. *Small* **5,** 646–664 (2009).

31. Hao, F., Nehl, C. L., Hafner, J. H. & Nordlander, P. Plasmon Resonances of a Gold Nanostar. *Nano Lett.* **7,** 729–732 (2007).

32. Garcia-Leis, A., Garcia-Ramos, J. V. & Sanchez-Cortes, S. Silver Nanostars with High SERS Performance. *J. Phys. Chem. C* **117,** 7791–7795 (2013).

33. Vo-Dinh, T. *et al.* SERS Nanosensors and Nanoreporters: Golden Opportunities in Biomedical Applications. *Wiley Interdiscip. Rev. Nanomedicine Nanobiotechnology* **7,** 17–33 (2015).

34. Graedel, T. E. Corrosion Mechanisms for Silver Exposed to the Atmosphere. *J. Electrochem. Soc.* **139,** 1963 (1992).

35. Levard, C., Hotze, E. M., Lowry, G. V. & Brown, G. E. Environmental Transformations of Silver Nanoparticles: Impact on Stability and Toxicity. *Environ. Sci. Technol.* **46,** 6900–6914 (2012).

36. Hainfeld, J. F., Slatkin, D. N., Focella, T. M. & Smilowitz, H. M. Gold nanoparticles: a new X-ray contrast agent. *Br. J. Radiol.* **79,** 248–253 (2006).

37. Nath, S. *et al.* Is Gold Really Softer than Silver? HSAB Principle Revisited. *J. Nanoparticle Res.* **8,** 111–116 (2006).

38. Neouze, M.-A. & Schubert, U. Surface Modification and Functionalization of Metal and Metal Oxide Nanoparticles by Organic Ligands. *Monatshefte für Chemie - Chem. Mon.* **139,** 183–195 (2008).

39. Pakiari, A. H. & Jamshidi, Z. Interaction of Amino Acids with Gold and Silver Clusters. *J. Phys. Chem. A* **111,** 4391–4396 (2007).

40. Austin, L. A., Mackey, M. A., Dreaden, E. C. & El-Sayed, M. A. The optical, photothermal, and facile surface chemical properties of gold and silver nanoparticles in

biodiagnostics, therapy, and drug delivery. *Arch. Toxicol.* **88,** 1391–1417 (2014).

41. Xiong, Y. & Lu, X. *Metallic Nanostructures: From Controlled Synthesis to Applications*. *Metallic Nanostructures: From Controlled Synthesis to Applications* (Springer International Publishing, 2015).

42. Xia, Y., Xiong, Y., Lim, B. & Skrabalak, S. E. Shape-Controlled Synthesis of Metal Nanocrystals: Simple Chemistry Meets Complex Physics? *Angew. Chemie Int. Ed.* **48,** 60–103 (2009).

43. Thanh, N. T. K., Maclean, N. & Mahiddine, S. Mechanisms of Nucleation and Growth of Nanoparticles in Solution. *Chem. Rev.* **114,** 7610–7630 (2014).

44. LaMer, V. K. & Dinegar, R. H. Theory, Production and Mechanism of Formation of Monodispersed Hydrosols. *J. Am. Chem. Soc.* **72,** 4847–4854 (1950).

45. Lin, M. Y. *et al.* Universal diffusion-limited colloid aggregation. *J. Phys. Condens. Matter* **2,** 3093–3113 (1990).

46. Watzky, M. A. & Finke, R. G. Nanocluster Size-Control and "Magic Number" Investigations. Experimental Tests of the "Living-Metal Polymer" Concept and of Mechanism-Based Size-Control Predictions Leading to the Syntheses of Iridium(0) Nanoclusters Centering about Four Sequential Magic. *Chem. Mater.* **9,** 3083–3095 (1997).

47. Liao, H.-G., Niu, K. & Zheng, H. Observation of growth of metal nanoparticles. *Chem. Commun.* **49,** 11720 (2013).

48. Ostwald, W. Über die vermeintliche Isomerie des roten und gelben Quecksilberoxyds und die Oberflächenspannung fester Körper. *Zeitschrift für Phys. Chemie* **34U,** (1900).

49. Lee, D., Park, S., Lee, J. & Hwang, N. A theoretical model for digestive ripening. *Acta Mater.* **55,** 5281–5288 (2007).

50. Lee, E. J. H., Ribeiro, C., Longo, E. & Leite, E. R. Oriented Attachment: An Effective Mechanism in the Formation of Anisotropic Nanocrystals. *J. Phys. Chem. B* **109,** 20842–20846 (2005).

51. José-Yacamán, M. *et al.* Surface Diffusion and Coalescence of Mobile Metal Nanoparticles. *J. Phys. Chem. B* **109,** 9703–9711 (2005).

52. Xia, Y., Gilroy, K. D., Peng, H.-C. & Xia, X. Seed-Mediated Growth of Colloidal Metal Nanocrystals. *Angew. Chemie Int. Ed.* **56,** 60–95 (2017).

53. Dykman, L. A. & Khlebtsov, N. G. Gold nanoparticles in biology and medicine: recent advances and prospects. *Acta Naturae* **3,** 34–55 (2011).

54. Rana, S., Bajaj, A., Mout, R. & Rotello, V. M. Monolayer coated gold nanoparticles for delivery applications. *Adv. Drug Deliv. Rev.* **64,** 200–216 (2012).

55. Aryal, S., Grailer, J. J., Pilla, S., Steeber, D. A. & Gong, S. Doxorubicin conjugated gold nanoparticles as water-soluble and pH-responsive anticancer drug nanocarriers. *J. Mater. Chem.* **19,** 7879 (2009).

56. Gibson, J. D., Khanal, B. P. & Zubarev, E. R. Paclitaxel-Functionalized Gold Nanoparticles. *J. Am. Chem. Soc.* **129,** 11653–11661 (2007).

57. Otsuka, H., Akiyama, Y., Nagasaki, Y. & Kataoka, K. Quantitative and Reversible Lectin-Induced Association of Gold Nanoparticles Modified with R -Lactosyl- ω -mercapto-poly (ethylene glycol). 8226–8230 (2018).

58. Turkevich, J., Stevenson, P. C. & Hillier, J. A study of the nucleation and growth processes

in the synthesis of colloidal gold. *Discuss. Faraday Soc.* **11,** 55 (1951).

59. Brewer, S. H., Glomm, W. R., Johnson, M. C., Knag, M. K. & Franzen, S. Probing BSA Binding to Citrate-Coated Gold Nanoparticles and Surfaces. *Langmuir* **21,** 9303–9307 (2005).

60. Pal, S., Tak, Y. K. & Song, J. M. Does the Antibacterial Activity of Silver Nanoparticles Depend on the Shape of the Nanoparticle? A Study of the Gram-Negative Bacterium Escherichia coli. *Appl. Environ. Microbiol.* **73,** 1712–1720 (2007).

61. Rai, M., Yadav, A. & Gade, A. Silver nanoparticles as a new generation of antimicrobials. *Biotechnol. Adv.* **27,** 76–83 (2009).

62. Feng, Q. L. *et al.* A mechanistic study of the antibacterial effect of silver ions on Escherichia coli and Staphylococcus aureus. *J. Biomed. Mater. Res.* **52,** 662–668 (2000).

63. Jung, W. K. *et al.* Antibacterial Activity and Mechanism of Action of the Silver Ion in Staphylococcus aureus and Escherichia coli. *Appl. Environ. Microbiol.* **74,** 2171–2178 (2008).

64. Reidy, B., Haase, A., Luch, A., Dawson, K. & Lynch, I. Mechanisms of Silver Nanoparticle Release, Transformation and Toxicity: A Critical Review of Current Knowledge and Recommendations for Future Studies and Applications. *Materials (Basel).* **6,** 2295–2350 (2013).

65. Xiu, Z., Zhang, Q., Puppala, H. L., Colvin, V. L. & Alvarez, P. J. J. Negligible Particle-Specific Antibacterial Activity of Silver Nanoparticles. *Nano Lett.* **12,** 4271–4275 (2012).

66. Chernousova, S. & Epple, M. Silver as Antibacterial Agent: Ion, Nanoparticle, and Metal. *Angew. Chemie Int. Ed.* **52,** 1636–1653 (2013).

67. Li, P., Li, J., Wu, C., Wu, Q. & Li, J. Synergistic antibacterial effects of β-lactam antibiotic combined with silver nanoparticles. *Nanotechnology* **16,** 1912–1917 (2005).

68. Shahverdi, A. R., Fakhimi, A., Shahverdi, H. R. & Minaian, S. Synthesis and effect of silver nanoparticles on the antibacterial activity of different antibiotics against Staphylococcus aureus and Escherichia coli. *Nanomedicine Nanotechnology, Biol. Med.* **3,** 168–171 (2007).

69. Rai, M. K., Deshmukh, S. D., Ingle, A. P. & Gade, A. K. Silver nanoparticles: the powerful nanoweapon against multidrug-resistant bacteria. *J. Appl. Microbiol.* **112,** 841–852 (2012).

70. Vitanov, T. & Popov, A. Adsorption of SO_4^{2-} on growth steps of (111) and (100) faces of silver single crystals. *J. Electroanal. Chem. Interfacial Electrochem.* **159,** 437–441 (1983).

71. Morones, J. R. *et al.* The bactericidal effect of silver nanoparticles. *Nanotechnology* **16,** 2346–2353 (2005).

72. Xue, C., Chen, X., Hurst, S. J. & Mirkin, C. A. Self-Assembled Monolayer Mediated Silica Coating of Silver Triangular Nanoprisms. *Adv. Mater.* **19,** 4071–4074 (2007).

73. Vilela, D., González, M. C. & Escarpa, A. Sensing colorimetric approaches based on gold and silver nanoparticles aggregation: Chemical creativity behind the assay. A review. *Anal. Chim. Acta* **751,** 24–43 (2012).

74. Lee, K.-S. & El-Sayed, M. A. Gold and Silver Nanoparticles in Sensing and Imaging: Sensitivity of Plasmon Response to Size, Shape, and Metal Composition. *J. Phys. Chem. B* **110,** 19220–19225 (2006).

75. Caro, C., M., P., Klippstein, R., Pozo, D. & P., A. Silver Nanoparticles: Sensing and

Imaging Applications. in *Silver Nanoparticles* (InTech, 2010).

76. Fernández-Lodeiro, J., Núñez, C., Oliveira, E., Capelo, J. L. & Lodeiro, C. 1D chain fluorescein-functionalized gold and silver nanoparticles as new optical mercury chemosensor in aqueous media. *J. Nanoparticle Res.* **15,** 1828 (2013).

77. Daniel, M. & Astruc, D. Gold nanoparticles: assembly, supramolecular chemistry, quantum-size-related properties, and applications toward biology, catalysis, and nanotechnology. *Chem. Rev.* **104,** 293–346 (2004).

78. Mirkin, C. A., Letsinger, R. L., Mucic, R. C. & Storhoff, J. J. A DNA-based method for rationally assembling nanoparticles into macroscopic materials. *Nature* **382,** 607–609 (1996).

79. Elghanian, R., Storhoff, J. J., Mucic, R. C., Letsinger, R. L. & Mirkin, C. A. Selective Colorimetric Detection of Polynucleotides Based on the Distance-Dependent Optical Properties of Gold Nanoparticles. *Science (80-.).* **277,** 1078–1081 (1997).

80. Storhoff, J. J., Elghanian, R., Mucic, R. C., Mirkin, C. A. & Letsinger, R. L. One-Pot Colorimetric Differentiation of Polynucleotides with Single Base Imperfections Using Gold Nanoparticle Probes. *J. Am. Chem. Soc.* **120,** 1959–1964 (1998).

81. Alivisatos, A. P. *et al.* Organization of 'nanocrystal molecules' using DNA. *Nature* **382,** 609–611 (1996).

82. Clark, R. J. H. & Stewart, B. The resonance raman effect—Review of the theory and of applications in inorganic chemistry. in *Inorganic Chemistry and Spectroscopy* 1–80 (1979).

83. Raman, C. V. & Krishnan, K. S. A New Type of Secondary Radiation. *Nature* **121,** 501–502 (1928).

84. Miller, F. A. & Kauffman, G. B. C. V. Raman and the discovery of the Raman effect. *J. Chem. Educ.* **66,** 795 (1989).

85. Kneipp, K., Kneipp, H., Itzkan, I., Dasari, R. R. & Feld, M. S. Ultrasensitive Chemical Analysis by Raman Spectroscopy. *Chem. Rev.* **99,** 2957–2976 (1999).

86. Fleischmann, M., Hendra, P. J. & McQuillan, A. J. Raman spectra of pyridine adsorbed at a silver electrode. *Chem. Phys. Lett.* **26,** 163–166 (1974).

87. Herrera, G., Padilla, A. & Hernandez-Rivera, S. Surface Enhanced Raman Scattering (SERS) Studies of Gold and Silver Nanoparticles Prepared by Laser Ablation. *Nanomaterials* **3,** 158–172 (2013).

88. Hong, S. & Li, X. Optimal Size of Gold Nanoparticles for Surface-Enhanced Raman Spectroscopy under Different Conditions. *J. Nanomater.* **2013,** 1–9 (2013).

89. Tian, F., Bonnier, F., Casey, A., Shanahan, A. E. & Byrne, H. J. Surface enhanced Raman scattering with gold nanoparticles: effect of particle shape. *Anal. Methods* **6,** 9116–9123 (2014).

90. Liu, Z. *et al.* Gold mesoparticles with precisely controlled surface topographies for single-particle surface-enhanced Raman spectroscopy. *J. Mater. Chem. C* **1,** 5567 (2013).

91. Chirico, G., Borzenkov, M. & Pallavicini, P. *Gold Nanostars: Synthesis, Properties and Biomedical Application*. *Springer International Publishing* (Springer International Publishing, 2015).

92. Kereselidze, Z., Romero, V. H., Peralta, X. G. & Santamaria, F. Gold Nanostar Synthesis with a Silver Seed Mediated Growth Method. *J. Vis. Exp.* 2–6 (2012).

93. Verma, M. S., Chen, P. Z., Jones, L. & Gu, F. X. Branching and size of CTAB-coated gold nanostars control the colorimetric detection of bacteria. *RSC Adv.* **4,** 10660–10668 (2014).

94. Luo, Y., Ji, X., Zhuang, J. & Yang, W. Controlled formation of gold nanoflowers by reduction of tetrachloroauric acid with thermally treated glucose in alkaline solution. *Colloids Surfaces A Physicochem. Eng. Asp.* **463,** 28–36 (2014).

95. Li, N., Zhao, P. & Astruc, D. Anisotropic Gold Nanoparticles: Synthesis, Properties, Applications, and Toxicity. *Angew. Chemie Int. Ed.* **53,** 1756–1789 (2014).

96. Fang, J. *et al.* Gold Mesostructures with Tailored Surface Topography and Their Self-Assembly Arrays for Surface-Enhanced Raman Spectroscopy. *Nano Lett.* **10,** 5006–5013 (2010).

97. Allen J. Bard, Joseph Jordan, R. P. *Standard potentials in aqueous solutions*. (1985).

98. Peumans, W. J. & Van Damme, E. Lectins as Plant Defense Proteins. *Plant Physiol.* **109,** 347–352 (1995).

99. Sharon, N. History of lectins: from hemagglutinins to biological recognition molecules. *Glycobiology* **14,** 53R–62R (2004).

100. Schubert, M. *et al.* Plasticity of the β-Trefoil Protein Fold in the Recognition and Control of Invertebrate Predators and Parasites by a Fungal Defence System. *PLoS Pathog.* **8,** e1002706 (2012).

101. Delatorre, P. *et al.* Structure of a lectin from Canavalia gladiata seeds: new structural insights for old molecules. *BMC Struct. Biol.* **7,** 52 (2007).

102. Kumar, M. A. *et al.* Characterization of the lectin from the bulbs of *Eranthis hyemalis* (winter aconite) as an inhibitor of protein synthesis. *J. Biol. Chem.* **268,** 25176–83 (1993).

103. Rao, K. V. *et al.* Expression of snowdrop lectin (GNA) in transgenic rice plants confers resistance to rice brown planthopper. *Plant J.* **15,** 469–477 (1998).

104. Peumans, W. J., Hao, Q. & Van Damme, E. J. Ribosome-inactivating proteins from plants: more than RNA N-glycosidases? *FASEB J.* **15,** 1493–506 (2001).

105. Vurro, M. & Gresse, J. *Novel Biotechnologies for Biocontrol Agent Enhancement and Management*. (Springer Netherlands, 2007).

106. Cammue, B. P., Peeters, B. & Peumans, W. J. Isolation and partial characterization of an N -acetylgalactosamine-specific lectin from winter-aconite (*Eranthis hyemalis*) root tubers. *Biochem. J.* **227,** 949–955 (1985).

107. George, O., Solscheid, C., Bertolo, E., Fell, J. C. & Lisgarten, D. Extraction and purification of the lectin found in the tubers of *Eranthis hyemalis* (winter aconite). *J. Integr. OMICS* **1,** 268–271 (2011).

108. McConnell, M. T. Structural and Functional Characterisation of *Eranthis Hyemalis* Lectin: A Type II Ribosome Inactivating Protein. (2017).

109. Ju, T., Otto, V. I. & Cummings, R. D. The Tn Antigen-Structural Simplicity and Biological Complexity. *Angew. Chemie Int. Ed.* **50,** 1770–1791 (2011).

110. Voss, C., Eyol, E., Frank, M., von der Lieth, C.-W. & Berger, M. R. Identification and characterization of riproximin, a new type II ribosome-inactivating protein with antineoplastic activity from Ximenia americana. *FASEB J.* **20,** 1194–1196 (2006).

111. Bayer, H. *et al.* Evaluation of Riproximin Binding Properties Reveals a Novel Mechanism for Cellular Targeting. *J. Biol. Chem.* **287,** 35873–35886 (2012).

112. Adwan, H., Bayer, H., Pervaiz, A., Sagini, M. & Berger, M. R. Riproximin is a recently discovered type II ribosome inactivating protein with potential for treating cancer. *Biotechnol. Adv.* **32,** 1077–1090 (2014).

113. McConnell, M.-T., Lisgarten, D. R., Byrne, L. J., Harvey, S. C. & Bertolo, E. Winter Aconite (*Eranthis hyemalis*) Lectin as a cytotoxic effector in the lifecycle of *Caenorhabditis elegans*. *PeerJ* **3,** e1206 (2015).

114. Boyd, W. A., Smith, M. V. & Freedman, J. H. *Caenorhabditis elegans* as a Model in Developmental Toxicology. in *Methods in Molecular Biology* (eds. Harris, C. & Hansen, J. M.) **889,** 15–24 (Humana Press, 2012).

115. Corsi, A. K., Wightman, B. & Chalfie, M. A Transparent Window into Biology: A Primer on *Caenorhabditis elegans*. *Genetics* **200,** 387–407 (2015).

116. Cassada, R. C. & Russell, R. L. The dauerlarva, a post-embryonic developmental variant of the nematode *Caenorhabditis elegans*. *Dev. Biol.* **46,** 326–342 (1975).

117. Dreaden, E. C., Alkilany, A. M., Huang, X., Murphy, C. J. & El-Sayed, M. A. The golden age: gold nanoparticles for biomedicine. *Chem. Soc. Rev.* **41,** 2740–2779 (2012).

118. Hutter, E. & Maysinger, D. Gold nanoparticles and quantum dots for bioimaging. *Microsc. Res. Tech.* **74,** 592–604 (2011).

119. Dykman, L. & Khlebtsov, N. Gold nanoparticles in biomedical applications: recent advances and perspectives. *Chem. Soc. Rev.* **41,** 2256–2282 (2012).

120. Libralato, G. *et al.* Toxicity Effects of Functionalized Quantum Dots, Gold and Polystyrene Nanoparticles on Target Aquatic Biological Models: A Review. *Molecules* **22,** 1439 (2017).

121. Ahmad, M. Z. *et al.* Nanometric gold in cancer nanotechnology: current status and future prospect. *J. Pharm. Pharmacol.* **65,** 634–651 (2013).

122. Rasband, W. S. ImageJ, U.S. National Institutes of Health, Bethesda, MA, USA. *Available online: https://imagej.nih.gov/ij/ (accessed on 3 August 2018)* 1–2

123. Kimling, J. *et al.* Turkevich Method for Gold Nanoparticle Synthesis Revisited. *J. Phys. Chem. B* **110,** 15700–15707 (2006).

124. Stiernagle, T. *Maintenance of C. elegans. In WormBook (The C. elegans Research Community)* **2,** (2006).

125. Shang, L., Wang, Y., Jiang, J. & Dong, S. pH-Dependent Protein Conformational Changes in Albumin:Gold Nanoparticle Bioconjugates: A Spectroscopic Study. *Langmuir* **23,** 2714–2721 (2007).

126. Lacerda, S. H. D. P. *et al.* Interaction of Gold Nanoparticles with Common Human Blood Proteins. *ACS Nano* **4,** 365–379 (2010).

127. Tsai, D.-H. *et al.* Adsorption and Conformation of Serum Albumin Protein on Gold Nanoparticles Investigated Using Dimensional Measurements and in Situ Spectroscopic Methods. *Langmuir* **27,** 2464–2477 (2011).

128. Wang, Y. & Ni, Y. Combination of UV–vis spectroscopy and chemometrics to understand protein–nanomaterial conjugate: A case study on human serum albumin and gold nanoparticles. *Talanta* **119,** 320–330 (2014).

129. Hendel, T. *et al.* In Situ Determination of Colloidal Gold Concentrations with UV–Vis Spectroscopy: Limitations and Perspectives. *Anal. Chem.* **86,** 11115–11124 (2014).

130. Scarabelli, L., Grzelczak, M. & Liz-Marzán, L. M. Tuning Gold Nanorod Synthesis through Prereduction with Salicylic Acid. *Chem. Mater.* **25,** 4232–4238 (2013).

131. Scarabelli, L., Sánchez-Iglesias, A., Pérez-Juste, J. & Liz-Marzán, L. M. A "Tips and Tricks" Practical Guide to the Synthesis of Gold Nanorods. *J. Phys. Chem. Lett.* **6,** 4270–4279 (2015).

132. Rodríguez-Fernández, J., Pérez-Juste, J., Mulvaney, P. & Liz-Marzán, L. M. Spatially-Directed Oxidation of Gold Nanoparticles by Au(III)−CTAB Complexes. *J. Phys. Chem. B* **109,** 14257–14261 (2005).

133. Wang, P. *et al.* Interaction of gold nanoparticles with proteins and cells. *Sci. Technol. Adv. Mater.* **16,** 034610 (2015).

134. Thobhani, S. *et al.* Bioconjugation and characterisation of gold colloid-labelled proteins. *J. Immunol. Methods* **356,** 60–69 (2010).

135. Anderson, G. L., Boyd, W. A. & Williams, P. L. Assessment of sublethal endpoints for toxicity testing with the nematode *Caenorhabditis elegans*. *Environ. Toxicol. Chem.* **20,** 833–838 (2001).

136. Dhawan, R., Dusenbery, D. B. & Williams, P. L. Comparison of lethality, reproduction, and behavior as toxicological endpoints in the nematode *Caenorhabditis elegans*. *J. Toxicol. Environ. Heal. Part A* **58,** 451–462 (1999).

137. Leung, M. C. K. *et al. Caenorhabditis elegans*: An Emerging Model in Biomedical and Environmental Toxicology. *Toxicol. Sci.* **106,** 5–28 (2008).

138. Khare, P. *et al.* Adverse Effects of TiO2 and ZnO Nanoparticles in Soil Nematode, *Caenorhabditis elegans*. *J. Biomed. Nanotechnol.* **7,** 116–117 (2011).

139. Wang, H., Wick, R. L. & Xing, B. Toxicity of nanoparticulate and bulk ZnO, Al2O3 and TiO2 to the nematode *Caenorhabditis elegans*. *Environ. Pollut.* **157,** 1171–1177 (2009).

140. Stutz, K., Kaech, A., Aebi, M., Künzler, M. & Hengartner, M. O. Disruption of the C. elegans Intestinal Brush Border by the Fungal Lectin CCL2 Phenocopies Dietary Lectin Toxicity in Mammals. *PLoS One* **10,** e0129381 (2015).

141. Sharma, V. K., Yngard, R. A. & Lin, Y. Silver nanoparticles: Green synthesis and their antimicrobial activities. *Adv. Colloid Interface Sci.* **145,** 83–96 (2009).

142. Giljohann, D. A. *et al.* Gold Nanoparticles for Biology and Medicine. *Angew. Chemie Int. Ed.* **49,** 3280–3294 (2010).

143. McFarland, A. D. & Van Duyne, R. P. Single Silver Nanoparticles as Real-Time Optical Sensors with Zeptomole Sensitivity. *Nano Lett.* **3,** 1057–1062 (2003).

144. Saha, K., Agasti, S. S., Kim, C., Li, X. & Rotello, V. M. Gold Nanoparticles in Chemical and Biological Sensing. *Chem. Rev.* **112,** 2739–2779 (2012).

145. Jiang, Z.-J., Liu, C.-Y. & Sun, L.-W. Catalytic Properties of Silver Nanoparticles Supported on Silica Spheres. *J. Phys. Chem. B* **109,** 1730–1735 (2005).

146. Willets, K. A. & Van Duyne, R. P. Localized Surface Plasmon Resonance Spectroscopy and Sensing. *Annu. Rev. Phys. Chem.* **58,** 267–297 (2007).

147. Jain, P. K., Huang, X., El-Sayed, I. H. & El-Sayed, M. A. Noble Metals on the Nanoscale: Optical and Photothermal Properties and Some Applications in Imaging, Sensing, Biology, and Medicine. *Acc. Chem. Res.* **41,** 1578–1586 (2008).

148. Mout, R., Moyano, D. F., Rana, S. & Rotello, V. M. Surface functionalization of

nanoparticles for nanomedicine. *Chem. Soc. Rev.* **41,** 2539 (2012).

149. Kora, A. J. & Rastogi, L. Enhancement of Antibacterial Activity of Capped Silver Nanoparticles in Combination with Antibiotics, on Model Gram-Negative and Gram-Positive Bacteria. *Bioinorg. Chem. Appl.* **2013,** 1–7 (2013).

150. Khurana, C., Vala, A. K., Andhariya, N., Pandey, O. P. & Chudasama, B. Antibacterial activities of silver nanoparticles and antibiotic-adsorbed silver nanoparticles against biorecycling microbes. *Environ. Sci. Process. Impacts* **16,** 2191 (2014).

151. Shen, L., Chen, J., Li, N., He, P. & Li, Z. Rapid colorimetric sensing of tetracycline antibiotics with in situ growth of gold nanoparticles. *Anal. Chim. Acta* **839,** 83–90 (2014).

152. Fernández-Lodeiro, A. *et al.* Polyamine Ligand-Mediated Self-Assembly of Gold and Silver Nanoparticles into Chainlike Structures in Aqueous Solution: Towards New Nanostructured Chemosensors. *ChemistryOpen* **2,** 200–207 (2013).

153. Santos, C. I. M. *et al.* Corrole and Corrole Functionalized Silica Nanoparticles as New Metal Ion Chemosensors: A Case of Silver Satellite Nanoparticles Formation. *Inorg. Chem.* **52,** 8564–8572 (2013).

154. Fernández-Lodeiro, J. *et al.* New-coated fluorescent silver nanoparticles with a fluorescein thiol esther derivative: fluorescent enhancement upon interaction with heavy metal ions. *J. Nanoparticle Res.* **16,** 2315 (2014).

155. Araújo, J. E. *et al.* Novel nanocomposites based on a strawberry-like gold- coated magnetite (Fe@Au) for protein separation in multiple myeloma serum samples. *Nano Res.* **8,** 1189–1198 (2015).

156. Ruiz, E. *et al.* qnr, aac(6′)-Ib-cr and qepA genes in Escherichia coli and Klebsiella spp.: genetic environments and plasmid and chromosomal location. *J. Antimicrob. Chemother.* **67,** 886–897 (2012).

157. Lozano, C. *et al.* Empyema caused by MRSA ST398 with Atypical Resistance Profile, Spain. *Emerg. Infect. Dis.* **17,** 138–140 (2011).

158. Andrews, J. M. Determination of minimum inhibitory concentrations. *J. Antimicrob. Chemother.* **49,** 1049–1049 (2002).

159. Nishimura, S., Mott, D., Takagaki, A., Maenosono, S. & Ebitani, K. Role of base in the formation of silver nanoparticles synthesized using sodium acrylate as a dual reducing and encapsulating agent. *Phys. Chem. Chem. Phys.* **13,** 9335 (2011).

160. Romanov, V. *et al.* Binding Energies of the Silver Ion to Alcohols and Amides: A Theoretical and Experimental Study. *J. Phys. Chem. A* **112,** 10912–10920 (2008).

161. Amat, A., Fantacci, S., De Angelis, F., Carlotti, B. & Elisei, F. DFT/TDDFT investigation of the stepwise deprotonation in tetracycline: pKa assignment and UV–vis spectroscopy. *Theor. Chem. Acc.* **131,** 1218 (2012).

162. Ghosh, P., Han, G., De, M., Kim, C. K. & Rotello, V. M. Gold nanoparticles in delivery applications. *Adv. Drug Deliv. Rev.* **60,** 1307–1315 (2008).

163. Eisenhart, A. E. & M., D. N. Thermostability Determination of Antibiotics at High Temperatures by Liquid Chromatography-Mass Spectrometry. in *Proceedings of The National Conference On Undergraduate Research (NCUR)* (2012).

164. Hassani, M., Lázaro, R., Pérez, C., Condón, S. & Pagán, R. Thermostability of Oxytetracycline, Tetracycline, and Doxycycline at Ultrahigh Temperatures. *J. Agric. Food Chem.* **56,** 2676–2680 (2008).

165. Oka, H. *et al.* Photodecomposition products of tetracycline in aqueous solution. *J. Agric. Food Chem.* **37,** 226–231 (1989).

166. Chopra, I. & Roberts, M. Tetracycline antibiotics: mode of action, applications, molecular biology, and epidemiology of bacterial resistance. *Microbiol. Mol. Biol. Rev.* **65,** 232–60 ; second page, table of contents (2001).

167. Nelson, M., Hillen, W. & Greenwald, R. A. *Tetracyclines in Biology, Chemistry and Medicine*. (Birkhäuser Basel, 2001).

168. Agnihotri, S., Mukherji, S. & Mukherji, S. Size-controlled silver nanoparticles synthesized over the range 5–100 nm using the same protocol and their antibacterial efficacy. *RSC Adv.* **4,** 3974–3983 (2014).

169. Minogue, T. D. *et al.* Complete Genome Assembly of Escherichia coli ATCC 25922, a Serotype O6 Reference Strain. *Genome Announc.* **2,** e00969-14 (2014).

170. Brown, A. N. *et al.* Nanoparticles Functionalized with Ampicillin Destroy Multiple-Antibiotic-Resistant Isolates of Pseudomonas aeruginosa and Enterobacter aerogenes and Methicillin-Resistant Staphylococcus aureus. *Appl. Environ. Microbiol.* **78,** 2768–2774 (2012).

171. Wang, L. *et al.* Functionalised nanoparticles complexed with antibiotic efficiently kill MRSA and other bacteria. *Chem. Commun.* **50,** 12030–12033 (2014).

172. Li, X. *et al.* Functional Gold Nanoparticles as Potent Antimicrobial Agents against Multi-Drug-Resistant Bacteria. *ACS Nano* **8,** 10682–10686 (2014).

173. Fayaz, A. M. *et al.* Biogenic synthesis of silver nanoparticles and their synergistic effect with antibiotics: a study against gram-positive and gram-negative bacteria. *Nanomedicine Nanotechnology, Biol. Med.* **6,** 103–109 (2010).

174. Kelly, K. L., Coronado, E., Zhao, L. L. & Schatz, G. C. The Optical Properties of Metal Nanoparticles: The Influence of Size, Shape, and Dielectric Environment. *J. Phys. Chem. B* **107,** 668–677 (2003).

175. Wei, H. Plasmonic Silver Nanoparticles for Energy and Optoelectronic Applications. in *Advances in Nanomaterials and Nanostructures* **52,** 171–184 (2011).

176. Köhler, J. M., Abahmane, L., Wagner, J., Albert, J. & Mayer, G. Preparation of metal nanoparticles with varied composition for catalytical applications in microreactors. *Chem. Eng. Sci.* **63,** 5048–5055 (2008).

177. Pastoriza-Santos, I. & Liz-Marzán, L. M. Colloidal silver nanoplates. State of the art and future challenges. *J. Mater. Chem.* **18,** 1724 (2008).

178. Kundu, S. *et al.* Shape-selective catalysis and surface enhanced Raman scattering studies using Ag nanocubes, nanospheres and aggregated anisotropic nanostructures. *J. Colloid Interface Sci.* **498,** 248–262 (2017).

179. Sadeghi, B. *et al.* Comparison of the anti-bacterial activity on the nanosilver shapes: Nanoparticles, nanorods and nanoplates. *Adv. Powder Technol.* **23,** 22–26 (2012).

180. Le Beulze, A. *et al.* New Insights into the Side-Face Structure, Growth Aspects, and Reactivity of Ag n Nanoprisms. *Langmuir* **30,** 1424–1434 (2014).

181. Van Dong, P., Ha, C. H., Binh, L. T. & Kasbohm, J. Chemical synthesis and antibacterial activity of novel-shaped silver nanoparticles. *Int. Nano Lett.* **2,** 9 (2012).

182. Abbaszadegan, A. *et al.* The Effect of Charge at the Surface of Silver Nanoparticles on Antimicrobial Activity against Gram-Positive and Gram-Negative Bacteria: A

Preliminary Study. *J. Nanomater.* **2015,** 1–8 (2015).

183. Yang, X. *et al.* Mechanism of Silver Nanoparticle Toxicity Is Dependent on Dissolved Silver and Surface Coating in *Caenorhabditis elegans*. *Environ. Sci. Technol.* **46,** 1119–1127 (2012).

184. Le, Y., Hou, P., Wang, J. & Chen, J.-F. Controlled release active antimicrobial corrosion coatings with Ag/SiO2 core–shell nanoparticles. *Mater. Chem. Phys.* **120,** 351–355 (2010).

185. Liong, M., France, B., Bradley, K. A. & Zink, J. I. Antimicrobial Activity of Silver Nanocrystals Encapsulated in Mesoporous Silica Nanoparticles. *Adv. Mater.* **21,** 1684–1689 (2009).

186. Nuti, S. *et al.* Engineered Nanostructured Materials for Ofloxacin Delivery. *Front. Chem.* **6,** 1–14 (2018).

187. Jiang, X., Zeng, Q. & Yu, A. Thiol-Frozen Shape Evolution of Triangular Silver Nanoplates. *Langmuir* **23,** 2218–2223 (2007).

188. Mulvaney, P., Giersig, M., Ung, T. & Liz-Marzán, L. M. Direct observation of chemical reactions in silica-coated gold and silver nanoparticles. *Adv. Mater.* **9,** 570–575 (1997).

189. Lecloux, A. J. *et al.* Study of the texture of monodisperse silica sphere samples in the nanometer size range. *Colloids and Surfaces* **19,** 359–374 (1986).

190. van Blaaderen, A. & Vrij, A. Synthesis and Characterization of Monodisperse Colloidal Organo-silica Spheres. *J. Colloid Interface Sci.* **156,** 1–18 (1993).

191. Bruce, I. J. & Sen, T. Surface Modification of Magnetic Nanoparticles with Alkoxysilanes and Their Application in Magnetic Bioseparations. *Langmuir* **21,** 7029–7035 (2005).

192. Brandon, M. P., Ledwith, D. M. & Kelly, J. M. Preparation of saline-stable, silica-coated triangular silver nanoplates of use for optical sensing. *J. Colloid Interface Sci.* **415,** 77–84 (2014).

193. Métraux, G. S. & Mirkin, C. A. Rapid Thermal Synthesis of Silver Nanoprisms with Chemically Tailorable Thickness. *Adv. Mater.* **17,** 412–415 (2005).

194. Yu, H. *et al.* Thermal Synthesis of Silver Nanoplates Revisited: A Modified Photochemical Process. *ACS Nano* **8,** 10252–10261 (2014).

195. Zhang, Q., Li, N., Goebl, J., Lu, Z. & Yin, Y. A Systematic Study of the Synthesis of Silver Nanoplates: Is Citrate a "Magic" Reagent? *J. Am. Chem. Soc.* **133,** 18931–18939 (2011).

196. Link, S. & El-Sayed, M. A. Spectral Properties and Relaxation Dynamics of Surface Plasmon Electronic Oscillations in Gold and Silver Nanodots and Nanorods. *J. Phys. Chem. B* **103,** 8410–8426 (1999).

197. Szunerits, S. & Boukherroub, R. Sensing using localised surface plasmon resonance sensors. *Chem. Commun.* **48,** 8999 (2012).

198. Morales-Cruz, A. L., Tremont, R., Martínez, R., Romañach, R. & Cabrera, C. R. Atomic force measurements of 16-mercaptohexadecanoic acid and its salt with CH_3, OH, and $CONHCH_3$ functionalized self-assembled monolayers. *Appl. Surf. Sci.* **241,** 371–383 (2005).

199. Gupta, R. K., Srinivasan, M. P. & Dharmarajan, R. Synthesis of 16-Mercaptohexadecanoic acid capped gold nanoparticles and their immobilization on a substrate. *Mater. Lett.* **67,** 315–319 (2012).

200. Johnson, S. R., Evans, S. D. & Brydson, R. Influence of a Terminal Functionality on the Physical Properties of Surfactant-Stabilized Gold Nanoparticles. *Langmuir* **14,** 6639–6647 (1998).

201. Azarshin, S., Moghadasi, J. & A Aboosadi, Z. Surface functionalization of silica nanoparticles to improve the performance of water flooding in oil wet reservoirs. *Energy Explor. Exploit.* **35,** 685–697 (2017).

202. Rahman, I. A., Vejayakumaran, P., Sipaut, C. S., Ismail, J. & Chee, C. K. Size-dependent physicochemical and optical properties of silica nanoparticles. *Mater. Chem. Phys.* **114,** 328–332 (2009).

203. Sakthisabarimoorthi, A., Dhas, S. A. M. B. & Jose, M. Fabrication and nonlinear optical investigations of SiO_2@Ag core-shell nanoparticles. *Mater. Sci. Semicond. Process.* **71,** 69–75 (2017).

204. Jacobasch, H.-J. Characterization of solid surfaces by electrokinetic measurements. *Prog. Org. Coatings* **17,** 115–133 (1989).

205. Jesionowski, T. Influence of aminosilane surface modification and dyes adsorption on zeta potential of spherical silica particles formed in emulsion system. *Colloids Surfaces A Physicochem. Eng. Asp.* **222,** 87–94 (2003).

206. Bahadur, N. M. *et al.* Fast and facile synthesis of silica coated silver nanoparticles by microwave irradiation. *J. Colloid Interface Sci.* **355,** 312–320 (2011).

207. Akhavan, O. & Ghaderi, E. Bactericidal effects of Ag nanoparticles immobilized on surface of SiO2 thin film with high concentration. *Curr. Appl. Phys.* **9,** 1381–1385 (2009).

208. Ifuku, S. *et al.* Facile preparation of silver nanoparticles immobilized on chitin nanofiber surfaces to endow antifungal activities. *Carbohydr. Polym.* **117,** 813–817 (2015).

209. Liga, M. V., Bryant, E. L., Colvin, V. L. & Li, Q. Virus inactivation by silver doped titanium dioxide nanoparticles for drinking water treatment. *Water Res.* **45,** 535–544 (2011).

210. Bryaskova, R., Pencheva, D., Nikolov, S. & Kantardjiev, T. Synthesis and comparative study on the antimicrobial activity of hybrid materials based on silver nanoparticles (AgNps) stabilized by polyvinylpyrrolidone (PVP). *J. Chem. Biol.* **4,** 185–191 (2011).

211. Djafari, J. *et al.* New Synthesis of Gold- and Silver-Based Nano-Tetracycline Composites. *ChemistryOpen* **5,** 206–212 (2016).

212. D'Agostino, A. *et al.* Bulk Surfaces Coated with Triangular Silver Nanoplates: Antibacterial Action Based on Silver Release and Photo-Thermal Effect. *Nanomaterials* **7,** 7 (2017).

213. Lu, W., Yao, K., Wang, J. & Yuan, J. Ionic liquids–water interfacial preparation of triangular Ag nanoplates and their shape-dependent antibacterial activity. *J. Colloid Interface Sci.* **437,** 35–41 (2015).

214. Marta, B. *et al.* Pluronic-coated silver nanoprisms: Synthesis, characterization and their antibacterial activity. *Colloids Surfaces A Physicochem. Eng. Asp.* **441,** 77–83 (2014).

215. Tang, B. *et al.* Colorful and Antibacterial Silk Fiber from Anisotropic Silver Nanoparticles. *Ind. Eng. Chem. Res.* **52,** 4556–4563 (2013).

216. Tanvir, F., Yaqub, A., Tanvir, S. & Anderson, W. Poly-L-arginine Coated Silver Nanoprisms and Their Anti-Bacterial Properties. *Nanomaterials* **7,** 296 (2017).

217. Bagwe, R. P., Hilliard, L. R. & Tan, W. Surface Modification of Silica Nanoparticles to

Reduce Aggregation and Nonspecific Binding. *Langmuir* **22,** 4357–4362 (2006).

218. Xu, K., Wang, J. X., Kang, X. L. & Chen, J. F. Fabrication of antibacterial monodispersed Ag-SiO_2 core-shell nanoparticles with high concentration. *Mater. Lett.* **63,** 31–33 (2009).

219. Wong, K. K. Y. & Liu, X. Silver nanoparticles—the real "silver bullet" in clinical medicine? *Medchemcomm* **1,** 125 (2010).

220. Mijnendonckx, K., Leys, N., Mahillon, J., Silver, S. & Van Houdt, R. Antimicrobial silver: uses, toxicity and potential for resistance. *BioMetals* **26,** 609–621 (2013).

221. Durán, N. *et al.* Silver nanoparticles: A new view on mechanistic aspects on antimicrobial activity. *Nanomedicine Nanotechnology, Biol. Med.* **12,** 789–799 (2016).

222. Bodelón, G. *et al.* Detection and imaging of quorum sensing in Pseudomonas aeruginosa biofilm communities by surface-enhanced resonance Raman scattering. *Nat. Mater.* **15,** 1203–1211 (2016).

223. Bodelón, G., Costas, C., Pérez-Juste, J., Pastoriza-Santos, I. & Liz-Marzán, L. M. Gold nanoparticles for regulation of cell function and behavior. *Nano Today* **13,** 40–60 (2017).

224. Notarianni, M. *et al.* Plasmonic effect of gold nanoparticles in organic solar cells. *Sol. Energy* **106,** 23–37 (2014).

225. Priecel, P., Adekunle Salami, H., Padilla, R. H., Zhong, Z. & Lopez-Sanchez, J. A. Anisotropic gold nanoparticles: Preparation and applications in catalysis. *Chinese J. Catal.* **37,** 1619–1650 (2016).

226. Grzelczak, M., Pérez-Juste, J., Mulvaney, P. & Liz-Marzán, L. M. Shape control in gold nanoparticle synthesis. *Chem. Soc. Rev.* **37,** 1783 (2008).

227. Chen, J., Herricks, T. & Xia, Y. Polyol Synthesis of Platinum Nanostructures: Control of Morphology through the Manipulation of Reduction Kinetics. *Angew. Chemie Int. Ed.* **44,** 2589–2592 (2005).

228. Mourdikoudis, S. & Liz-Marzán, L. M. Oleylamine in Nanoparticle Synthesis. *Chem. Mater.* **25,** 1465–1476 (2013).

229. Koczkur, K. M., Mourdikoudis, S., Polavarapu, L. & Skrabalak, S. E. Polyvinylpyrrolidone (PVP) in nanoparticle synthesis. *Dalt. Trans.* **44,** 17883–17905 (2015).

230. Shankar, S. S. *et al.* Biological synthesis of triangular gold nanoprisms. *Nat. Mater.* **3,** 482–488 (2004).

231. Anshup *et al.* Growth of Gold Nanoparticles in Human Cells. *Langmuir* **21,** 11562–11567 (2005).

232. Johnston, C. W. *et al.* Gold biomineralization by a metallophore from a gold-associated microbe. *Nat. Chem. Biol.* **9,** 241–243 (2013).

233. Engelbrekt, C. *et al.* Green synthesis of gold nanoparticles with starch–glucose and application in bioelectrochemistry. *J. Mater. Chem.* **19,** 7839 (2009).

234. Leng, Y. *et al.* Protein-directed synthesis of highly monodispersed, spherical gold nanoparticles and their applications in multidimensional sensing. *Sci. Rep.* **6,** 28900 (2016).

235. Kunoh, T. *et al.* Green Synthesis of Gold Nanoparticles Coupled with Nucleic Acid Oxidation. *ACS Sustain. Chem. Eng.* **6,** 364–373 (2018).

236. Mannar, V. & Gallego, E. B. Forging Effective Strategies to Combat Iron Deficiency Iron

Fortification : Country Level Experiences and Lessons Learned 1 , 2 , 3. *J. Nutr.* **1,** 856–858 (2002).

237. Leach, B. *Applied Industrial Catalysis; Leach, B., Ed.; Elsevier,*. **18,** (198AD).

238. Morris, D. F. C. & Khan, M. A. Application of solvent extraction to the refining of precious metals—III Purification of gold. *Talanta* **15,** 1301–1305 (1968).

239. Schneider, C. A., Rasband, W. S. & Eliceiri, K. W. NIH Image to ImageJ: 25 years of image analysis. *Nat. Methods* **9,** 671–675 (2012).

240. Moodley, K. G. & Nicol, M. J. Kinetics of reduction of gold(III) by platinum(II) and iron(III) in aqueous chloride solutions. *J. Chem. Soc. Dalt. Trans.* **26,** 993 (1977).

241. Gómez-Graña, S. *et al.* Au@Ag nanoparticles: Halides stabilize {100} facets. *J. Phys. Chem. Lett.* **4,** 2209–2216 (2013).

242. Lazaroff, N., Sigal, W. & Wasserman, A. Iron Oxidation and Precipitation of Ferric Hydroxysulfates by Resting Thiobacillus ferrooxidans Cells. *Appl. Environ. Microbiol.* **43,** 924–38 (1982).

243. Bishop, J. L. The visible and infrared spectral properties of jarosite and alunite. *Am. Mineral.* **90,** 1100–1107 (2005).

244. Liu, H., Li, P., Lu, B., Wei, Y. & Sun, Y. Transformation of ferrihydrite in the presence or absence of trace Fe(II): The effect of preparation procedures of ferrihydrite. *J. Solid State Chem.* **182,** 1767–1771 (2009).

245. Deki, S. *et al.* Preparation and characterization of iron oxyhydroxide and iron oxide thin films by liquid-phase deposition. *J. Mater. Chem.* **7,** 1769–1772 (1997).

246. Pinto, P. S., Medeiros, T. P. V., Ardisson, J. D. & Lago, R. M. Role of $[FeO_x(OH)_y]$ surface sites on the adsorption of β-lactamic antibiotics on Al_2O_3 supported Fe oxide. *J. Hazard. Mater.* **317,** 327–334 (2016).

247. Shepherd, G., Klein-Schwartz, W. & Burstein, A. H. Efficacy of the Cation Exchange Resin, Sodium Polystyrene Sulfonate, to Decrease Iron Absorption. *J. Toxicol. Clin. Toxicol.* **38,** 389–394 (2000).

248. Bakshi, M. S., Kaur, G., Possmayer, F. & Petersen, N. O. Shape-Controlled Synthesis of Poly(styrene sulfonate) and Poly(vinyl pyrolidone) Capped Lead Sulfide Nanocubes, Bars, and Threads. *J. Phys. Chem. C* **112,** 4948–4953 (2008).

249. Si, G., Shi, W., Li, K. & Ma, Z. Synthesis of PSS-capped triangular silver nanoplates with tunable SPR. *Colloids Surfaces A Physicochem. Eng. Asp.* **380,** 257–260 (2011).

250. Leonov, A. P. *et al.* Detoxification of Gold Nanorods by Treatment with Polystyrenesulfonate. *ACS Nano* **2,** 2481–2488 (2008).

251. Krass, H., Papastavrou, G. & Kurth, D. G. Layer-by-Layer Self-assembly of a Polyelectrolyte Bearing Metal Ion Coordination and Electrostatic Functionality. *Chem. Mater.* **15,** 196–203 (2003).

252. Rodríguez-Fernández, J., Pérez-Juste, J., García de Abajo, F. J. & Liz-Marzán, L. M. Seeded Growth of Submicron Au Colloids with Quadrupole Plasmon Resonance Modes. *Langmuir* **22,** 7007–7010 (2006).

253. Raashid, S. Coordination inspired redox behaviour of Fe(II) and Co(II) explored for simultaneous Iron oxidation state analysis . **5,** 2715–2720 (2012).

254. Rizvi, M. A. Complexation modulated redox behavior of transition metal systems

(review). *Russ. J. Gen. Chem.* **85,** 959–973 (2015).

255. Rizvi, M. A., Teshima, N., Maqsood, S. R., Akhoon, S. A. & Peerzada, G. M. Thermo-Kinetic Investigation of Comparative Ligand Effect on Cysteine Iron Redox Reaction. *Croat. Chem. Acta* **88,** 67–72 (2015).

256. Jones, A. M., Griffin, P. J. & Waite, T. D. Ferrous iron oxidation by molecular oxygen under acidic conditions: The effect of citrate, EDTA and fulvic acid. *Geochim. Cosmochim. Acta* **160,** 117–131 (2015).

257. Ilbert, M. & Bonnefoy, V. Insight into the evolution of the iron oxidation pathways. *Biochim. Biophys. Acta - Bioenerg.* **1827,** 161–175 (2013).

258. Scialdone, O., Guarisco, C., Grispo, S., Angelo, A. D. & Galia, A. Investigation of electrode material – Redox couple systems for reverse electrodialysis processes. Part I: Iron redox couples. *J. Electroanal. Chem.* **681,** 66–75 (2012).

259. Rivas, B. L. & Moreno-Villoslada, I. Poly(sodium 4-styrenesulfonate)-metal ion interactions. *J. Appl. Polym. Sci.* **70,** 219–225 (1998).

260. You, H. & Fang, J. Particle-mediated nucleation and growth of solution-synthesized metal nanocrystals: A new story beyond the LaMer curve. *Nano Today* **11,** 145–167 (2016).

261. Wen, Y. H. *et al.* Studies on Iron (Fe^{3+}/Fe^{2+})-Complex/Bromine (Br[sub 2]/Br[sup −]) Redox Flow Cell in Sodium Acetate Solution. *J. Electrochem. Soc.* **153,** A929 (2006).

262. You, H. *et al.* Interface synthesis of gold mesocrystals with highly roughened surfaces for surface-enhanced Raman spectroscopy. *J. Mater. Chem.* **22,** 1998–2006 (2012).

263. Teguh, J. S., Liu, F., Xing, B. & Yeow, E. K. L. Surface-Enhanced Raman Scattering (SERS) of Nitrothiophenol Isomers Chemisorbed on TiO_2. *Chem. - An Asian J.* **7,** 975–981 (2012).

264. Lin, K.-Q. *et al.* Size Effect on SERS of Gold Nanorods Demonstrated via Single Nanoparticle Spectroscopy. *J. Phys. Chem. C* **120,** 20806–20813 (2016).

265. Edwards, H. G. M., Brown, D. R., Dale, J. A. & Plant, S. Raman spectroscopy of sulfonated polystyrene resins. *Vib. Spectrosc.* **24,** 213–224 (2000).

266. Morla-Folch, J., Guerrini, L., Pazos-Perez, N., Arenal, R. & Alvarez-Puebla, R. A. Synthesis and Optical Properties of Homogeneous Nanoshurikens. *ACS Photonics* **1,** 1237–1244 (2014).

267. Le Ru, E. C., Blackie, E., Meyer, M. & Etchegoin, P. G. Surface Enhanced Raman Scattering Enhancement Factors: A Comprehensive Study. *J. Phys. Chem. C* **111,** 13794–13803 (2007).

268. Sivapalan, S. T. *et al.* Off-Resonance Surface-Enhanced Raman Spectroscopy from Gold Nanorod Suspensions as a Function of Aspect Ratio: Not What We Thought. *ACS Nano* **7,** 2099–2105 (2013).

269. Kuttner, C. *et al.* Seeded Growth Synthesis of Gold Nanotriangles: Size Control, SAXS Analysis, and SERS Performance. *ACS Appl. Mater. Interfaces* **10,** 11152–11163 (2018).